3D LASER HOLOGRAPHIC INTERFEROMETRY MEASUREMENTS

by

Zhenhua Huang

A dissertation submitted in partial fulfillment
of the requirements for the degree of
Doctor of Philosophy
(Mechanical Engineering)
in The University of Michigan
2006

Doctoral Committee:

Associate Professor Albert J. Shih, Co-Chair
Professor Jun Ni, Co-Chair
Professor Elijah Kannatey-Asibu Jr
Professor Jianjun Shi
Adjunct Assistant Professor John Patrick Spicer

To my beloved family, especially my wife Mingmin Zhu and my daughter Cindy Huang.

Acknowledgements

I would like to express my sincere gratitude to my advisors Dr. Albert Shih and Dr. Jun Ni for their continuous guidance and education not only on my research but also on my moral maturity. Dr. Shih and Dr. Ni spent tremendous time from their busy schedules teaching me word by word how to write good papers and how to give good presentations. They also coached me through many trivial details how to treat other people well and how to be a good man. The significant efforts from Dr. Shih and Dr. Ni to secure my financial support are highly recognized.

The kind helps from all the other committee members, Dr. Jianjun Shi, Dr. Elijah Kannatey-Asibu Jr, and Dr. Pat Spicer, are greatly appreciated.

I am grateful to Mr. Dwight Carlson, Mr. Ron Swonger, and many other gentlemen from Coherix Inc. for their generous and unreserved technical supports. They not only provided me the opportunity to use their advanced equipment but also created the environment for me to learn the in-depth knowledge about this exciting technology.

The Engineering Research Center for Reconfigurable Manufacturing Systems directed by Professor Yoram Koren generously sponsored this research. And through the active involvement of many activities in ERC, my academic and social skills have been improved significantly. This precious experience in ERC will be treasured through the rest of my life.

The advanced measurement group directed by Robert Waite in DaimlerChrysler helped me initiate this exciting research area and provided me the access to their state-of-the-art instruments. The CogniTens Ltd. under Eyal Mizrahi also offered a lot of measurement help. Professor Jack Hu generously offered me the opportunities to use his devices for my research experiments. I thank them all.

My family, especially my wife Mingmin, always stood behind me throughout the four year PhD study, no matter up or down. Without their supports, I could not make this dissertation happen.

Contents

List of Figures

List of Tables

List of Appendices

Chapter 1

Introduction

1.1. Research motivations and goals

Automotive manufacturers are continually challenged by the needs to improve product quality and reduce warranty cost. Effective measurement methods are required to assure the precision and accuracy of component manufacturing, assembly, and testing. For automobile bodies and sub-assemblies, the optical measurement technologies have revolutionized the dimensional quality monitoring and control in the past two decades. The optical measurement systems enable the in-line, 100% inspection and use of advanced statistical analysis methods for root cause diagnostics. Such success has not yet been realized in the automotive powertrain and wheel assembly.

The automotive powertrain, which includes the engine, engine accessories, transmissions, differentials, and axles, generates and transmits powers to the wheel assembly. Powertrain and wheel assembly components have more stringent dimensional and geometrical form tolerances compared with body parts to meet the performance requirements. Five examples are presented in Fig. 1.1 to illustrate the powertrain and wheel assembly components. Typical tolerance specifications are discussed as following.

A typical V6 internal combustion engine head is shown in Fig. 1.1(a). The combustion deck surface on the engine head is a representative feature for precision powertrain components. The flatness specifications of this combustion deck surface are 150 μm along the 400 mm length, 100 μm across the 250 mm width, and 25 μm over any 25 mm x 25 mm surface area. Fig. 1.1(b) shows a hydraulic valve body for the automatic transmission. The part has the flatness specifications of 50 μm over the 200 mm x 100

mm surface and 25 μm across any 80 mm line. The wheel hub, as shown in Fig. 1.1(c), transmits power from the axle to wheel and supports the vehicle. The flatness specification of the hub surface, as marked by A, is from 30 to 50 μm. Figure 1.1(d) shows a rotor for disk brake. The surface, as marked by B on the rotor in Fig. 1.1(d), contacts the surface A on the hub in the wheel assembly. The brake pads contact the surface, marked by C on the rotor in Fig. 1.1(d). The runout specifications of surface C relative to the datum surface A of the rotor is usually 50 μm or less. This specification is critical to reduce the vehicle noise, vibration, and harshness (NVH) and improve drivability.

A Coordinate Measurement Machine (CMM) is a flexible and accurate contact-based measurement system which has been extensively used for the inspection of automotive powertrain components. However, CMMs are not feasible for the in-line inspection desired by transfer line production applications due to the extended measurement cycle time and lack of the full surface measurement capability. Some critical regions may be neglected. This can introduce the leakage problem when the engine head is assembled to the engine block. Further quality control and root cause diagnostics is also difficult from the incomplete data measured by CMMs.

The 3D non-contact optical measurement technologies have been widely utilized in quality inspection [1], reverse engineering [2], remote sensing [3], and robot guidance [4]. In recent years, new optical hardware and software developments have further advanced the accuracy and reduced the cost of 3D optical measurement systems. Optical measurement systems have been successfully applied in the automotive quality control and process diagnosis of body manufacturing and assembly.

Figure 1.2 shows the measurement size and form tolerance requirements for different automotive components [1]. The powertrain and wheel assembly components, marked in boxes, have the form tolerances from 10 to 100 μm in the measurement volume less than 0.1 m^3. Extensive research efforts [5-8] have been dedicated to the applications of non-contact optical measurements for powertrain components. There is still a gap before widespread and practical in-line utilization by industry due to the following three reasons. First, a wide variety of surface features, surface textures and

finish, and surface reflectance exist for the powertrain components. This imposes a great challenge on precision optical measurement systems. Second, the performance of optical measurements usually depends on the environment conditions. An optical system with good performance in laboratory may not function well due to the vibration, thermal deviation, and environment illumination disturbance in the production line. Third, the measurement speed needs further improvement to satisfy the in-line measurement requirements.

This research is motivated by the lack of effective and efficient 3D non-contact optical measurement methods for precision automotive components. The 3D μm-level accurate optical systems, which will be capable of the in-line, full surface precision measurement, are targeted in this research.

1.2. Laser holographic interferometry for powertrain components measurement

A wide variety of 3D optical measurement methods are available. Based on the principles of the data extraction for 3D dimensional and geometrical form measurement, the 3D optical measurement methods can be categorized as: stereovision [9], interferometry [10,11], structured lighting [12,13], laser triangulation [14], Moiré fringe [15-17], focus detection [18,19], time-of-flight [20], and laser speckle pattern sectioning [21]. A comparison matrix of six 3D measurement systems is illustrated in Appendix A.

The laser holographic interferometry method is demonstrated to have the potential capabilities for in-line, full surface precision measurement of powertrain and wheel assembly components. The basic principles and characteristics of the laser holographic interferometry methods are described as following. The system principle, configurations, and the performance evaluation are discussed in detail in Appendix B.

Laser holographic interferometry extracts the 3D profile of an object by identifying the phase of the light wave which is reflected from the object surface and carries the height information of the object. The laser holographic interferometer usually uses a beam splitter to separate the laser into two separate beams, the reference and the carrier beams of the same wavelength. The carrier beam is directed onto the object

surface and the phase is modulated by the 3D object profile. The modulated carrier beam interferes with the reference beam and generates the hologram containing the 3D profile information of the object surface. By identifying the phase difference at each pixel in the hologram, the 3D profile of the object can be extracted.

The laser holographic interferometry for 3D surface profile measurement has three advantages. (1) High accuracy. Combined with phase shifting analysis, interferometric methods can have the accuracy of 1/100 of a fringe [22]. For a typical system, the accuracy of the height measurement can reach 0.50 μm for a 300 mm x 300 mm field of view (FOV) with the height measurement range up to 17 mm [3]. The lateral resolution and range of phase shifting interferometric instruments depend on the CCD pixel spacing and the magnification of the objective. (2) No shadowing or occlusion. Shadowing occurs when the object cannot be illuminated but is visible to the sensor. Occlusion occurs when the object is illuminated but invisible to the sensor. Either shadowing or occlusion does not exist in the laser holographic interferometry because the object is illuminated and viewed from the same direction. (3) No moving parts. The 3D image of the entire field of view is generated without scanning. With all parts fixed, the system has high reliability and repeatability.

There are three limitations for the current laser holographic interferometry method. First, the measurement area is limited by the system FOV and no hologram registration method is available for the measurement of part larger than the system FOV. Second, the height measurement range is limited by the optical configurations. And the height measurement accuracy and resolution will decrease if the height measurement range increases using the wavelength-tuning technology. Third, difficulties are usually expected for the precision measurement of round and more generally free-form specular surfaces due to the large surface curvature which makes insufficient modulated light reflected back to generate the hologram.

1.3. Feasibility study of 3D optical systems for engine head measurement

The CMM, laser holographic interferometry, and stereovision methods are compared to identify the feasibility for powertrain component measurement. The

combustion deck surface of a V6 engine head, as shown in Fig. 1.1(a), is applied as an example. Figure 1.3 shows the top view of the combustion deck surface.

The flatness measurement results using the CMM, laser holographic interferometry and stereovision methods are shown in Fig. 1.4. Figure 1.4(a) shows the measurement results using a Zeiss CMM, model UPMC CARAT 850/1200 with a scanning probe. The length (size) measurement accuracy of this CMM is 0.7 + L/600 μm within the 1 m^3 measurement volume, where L is the length or size of the part in mm. And the scanning probing error is 1.8 μm for 88 sec. Therefore the measurement result of this CMM can be used as the target value. Figure 1.4(b) shows the measurement result of the laser holographic interferometer. The FOV of this system is 300 mm x 300 mm and only a portion of the entire combustion deck surface is measured, as shown in Fig. 1.4(b). The stereovision measurement is shown in Fig. 1.4(c). A total of 21 3D images are combined to represent the whole surface. Instead of the line data in CMM, the full surface area data is obtained for flatness characterization using the stereovision system.

A line is marked at corresponding locations of the combustion deck surface in Figs. 1.4(a), 1.4(b), and 1.4(c). The surface height deviations across the line for the CMM, laser holographic interferometry, and stereovision are all around 15 μm. This indicates that similar trends are obtained by the laser holographic interferometry and stereovision compared to the CMM measurement result. The standard deviations of the data points measured using CMM, laser holographic interferometry, and stereovision are 24.5, 24.8, and 17.4 μm, respectively. This shows the potential of the laser holographic interferometry for precision powertrain measurements. This is a preliminary result and further detailed investigation is necessary.

1.4. Overview of research

The objective of this dissertation is to develop a 3D non-contact optical system based on laser holographic interferometry with enhanced performance for the in-line, full surface, and μm-level precision measurement of automotive components, such as engine

heads and blocks, automatic transmission valve bodies, wheel hubs and rotors, and precision journals. Following research issues are studied in this dissertation.

In Chapter 2, a hologram registration method is developed to enable the laser holographic interferometry for the precision measurement of objects larger than the FOV. The performance of the developed method is evaluated by comparing the registered and standard measurements of the same hub surface. The combustion engine head deck surface is measured by CMM and the laser holographic interferometry with the hologram registration method to verify the developed method.

In Chapter 3, a phase unwrapping method is developed to mathematically increase the height measurement range of the laser holographic interferometry while maintaining the same level of accuracy and resolution. Three approaches, including the masking and recovery, dynamic segmentation, and phase adjustment for pixels in thin boundary regions, are developed to effectively avoid the divergence problem of boundary pixels. An automatic transmission valve body is applied as an example of laterally discontinuous surfaces to verify this method.

In Chapter 4, a mathematical method is developed to utilize the laser holographic interferometry with customized optical and mechanical configurations for flexible and full surface measurement of cylinders with variable diameters. Simulations are conducted to verify the capability of the developed method. The experiment is performed to measure the master cylinder with negligible cylindricity errors and the practical feasibility of the method is demonstrated.

In Chapter 5, the contributions of this research are specified in the conclusions and the future work is identified in two areas. First is to further improve the performance of the cylindricity measurement with the laser holographic interferometry system. An effective calibration method of the aspherical cylindrical lens with minimum aberrations should be developed. More robust and efficient optimization methods shall be explored to reach a more reliable estimation of the system configuration parameters. Second is to develop a more comprehensive method to quantitatively analyze the error flows starting from each measured points to the final evaluated flatness result for the high definition

measurement system. This method will be extended to other complicated geometrical forms such as cylinder and sphere.

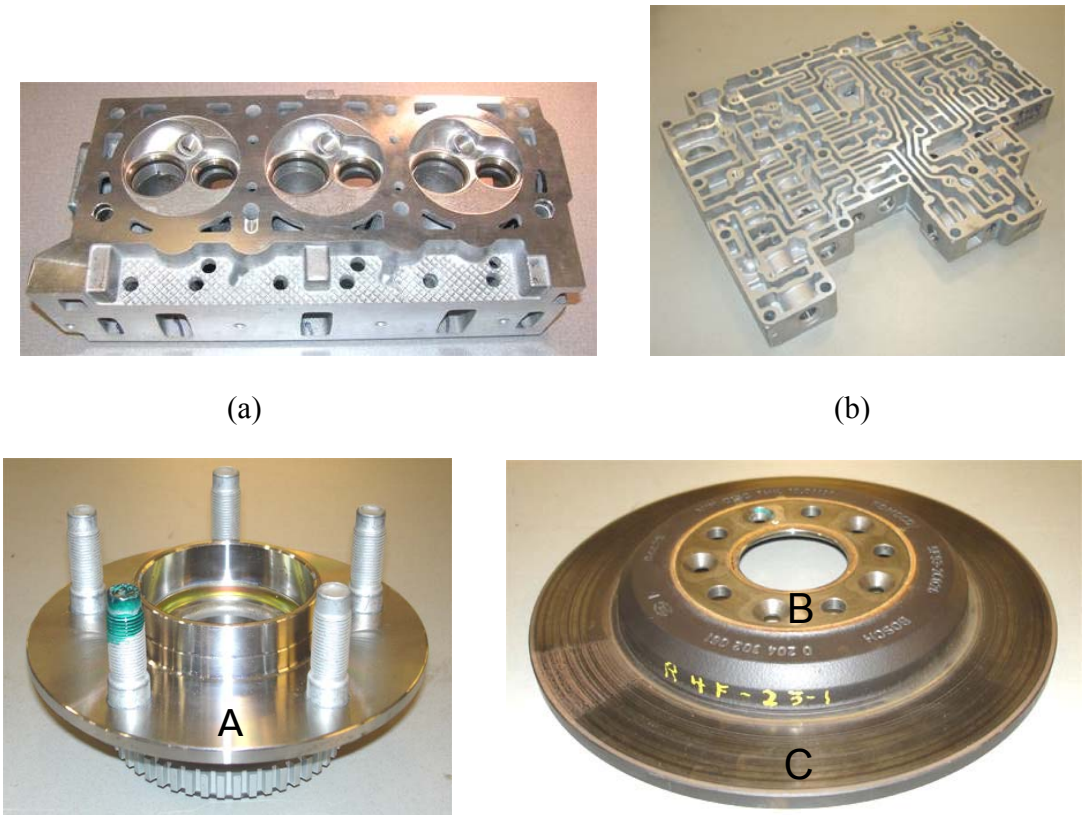

(a) (b)

(c) (d)

Fig. 1.1. Examples of automotive powertrain and wheel assembly components: (a) engine head, (b) automatic transmission valve body, (c) wheel hub, and (d) wheel rotor.

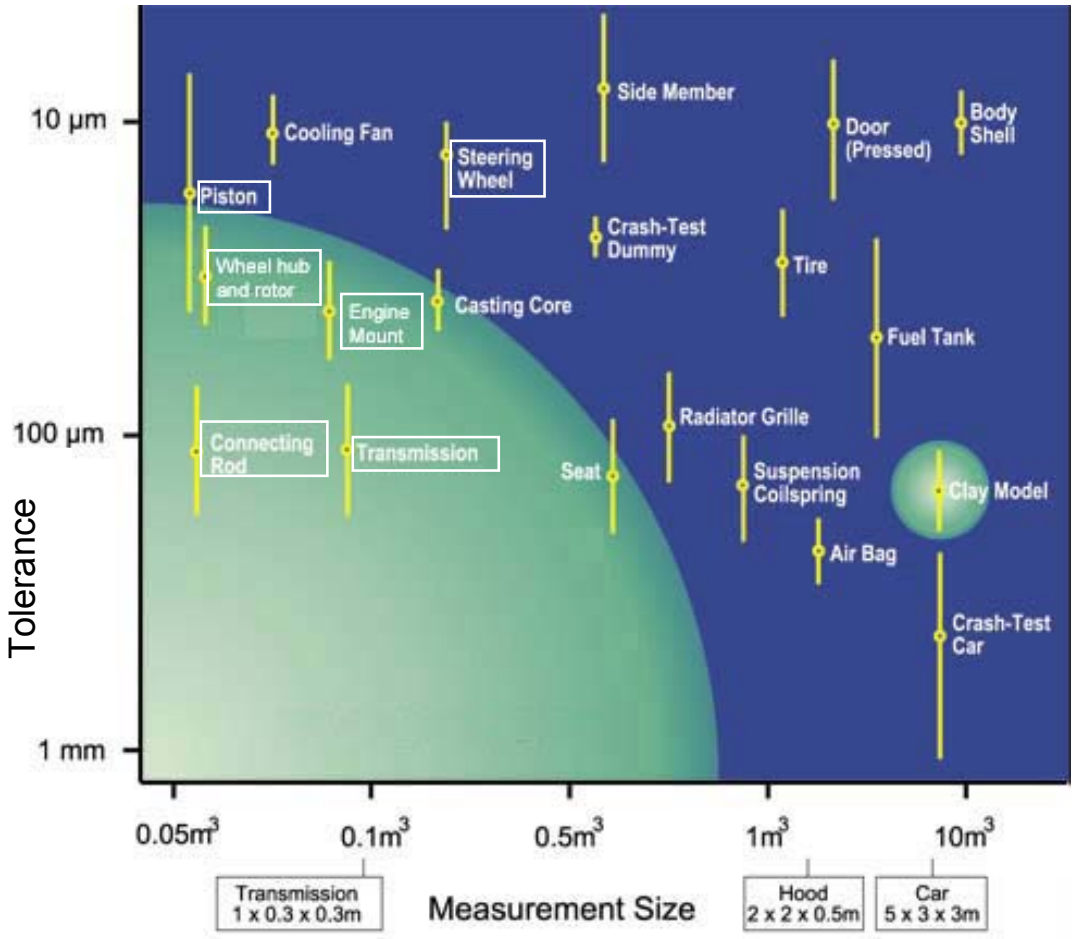

Fig. 1.2. Measurement size and tolerance requirement for automotive components. [1]

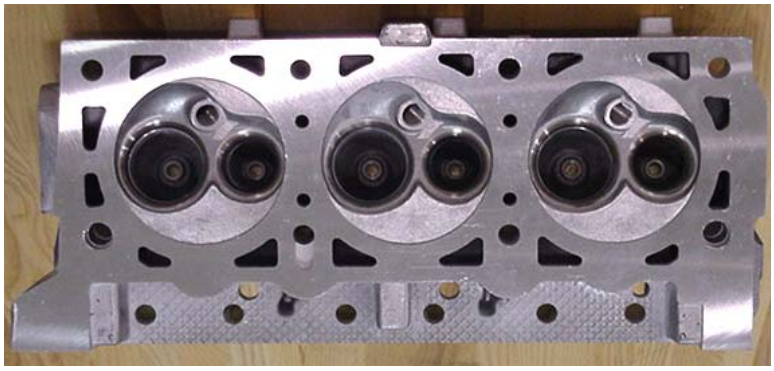

Fig. 1.3. Top view of a V6 engine head combustion deck surface.

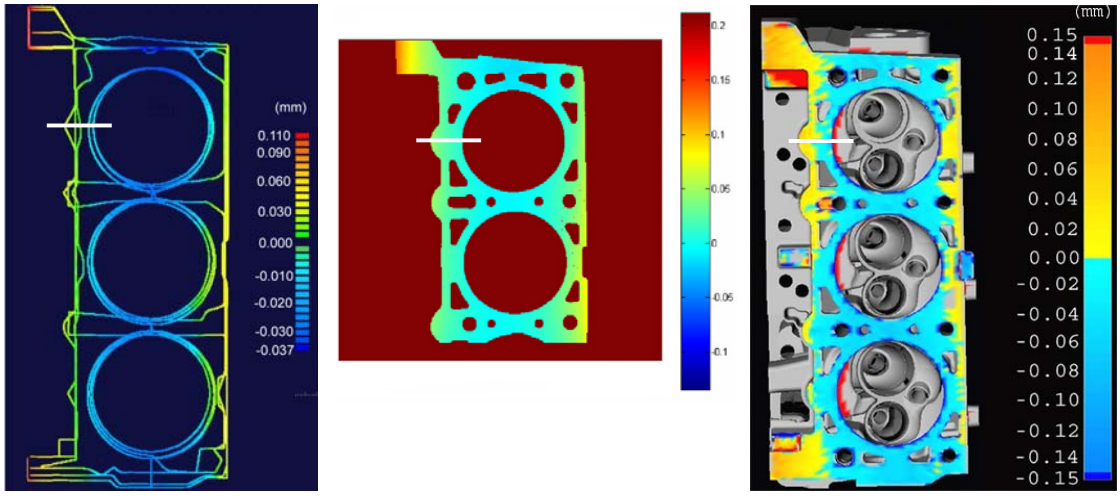

(a) (b) (c)

Fig. 1.4. Flatness measurement results by: (a) Zeiss CMM, model UPMC CARAT 850/1200 with a scanning probe, (b) laser holographic interferometer Coherix Shapix 1000, and (c) stereovision system CogniTens Optigo 200.

Chapter 2

Hologram Registration for 3D Precision Holographic Interferometry Measurement

2.1. Introduction

The limited size of FOV is a constraint in the current laser holographic interferometer for precision measurement of large objects, such as the internal combustion engine head combustion deck surfaces and the automatic transmission valve bodies. Increasing the dimensions of optical mirrors in the interferometer to enlarge the measurement FOV is possible but cost prohibited. The goal of this research is to develop a hologram registration method as a more practical alternative to enable the laser holographic interferometry measurement of objects larger than the FOV.

Several 3D image registration methods have been developed. VanderLugt [23] and Kim et al. [24,25] applied the 3D pattern recognition, Dias et al. [26] fused the range and intensity data of the image, and Hsu et al. [27,28] extracted and matched the edge and surface features for hologram registration. However, the hologram registration method is still lacking.

This study develops a hologram registration method to enable laser holographic interferometry for the precision measurement of large objects. The mathematical procedures for hologram registration are discussed in Sec. 2.2. In Sec. 2.3, the accuracy of hologram registration is evaluated using two examples and this method is validated.

2.2. Hologram registration

The hologram registration method is developed to enable the laser holographic interferometry for measuring objects larger than the FOV. Traditionally, targets have been used for image registration in 3D optical measurement [29,30]. The approach proposed in this study eliminates the use of targets and simplifies the measurement procedure for image registration.

The procedures to register two holographic measurements are shown in Fig. 2.1. The FOV contains W rows and W columns of measurement points, which correspond to pixels in the CCD camera. The distance between adjacent rows or columns of points in FOV is p. The size of the FOV is pW x pW, as illustrated in Fig. 2.1(a). Mathematically, the measured data in FOV is represented by a W x W matrix. Each element in the matrix is a complex number. The magnitude and angle of the complex number represent the light intensity I and the phase difference $\Delta\varphi$, respectively, of a measurement point in the FOV.

The length of the measurement object is larger than the width pW of the FOV, as shown in Fig. 2.1. Two measurements, marked as Measurement A in Fig. 2.1(a) and Measurement B in Fig. 2.1(b), are conducted. An overlapped region exists between the Measurements A and B.

A procedure called masking is applied to extract the region of the measurement object in FOV for data analysis. The measurement object in Fig. 2.1 is a rectangle with three holes. The masking procedure eliminates the data points outside the measurement object area. The region after masking, called the Unmasked Region, is marked by hatched lines in Fig. 2.1. The Unmasked Region can have an arbitrary shape. A rectangle shape to enclose the whole Unmasked Region, called the Rectangle Unmasked Region, is selected for mathematical representation and processing of the region by matrices. For example, as shown in Fig. 2.1(a) for Measurement A, the dimension of the Rectangle Unmasked Region is pN_A x pM_A. Two matrices associated with the Rectangle Unmasked Region are the intensity matrix $\mathbf{I}_A$ and phase matrix $\mathbf{\Delta\varphi}_A$, which represent the array of measured intensities and calculated phase differences, respectively. Both matrices have the dimension N_A x M_A. These two matrices are extracted from the

measurement data in the FOV. Similarly, the Measurement B after masking has the Rectangle Unmasked Region, as illustrated by the hatched region as shown in Fig. 2.1(b), with physical dimension of pN_B x pM_B. The intensity matrix $\mathbf{I}_B$ and phase matrix $\mathbf{\Delta\varphi}_B$, both with the dimension of N_B x M_B, are extracted to represent the measurement.

The correlation analysis, to be discussed in Sec. 2.2.1, is used to calculate the translation to match the two measurements and find the Overlapped Region.

2.2.1. Translation

Translation is the lateral movement in the x and y directions between the two measurements of the same measurement object. The lateral translation is determined by the location of the correlation peak in the cross-correlation matrix $\mathbf{C}$ of two intensity matrices $\mathbf{I}_A$ and $\mathbf{I}_B$.

The direct normalized method [31] is utilized to calculate the cross-correlation matrix $\mathbf{C}$, which has the dimension of $(N_A + N_B - 1)$ x $(M_A + M_B - 1)$.

$$\mathbf{C} = \mathbf{I}_A \otimes \mathbf{I}_B \tag{2.1}$$

where $\otimes$ is the cross-correlation operator.

Each element of the matrix $\mathbf{C}$ is expressed by

$$C(u,v) = \frac{\sum_{x,y}\left[I_A\left(x-\left(u-N_A\right),y-\left(v-M_A\right)\right)-\bar{I}_A\right]\left[I_B(x,y)-\bar{I}_B\right]}{\sqrt{\sum_{x,y}\left[I_A\left(x-\left(u-N_A\right),y-\left(v-M_A\right)\right)-\bar{I}_A\right]^2\cdot\sum_{x,y}\left[I_B(x,y)-\bar{I}_B\right]^2}} \tag{2.2}$$

where

u and v are the lateral shift coordinates, ranging from 1 to $N_A + N_B - 1$ and from 1 to $M_A + M_B - 1$, respectively,

x and y are the integers indicating location (x, y) of each element in the matrix, and

$\bar{I}_A$ and $\bar{I}_B$ are the means of $\mathbf{I}_A$ and $\mathbf{I}_B$, respectively.

The correlation peak is the maximum value in the cross-correlation matrix **C**. If the correlation peak is located at (N_p, M_p), the lateral translation in pixels of Measurement A relative to Measurement B is $(N_p - N_A, M_p - M_A)$.

The lateral translation identified from the procedures described above has the resolution of pixel spacing. Sub-pixel spacing resolution is possible by using interpolated pixel data. The interpolation does enlarge the dimensions of the cross-correlation matrix and increase the computation time.

A rectangular Overlapped Region exists between Measurements A and B. This is illustrated by the Overlapped Regions A′ and B′ in Measurements A and B, as shown by the bold dashed line in Figs. 2.1(a) and 2.1(b), respectively. Overlapped Regions A′ and B′ have identical shape and size. The location and size of the Overlapped Regions can be calculated from the translation between Measurements A and B. The phase matrices of Overlapped Regions A′ and B′ are denoted as $\mathbf{\Delta\varphi}_{A'}$ and $\mathbf{\Delta\varphi}_{B'}$ and have the dimension of $N_{A'} \times M_{A'}$ and $N_{B'} \times M_{B'}$, respectively, where $N_{A'} = N_{B'}$ and $M_{A'} = M_{B'}$. The relative tilt and phase shift between Measurements A and B are calculated by processing $\mathbf{\Delta\varphi}_{A'}$ and $\mathbf{\Delta\varphi}_{B'}$. This is elaborated in Sec. 2.2.2.

2.2.2. Tilt and shift correction

Tilting and shifting are adjustments used to make two planes match in the 3D space. Tilt are represented by two angles, relative to the x and y axes, of the difference between the normal vectors of the two planes. Tilt one plane relative to the other and the two planes can be made parallel. Shift is the translation along the z axis after the tilt

correction to make two parallel planes match in space. Because the phase is linearly proportional to the height of the object surface, as described in Sec. B.2.3.1, the tilt and shift are represented in the phase domain for the processing convenience.

The measured data points on the Overlapped Regions do not necessarily form a plane in practical applications. However, because the Overlapped Regions are the same portion of the object surface in two separate measurements, the difference between phases of measured data points on two Overlapped Regions should follow the trend of a plane. By least square fitting this plane, the tilt and shift corrections can be calculated.

The $\Delta\varphi_A(x, y)$ and $\Delta\varphi_B(x, y)$ are the phases of the pixel in $\mathbf{\Delta\varphi}_{A'}$ and $\mathbf{\Delta\varphi}_{B'}$ with the lateral location (x, y) in the Overlapped Regions A′ and B′, respectively. Define $\Delta\varphi_D(x, y)$ as the unmasked overlapped phase difference which equals $\Delta\varphi_B(x, y) - \Delta\varphi_A(x, y)$, where $(x, y) = (x_1, y_1), (x_2, y_2), \ldots, (x_n, y_n)$, and n is the total number of unmasked pixels in the Overlapped Region.

Collect all the unmasked pixels in $\Delta\varphi_D(x, y)$ and construct a matrix **L**:

$$\mathbf{L} = \begin{bmatrix} x_1 & y_1 & 1 \\ x_2 & y_2 & 1 \\ & \cdots & \\ x_n & y_n & 1 \end{bmatrix} \tag{2.3}$$

Record all the phases of the corresponding unmasked pixels and construct a vector **P**:

$$\mathbf{P} = \begin{Bmatrix} \Delta\varphi_D(x_1, y_1) \\ \Delta\varphi_D(x_2, y_2) \\ \vdots \\ \Delta\varphi_D(x_n, y_n) \end{Bmatrix} \tag{2.4}$$

Fit a least square plane to $\Delta\varphi_D$, defined by $\Delta\varphi_D(x,y) = ax + by + c$. The coefficients *a*, *b*, and *c* are determined by:

$$\begin{Bmatrix} a \\ b \\ c \end{Bmatrix} = \left(\mathbf{L}^T\mathbf{L}\right)^{-1}\left(\mathbf{L}^T\mathbf{P}\right) \tag{2.5}$$

The coefficients *a* and *b* relate to the tilt about *y* and *x* axes, respectively, of Measurement B relative to Measurement A. The coefficient *c* determines the relative shift of Measurement B relative to Measurement A in *z* axis.

Once the coefficients, *a*, *b*, and *c* are obtained, the phase $\Delta\varphi_B(x,y)$ of the whole measurement region in Measurement B is corrected by:

$$\Delta\varphi_B^c(x,y) = \Delta\varphi_B(x,y) - \left[ax + by + c\right] \tag{2.6}$$

where $\Delta\varphi_B^c(x,y)$ is the tilt-corrected phase of $\Delta\varphi_B(x,y)$.

In summary, to register two holograms shown in Fig. 2.1, the unmasked Measurements A and B are first identified. Using the cross-correlation analysis, the translational shift is calculated and the rectangular Overlapped Regions A′ and B′ are marked. The phase matrices of two Overlapped Regions are used to find the tilt and shift between Measurements A and B and complete the data registration.

2.2.3. Rotation

Rotation is the angular movement of the measurement object in the *xy* plane between the two measurements. If the rotation occurs with the lateral translation, the identification and correction of the rotation will be conducted before the lateral translation which is described in Sec. 2.2.1.

2.2.3.1. Rotation identification

The identification of the rotation is implemented using the Fourier transform [32] of the intensity matrices. Assume the object in the Measurement B is rotated by θ_0 and translated by (x_s, y_s) relative to the Measurement A, the intensity matrix $\mathbf{I}_B$ can be expressed by

$$I_B(x,y) = I_A(x\cos\theta_0 + y\sin\theta_0 - x_s, -x\sin\theta_0 + y\cos\theta_0 - y_s) \tag{2.7}$$

The Fourier transform **F** of the intensity matrix **I** is determined by [33]

$$F_k(\xi,\eta) = \frac{1}{N}\sum_{x,y} I_k(x,y) e^{-2\pi j(x\xi + y\eta)/N} \tag{2.8}$$

where $k = A$ or B, and N is the total number of data points.

The relation between $\mathbf{F}_A$ and $\mathbf{F}_B$ is determined by

$$F_B(\xi,\eta) = e^{-j2\pi(\xi x_s + \eta y_s)} F_A(\xi\cos\theta_0 + \eta\sin\theta_0, -\xi\sin\theta_0 + \eta\cos\theta_0) \tag{2.9}$$

From Eq. (2.9), we have

$$M_B(\xi,\eta) = M_A(\xi\cos\theta_0 + \eta\sin\theta_0, -\xi\sin\theta_0 + \eta\cos\theta_0) \tag{2.10}$$

where $\mathbf{M}_A = |\mathbf{F}_A|$ and $\mathbf{M}_B = |\mathbf{F}_B|$ are the magnitudes of $\mathbf{F}_A$ and $\mathbf{F}_B$, respectively.

Eq. (2.10) indicates that the matrix $\mathbf{M}_B$ is rotated by the angle θ_0 relative to the matrix $\mathbf{M}_A$ in the $\zeta\eta$ plane. Convert the Cartesian coordinate (ζ, η) of the matrices $\mathbf{M}_A$

and $\mathbf{M}_B$ into the polar coordinate (ρ, θ), where ρ and θ are the magnitude and angle of the coordinate (ζ, η), respectively. Then the relation between the matrices $\mathbf{M}_A$ and $\mathbf{M}_B$ in Eq. (2.10) is expressed by

$$M_B(\rho,\theta) = M_A(\rho,\theta+\theta_0) \tag{2.11}$$

The rotation θ_0 between the two matrices $\mathbf{M}_A$ and $\mathbf{M}_B$ is separated from the lateral translation (x_s, y_s) using the Eq. (2.11). This rotation can be identified using the cross-correlation, defined by Eqs. (2.1) and (2.2), of the matrices $\mathbf{M}_A$ and $\mathbf{M}_B$ in the $\rho\theta$ plane.

2.2.3.2. Rotation correction

Once the rotation θ_0 of the object between the two measurements is identified using the method described in Sec. 2.2.3.1, the rotation will be corrected before the identification of the lateral translation by [33]

$$\begin{bmatrix} x^r \\ y^r \end{bmatrix} = \begin{bmatrix} \cos\theta_0 & \sin\theta_0 \\ -\sin\theta_0 & \cos\theta_0 \end{bmatrix} \begin{bmatrix} x \\ y \end{bmatrix} \tag{2.12}$$

where x^r and y^r are the lateral coordinates after rotation.

Interpolation is required in general after the rotation because the lateral coordinates (x, y), which are integers in the matrix before the rotation, will not necessarily be integers after the rotation.

The bilinear interpolation [33] is applied due to the easy implementation and less computational cost. Assume that the intensity values I_{11}, I_{12}, I_{21}, and I_{22} at the four positions (x_1, y_1), (x_1, y_2), (x_2, y_1), and (x_2, y_2), respectively, are known and the intensity at the position (x, y) can be estimated by Eq. (2.13), where $x_1 < x < x_2$ and $y_1 < y < y_2$.

$$I(x,y)=\frac{I_{11}}{(x_2-x_1)(y_2-y_1)}(x_2-x)(y_2-y)+\frac{I_{21}}{(x_2-x_1)(y_2-y_1)}(x-x_1)(y_2-y)+$$
$$\frac{I_{12}}{(x_2-x_1)(y_2-y_1)}(x_2-x)(y-y_1)+\frac{I_{22}}{(x_2-x_1)(y_2-y_1)}(x-x_1)(y-y_1)$$

(2.13)

2.3. Accuracy evaluation of hologram registration

Two examples using different approaches are applied to evaluate the accuracy of the proposed hologram registration method. The first approach uses a measurement object which is small and fits in the FOV. The object can be accurately measured to create a standard height measurement $h_s(x, y)$. The same object is then measured twice on two sides with an overlapped region in between. The proposed method is applied to calculate the registered height measurement $h_m(x, y)$. The accuracy of the registration method is quantified by comparing $h_s(x, y)$ to $h_m(x, y)$. A wheel hub is used as the Example I.

The other approach uses a measurement object larger than the FOV. The CMM measurement of the whole measurement object is used as the standard measurement $h_s(x, y)$. It is compared to the registered measurement $h_m(x, y)$. An engine combustion deck surface is used as the Example II.

2.3.1. Accuracy evaluation procedures

Two parameters, the root mean squared (RMS) error e_{rms} of the difference between the $h_s(x, y)$ and $h_m(x, y)$ and the surface flatness, are used to evaluate the accuracy of the hologram registration method.

To compare $h_s(x, y)$ and $h_m(x, y)$, a linear transformation is required to tilt and shift the $h_m(x, y)$ relative to $h_s(x, y)$ before calculating e_{rms}. Since the measurement system in this study only delivers the relative height measurement, this linear transformation is required. Let $F_s(x, y) = a_s x + b_s y + c_s$ and $F_m(x, j) = a_m x + b_m y + c_m$ be

the least square fitted planes of $h_s(x, y)$ and $h_m(x, y)$, respectively. The linear transformation of $h_m(x, y)$ can be expressed as:

$$h_m^T(x,y) = h_m(x,y) - \left[(a_m - a_s)x + (b_m - b_s)y + (c_m - c_s)\right]. \tag{2.13}$$

The RMS error e_{rms} is:

$$e_{rms} = \sqrt{\frac{\sum_{(x,y)=(x_1,y_1)}^{(x_d,y_d)} \left(h_s(x,y) - h_m^T(x,y)\right)^2}{d}} \tag{2.14}$$

where d is the total number of all unmasked pixels.

The surface flatness is also used as an index to evaluate the accuracy. Two flatness definitions are used in this study. One is 6σ flatness, which is equal to six times the standard deviation of measured points from the least square fitted plane [34]. This definition suppresses the spike noise contribution to the flatness. The other is the maximum peak to valley from the least square fitted plane. This is called the peak-to-valley flatness.

2.3.2. Example I -- wheel hub

As shown in Fig. 2.2, a wheel hub, which is small to fit the FOV, is used as a measurement object to evaluate the accuracy of the hologram registration method. Five bolts were assembled to the wheel hub to transmit power to the wheel. These bolts after being assembled may alter the original hub surface flatness and need to be inspected. The laser holographic interferometry is a unique method to measure the surface flatness of the hub with the assembled bolts. The diameter of the hub, as shown in Fig. 2.2(b), is about 150 mm.

The intensities and phases for each measurement are shown in Fig. 2.3. The solid black regions in Figs. 2.3(a) and 2.3(b) are masked and excluded for height measurement. The intensity matrices $\mathbf{I}_A$ and $\mathbf{I}_B$ have the dimension of 649 x 964 and 615 x 964 pixels, respectively.

The cross-correlation matrix **C** of $\mathbf{I}_A$ and $\mathbf{I}_B$ is represented in Fig. 2.4. The dimension of **C** is 1297 x 1927 pixels. The location of the correlation peak is identified at (301, 964). This indicates that the measurement matrix A should translate 301 − 649 = −348 pixels in $+x$ direction and 964 − 964 = 0 pixels in the $+y$ direction to make the strongest match with the measurement matrix B. With this translational movement, the Overlapped Regions A′ and B′ can be chosen from the measurements A and B, respectively.

The hologram phase $\Delta\varphi_{A'}$ and $\Delta\varphi_{B'}$ of the Overlapped Regions A′ and B′, respectively, are shown in Fig. 2.3(b) in dashed rectangles. The reference point is marked with a plus sign. The dimension $N_{A'}$ x $M_{A'}$ of the Overlapped Regions is 300 x 964 pixels. The relative tilt and shift parameters [a, b, c], defined in Eq. (2.5), are [-1.0×10^{-4} rad/pixel, 1.2×10^{-5} rad/pixel, 1.23×10^{-2} rad]. Correct the relative tilt using Eq. (2.6) and register two holograms. The phase and intensity of the registered hologram are shown in Fig. 2.5. A clear separation line between two measurements can be observed in the registered intensity, as shown in Fig. 2.5(b). This is because the intensity of the Measurements A and B are connected without any correction. This does not affect the height measurement, which is calculated from the registered phase, as shown in Fig. 2.5(a).

There is a dent on the hub surface, which is marked in Fig. 2.2(b) and shown in close-up view in Fig. 2.2(c). Because this dent is more than 9 pixels in the image, this cannot be eliminated by 9 point median filtering. The 6σ surface flatness definition is applied to suppress the effect of this dent on the surface flatness measurement results.

Interpolation is applied to achieve sub-pixel resolution for the hologram registration. First, the lateral cross-correlation process, defined in Eq. (2.2), is interpolated. For example, one point linear interpolation is utilized in the 300 x 964

pixels overlapped region. The lateral translation is the same after processing. For higher sub-pixel resolution, two or more points can be linear interpolated.

The registered height measurement $h_m(x, y)$ is shown in Fig. 2.6(a). The standard measurement $h_s(x, y)$, as shown in Fig. 2.6(b), is obtained in a single holographic interferometry measurement of the wheel hub, which is small to fit in the FOV. The 6σ flatness of $h_s(x, y)$ and $h_m(x, y)$ are 25.3 and 25.2 μm, respectively. The gage repeatability (1σ) of the system is evaluated as 0.3 μm. Compared to this value, the 0.1 μm or 0.4% flatness difference is not significant. It indicates that the hologram registration does not significantly contribute to the measurement error.

The difference between $h_s(x, y)$ and $h_m(x, y)$ is presented in Fig. 2.7. The RMS value e_{rms} is 0.4 μm. This further proves the accuracy of the proposed hologram registration method.

The effect of the area of the overlapped region was also evaluated. As shown in Fig. 2.8, hologram registration with 10, 25, and 40% of the overlapped vs. total measurement area were conducted with the corresponding e_{rms} of 0.9, 0.5 and 0.4 μm, respectively. As the area of the overlapped region increases, the error introduced by the registration method decreases. The increase of overlapped region from 10 to 25% reduces the e_{rms} by 0.4 μm. The same 15% increase of overlapped region from 25 to 40% only reduces the e_{rms} by 0.1 μm. Also, when the area of the overlapped region is larger than 40%, the error e_{rms} is approaching the 0.3 μm system error. It is expected that increasing the overlapped region beyond 40% will not reduce e_{rms} significantly.

2.3.3. Example II -- engine head combustion deck surface

As shown in Fig. 2.9, an engine head combustion deck surface has a large, 420 x 180 mm, measurement area. Two measurements, marked as Measurements A and B in Fig. 2.9, were conducted. The translation of the measurement object was achieved by moving it with the side datum surface of the measurement object in contact with a straight reference bar in the machine. The intensity matrices $\mathbf{I}_A$ and $\mathbf{I}_B$ have dimensions of 948 x 584 and 889 x 599 pixels, respectively. Following the cross-correlation

procedure, the overlapped region with the size of 598 x 458 pixels is identified. The relative tilt and phase shift parameters [a, b, c], defined in Eq. (2.5), are [4.5×10^{-4} rad/pixel, 3.1×10^{-3} rad/pixel, −0.5 rad]. The tilt and phase shift are corrected using Eq. (2.6) and the two measurements are registered as a 1378 x 599 matrix.

The 3D profile of the registered surface is shown in Fig. 2.10(a). In comparison, the same surface was measured by a Zeiss Model UPMC 850 CMM with a scanning probe. The CMM measurement, which covers only a small portion of the surface, is shown in Fig. 2.10(b).

The peak-to-valley flatness definition is applied for evaluation because the surface area measured by CMM and laser holographic interferometry is significantly different. Under such condition, the standard deviation does not provide a comparable representation of measurement results. The peak-to-valley flatness of the CMM and the registered laser holographic measurement are 149.7 and 153.5 μm, respectively. This close comparison, 2.5% discrepancy, further verifies that the developed hologram registration method is feasible for the precision measurement of large components.

2.4. Concluding remarks

This research developed a hologram registration method for the laser holographic interferometry to measure the 3D profile of objects larger than the FOV. Two examples were used to validate the registration method using two different approaches. The first example, a wheel hub, was smaller than the FOV and enabled the use of holographic interferometry to create the standard measurement for the accuracy evaluation of hologram registration. The second example, an engine head combustion deck surface, was larger than the FOV and a CMM was used to create the standard measurement. The e_{rms} was 0.4 μm for the wheel hub (Example I) and peak-to-valley flatness difference was about 4 μm for the engine head combustion deck surface (Example II). The feasibility of the proposed hologram registration method was demonstrated.

The unique feature of the proposed registration method is the elimination of using target for data registration. This could simplify the measurement procedure and reduce

the time. Several research investigations can follow this study. The robustness of the proposed registration method with more complex surface geometric shapes than examples of the wheel hub and engine combustion deck surfaces is a good future research topic. The limit of the tilt and shift and optimal percentage of the area of the overlapped region can also be investigated as a series of follow-up research for practical application of the proposed hologram registration method. Only two measurements are used for the hologram registration examples in this study. A more comprehensive program to register multiple holograms can be developed and the error propagation analysis can be conducted to further advance the capability of hologram registration for precision measurements.

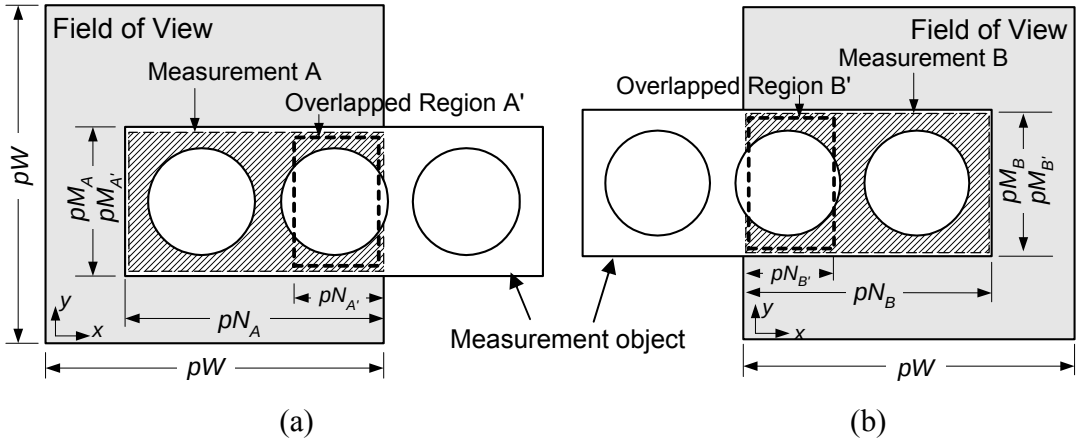

(a) (b)

Fig. 2.1. Measurement regions and variables used for hologram registration: (a) Measurement A and (b) Measurement B. In this research, $W = 1024$, $p = 0.293$ mm, and $pW = 300$ mm.

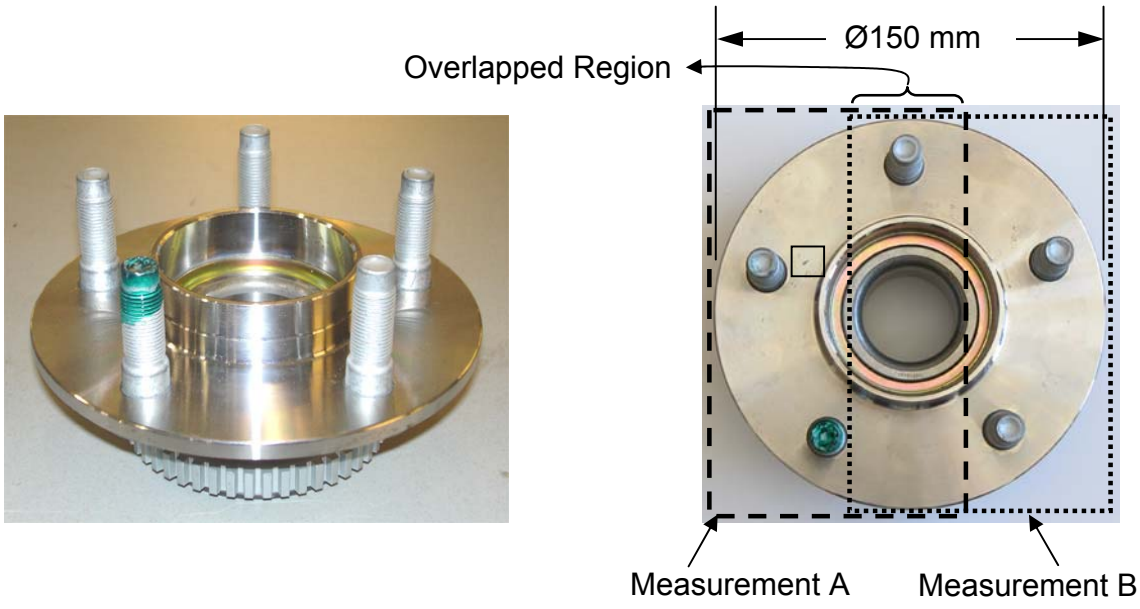

(a) (b)

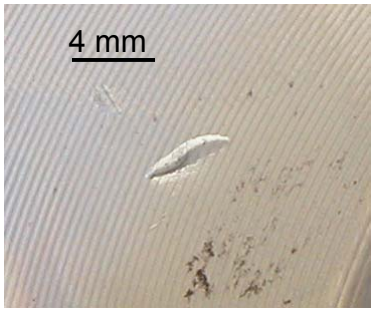

(c)

Fig. 2.2. Wheel hub: (a) isometric view, (b) top view, and (c) close-up view of the dent marked in solid rectangle in (b).

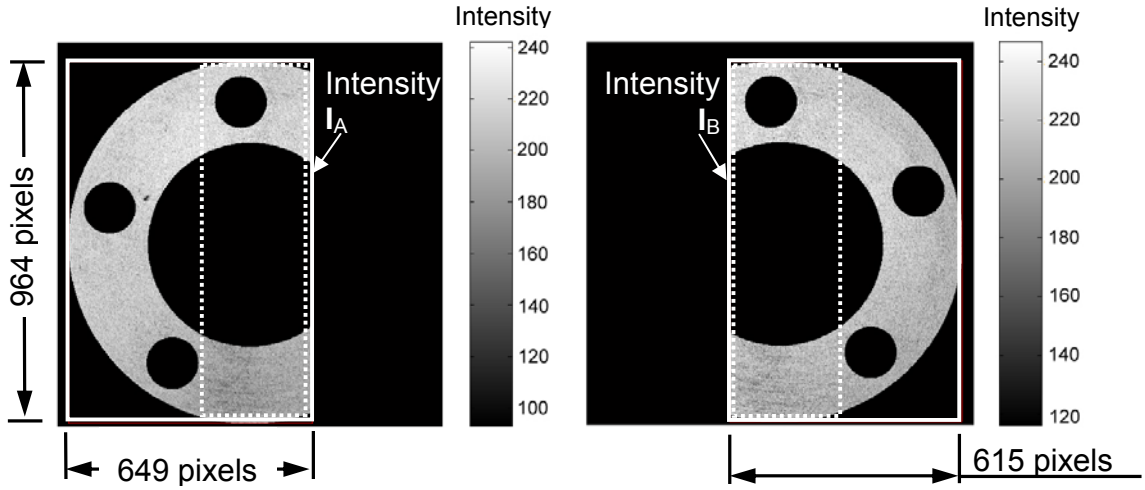

(a)

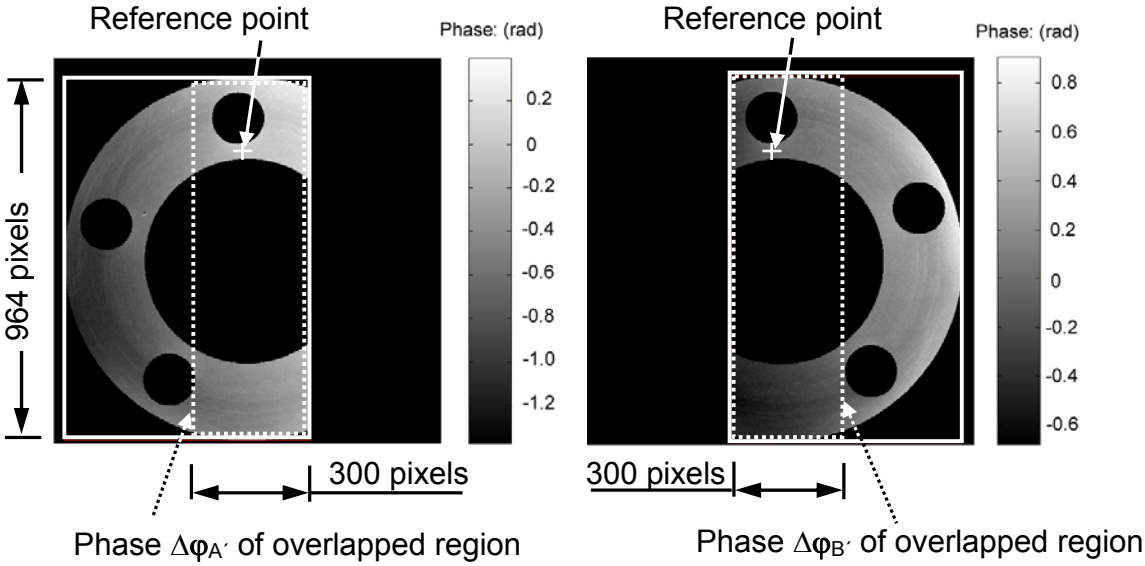

(b)

Fig. 2.3. Measured holograms of the wheel hub: (a) intensity and (b) phase of Measurements A and B.

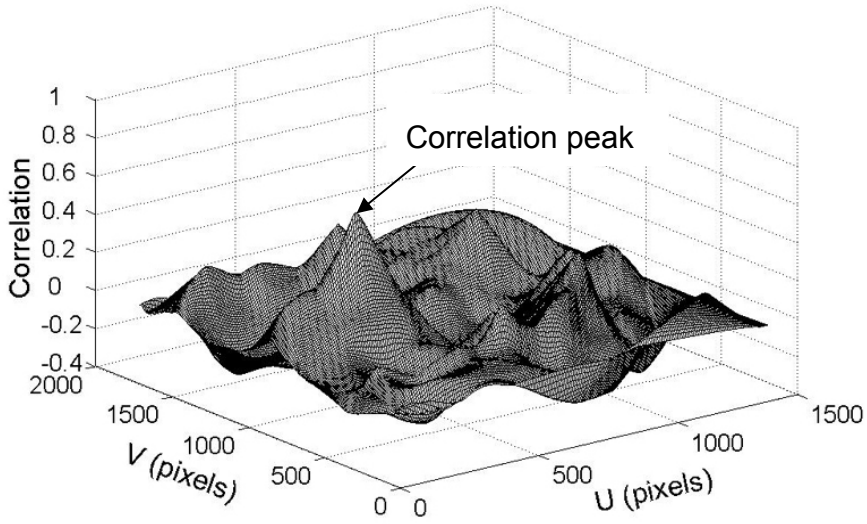

Fig. 2.4. Correlation matrix C of Measurements A and B of the wheel hub.

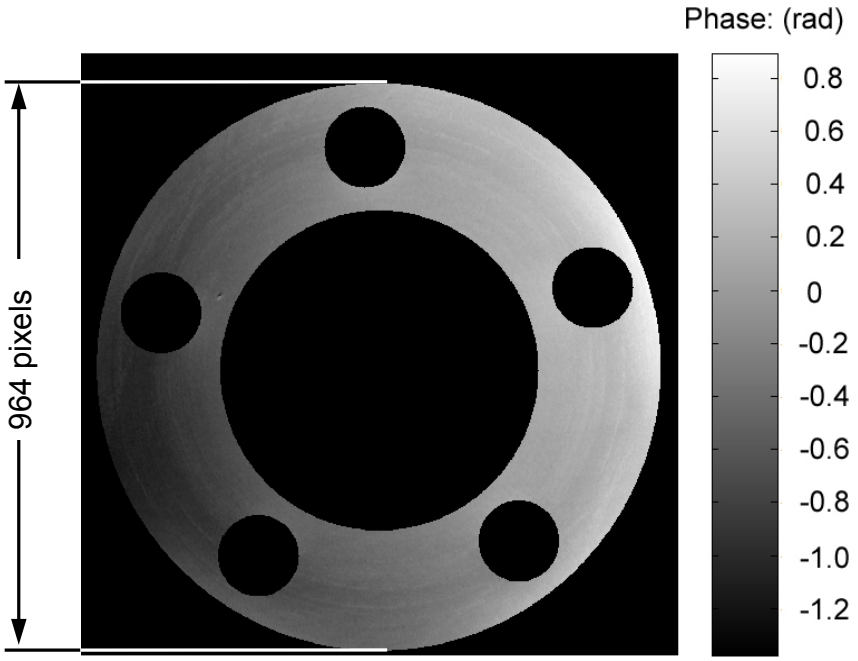

(a)

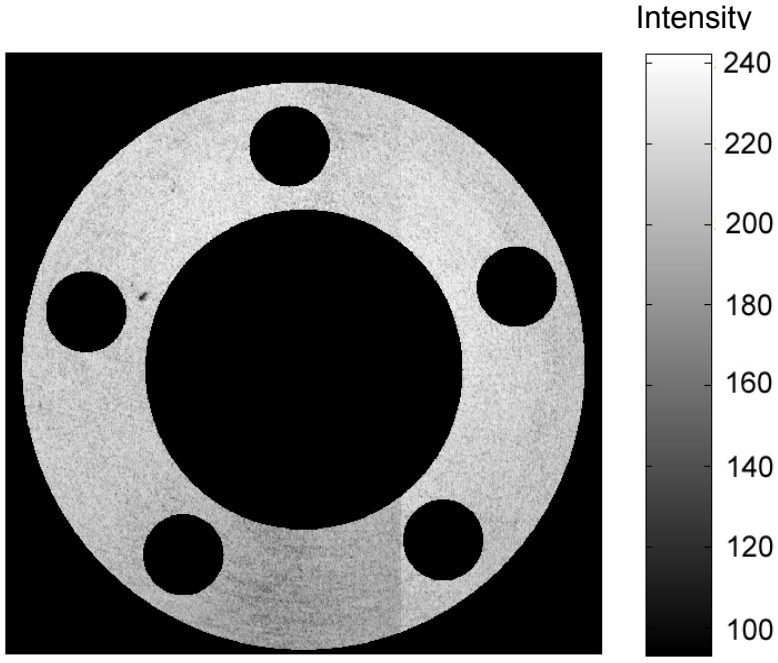

(b)

Fig. 2.5. Registered hologram of the wheel hub: (a) phase and (b) intensity.

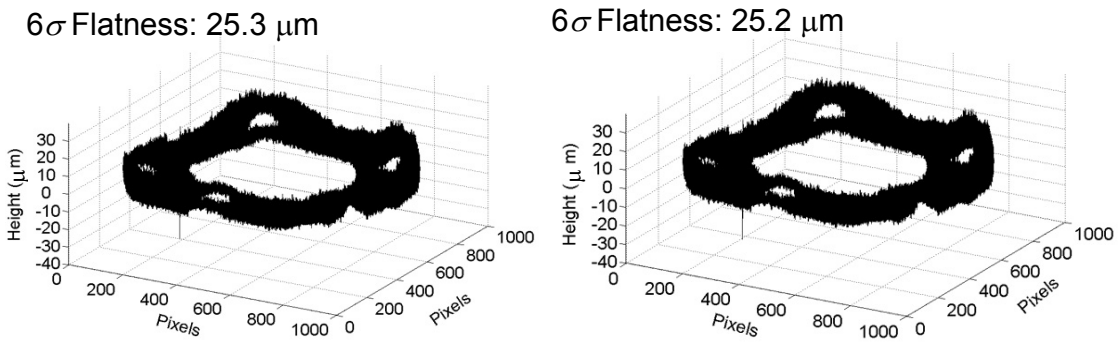

Fig. 2.6. 3D profile measurement of the wheel hub: (a) registered measurement $h_m(x, y)$ and (b) standard measurement $h_s(x, y)$.

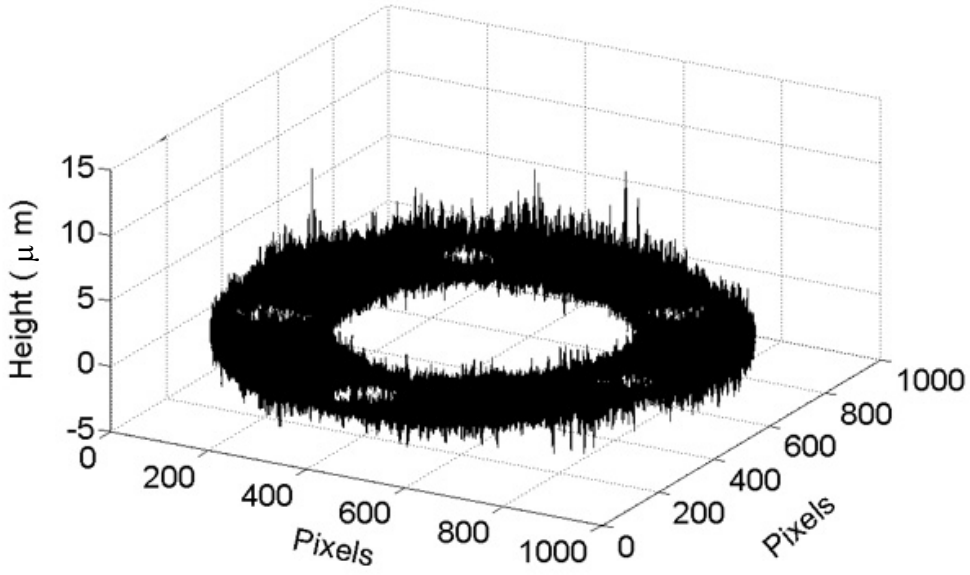

Fig. 2.7. Difference between $h_s(x, y)$ and $h_m(x, y)$ of the wheel hub.

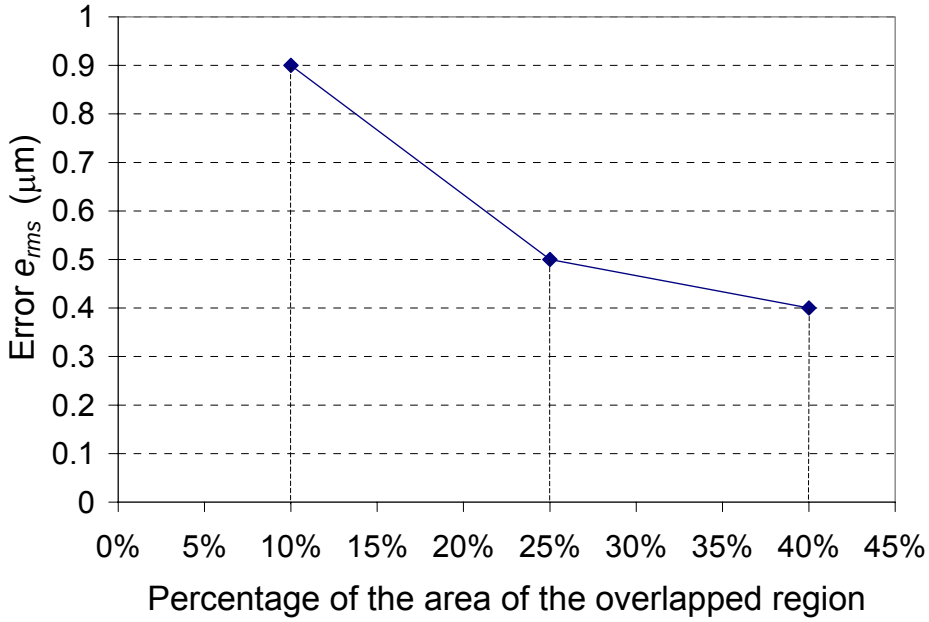

Fig. 2.8. Effect of the area of the overlapped region on the error e_{rms}.

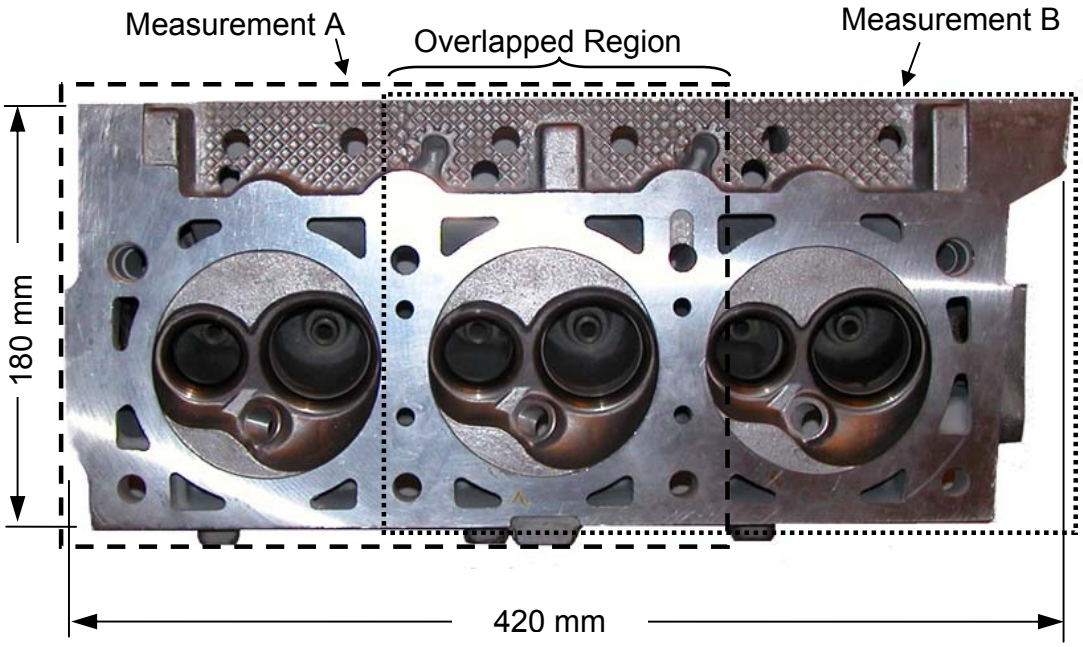

Fig. 2.9. Overview of a V6 engine head combustion deck surface.

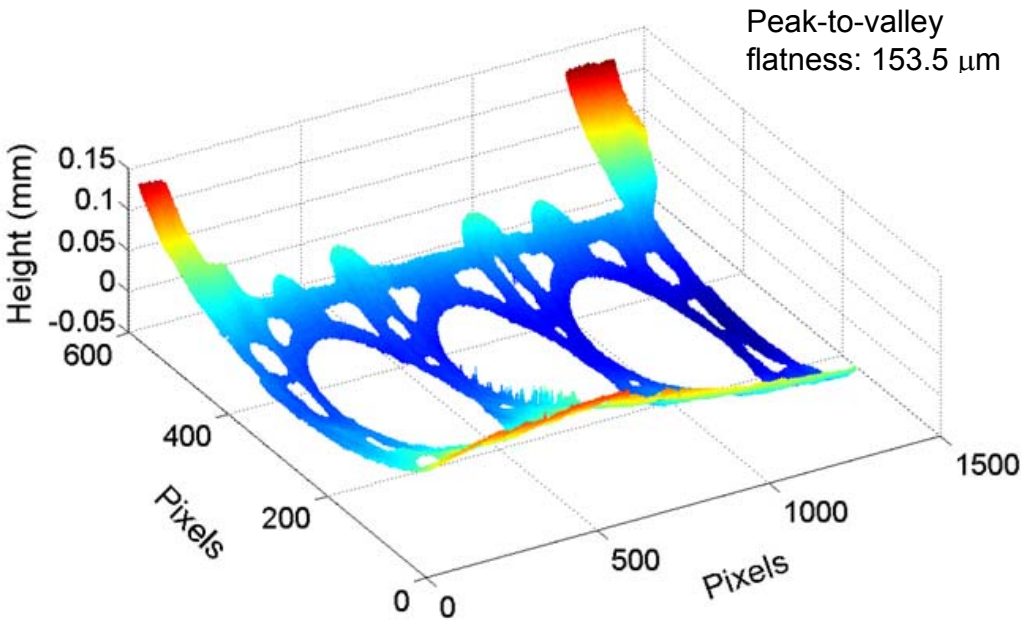

(a)

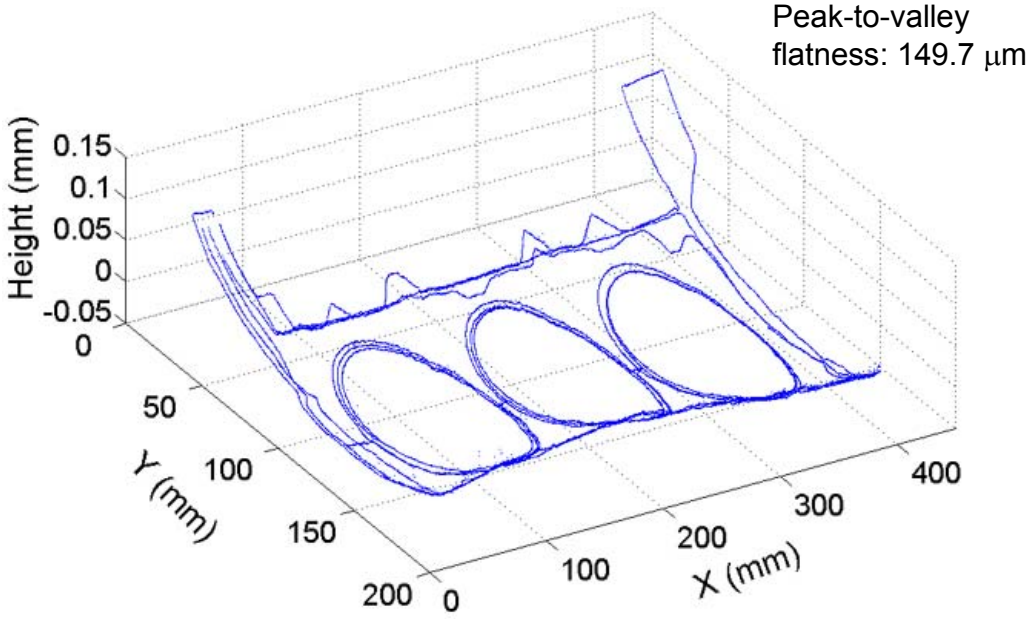

(b)

Fig. 2.10. 3D profile of the engine head combustion deck surface: (a) registered measurement and (b) CMM measurement.

Chapter 3

Phase Unwrapping for Large Depth-of-Field 3D Laser Holographic Interferometry Measurement of Laterally Discontinuous Surfaces

3.1. Introduction

Phase unwrapping is a mathematical procedure to eliminate the ambiguity in the phase map for imaging applications, including the synthetic aperture radar interferometry, laser holographic interferometry, magnetic resonance imaging, and others [35]. In this research, phase unwrapping is studied to increase the depth-of-field for the 3D laser holographic interferometry measurement of laterally discontinuous surfaces. The phases calculated by the laser holographic interferometry range from $-\pi$ to π, the principal value range of reverse trigonometric functions. The limited range of phase creates ambiguity, called phase wrap. Fig. 3.1(a) shows an example of a parabolic-shaped surface with phases ranging from 0 to 18 radians. The measurement of this surface with phase wraps is shown in Fig. 3.1(b). Sudden changes of phase are observed at pixels with the phase value near $-\pi$ or π. Phase unwrapping restores the true phase map (Fig. 3.1(a)) from the measured phase map (Fig. 3.1(b)). If the spatial sampling rate in the phase map is at least twice of the highest frequency of the change of phase, so called Shannon sampling theorem [36], a phase wrap is assumed when the phase difference between two adjacent pixels exceeds the threshold π. The wrapped phase is compensated by the integral multiples of 2π to be unwrapped.

The technical advancements in phase unwrapping have been aimed to achieve the high noise robustness and low computational cost. Both temporal- and spatial-based approaches for phase unwrapping have been developed. Temporal-based phase unwrapping, developed by Huntley and Saldner [36,37], unwraps the change of phase over time for each pixel independently. The error is restricted to individual pixels and

does not propagate between pixels. Special optical configurations [38] are required to relate the unwrapped phase to the height of surface and it makes the temporal-based approach not suitable for the laser holographic interferometry measurement, the targeted application in this research.

Spatial-based phase unwrapping processes the phase in the 2D spatial domain using either path-dependent or path-independent methods. The path dependent method unwraps the phase along a specially designed path by converting the 2D array into a folded 1D data set. This method needs complex path design strategy in the presence of noise [39] and is not feasible for the measurement of the laterally discontinuous surface, which contains regions disconnected with each other. Information between disconnected regions is unavailable along the designed path. The automatic transmission valve body, as shown in Fig. 3.2(a), has the laterally discontinuous surface. Figure 3.2(b) shows the top view of the measurement surface of a valve body. It contains grooves which carry pressurized fluid to control the position of valves for gear shifting. The surface with high aspect ratio regions disconnected with each other makes the phase unwrapping difficult.

The spatial-based path-independent methods, including model- [40,41], Bayesian- [42], least-squares- [43], and integration-based [44-52], do not require a specially designed path for the phase unwrapping. However, none of these spatial-based path-independent methods can be directly applied to unwrap the phase of laterally discontinuous surfaces because of narrow, curved regions and the discontinuity among regions. The region-referenced method [52], which is an integration-based and path-independent method, uses the phase data in regions surrounding a pixel to detect the phase wrap. This method has good noise robustness, can automatically adjust the direction to adapt for narrow and curved regions, and is selected to be further developed in this study.

The region-referenced phase unwrapping, segmentation and patching, and its problems for narrow segmented regions and boundary pixels are explained in Sec. 3.2. In Sec. 3.3, the solutions of phase wrap identification on boundary pixels, masking and recovery, dynamic segmentation, and phase adjustment are developed. An example is

presented in Sec. 3.4 to validate the proposed method and study the computational efficiency and convergence.

3.2. Region-referenced phase unwrapping

The region-referenced method is applied as the base for the developed phase unwrapping method. The region-referenced method uses an iterative algorithm to unwrap the phase. This method searches the pixels with phase wraps and compensates the phase by adding or subtracting 2π depending on the sign of phase wrap. The surface is assumed continuous in the height direction with no phase jump over π between two adjacent pixels. The searching and compensation processes are repeated until no phase wrap is detected.

3.2.1. Principle

A simple method to determine the phase wrap is to use the four adjacent pixels of a pixel, marked as (i, j) in Fig. 3.3(a), to determine the phase wrap [39,54]. If at least one of the four adjacent pixels has the phase difference larger than π, this pixel is recognized to have phase wrap and needs to be compensated by adding or subtracting 2π for phase unwrapping. The problem of this phase unwrapping method is the sensitivity to noise, which can cause the divergence of the iteration. A more complicated region-referenced criterion is developed by Huang and He [52] to overcome this problem. Each adjacent pixel in Fig. 3.3(a) is replaced by a region to determine the phase wrap. For example, the adjacent pixel $(i-1, j)$ in Fig. 3.3(a) is replaced by 15 pixels, as shown by the shaded area in Fig. 3.3(b), to determine the phase wrap. If over half of the pixels in the shaded region have the phase difference larger than π with the pixel (i, j), a phase wrap is identified at pixel (i, j). The criterion of over half of pixels, which is 8 in the case in Fig. 3.3(b), is empirically optimal [52]. Rotating the shaded region around the pixel (i, j) by 90, 180, and 270º, the other three reference regions corresponding to the other three adjacent pixels in Fig. 3.3(a) can be obtained. The phase wrap at pixel (i, j) is identified if any of the four reference regions have the phase wrap. Other reference regions of different

shapes are also developed [52]. This method can significantly improve the noise robustness. However, pixels on the boundary, so called boundary pixels, have limited number of pixels in the reference region to detect the phase wrap. This makes boundary pixels more sensitive to noise. The laterally discontinuous surface, like the automatic transmission valve body in Fig. 3.2, has many boundary pixels due to the discontinuity between regions, and may introduce the divergence problem in phase unwrapping.

Figure 3.4 shows the measured phase map of the automatic transmission valve body. The solid black background is the region not for measurement. All the phase values are within the range from $-\pi$ to π, the principal value range of reverse trigonometric functions. Phase wraps are observed in the phase map. The close-up view of the region S_1 is shown in Fig. 3.5(a). The boundary pixels, marked by arrows, are a source of instability and make the region-referenced phase unwrapping easy to diverge. The idea proposed in this research is to first conduct the phase unwrapping without considering these boundary pixels, i.e., boundary pixels with phase wrap are masked. After phase unwrapping, these masked pixels are recovered by median filtering. This concept will be elaborated in Sec. 3.3.1.

3.2.2. Segmentation and patching

Segmentation, which divides the phase map into many small overlapped segments, has been developed to improve the computational efficiency for phase unwrapping [50,52]. Each segment is first unwrapped independently. Then, the data of two adjacent segments is connected using the overlapped region between these two segments. The static segmentation is defined as the segmentation method with fixed size of segments and overlapped regions during unwrapping.

Patching is the process to combine the data of individual segments after phase unwrapping into an integral phase map. Two adjacent segments with an overlapped region are compared with each other and the phases of one segment are shifted by the multiple of 2π to make the overlapped regions of the two segments match. After shifting, these two adjacent segments are concatenated. This procedure is applied to all the adjacent segments until an integral phase map including all the individual segments is

reached. The path which the patching process follows is determined iteratively by systematically selecting one of the four adjacent segments as the next segment to be patched.

An example of static segmentation with patching is shown in Fig. 3.6(a), which illustrates the close-up view of region S_2 of the valve body in Fig. 3.4. The size of each segment is $(W + W_o)$ x $(W + W_o)$ with the width of the overlapped region equal to W_o. The unwrapped phase in segments $C_1D_1E_1F_1$ and $C_2D_2E_2F_2$ will be patched by shifting the phases of the segment $C_1D_1E_1F_1$ relative to the segment $C_2D_2E_2F_2$ to make the overlapped region $C_2D_1E_1F_2$ matches in both $C_1D_1E_1F_1$ and $C_2D_2E_2F_2$.

The problem of the static segmentation for laterally discontinuous surfaces is the thin boundary regions. An example of the boundary region is shown in Fig. 3.6(b), which is the close-up view of the region S_4 in Fig. 3.6(a). A boundary region with only 1 to 2 pixels in width after static segmentation and patching is observed on the top of the segment. The phase wrap which exists in this boundary region cannot be detected or removed using the phase unwrapping method. The dynamic segmentation and the phase adjustment, to be discussed in Secs. 3.3.3 and 3.3.4, respectively, are developed to overcome this problem.

3.3. Masking, dynamic segmentation and phase adjustment

The masking and recovery, dynamic segmentation, and phase adjustment are developed to improve the robustness and the computational efficiency for phase unwrapping of laterally discontinuous surfaces. To avoid the divergence problem, boundary pixels with phase wrap are masked during phase unwrapping. These pixels are recovered after phase unwrapping. Dynamic segmentation adaptively determines the size of segments to reduce the number of thin boundary regions in segmentation. The phase adjustment corrects the errors after dynamic segmentation to complete phase unwrapping.

3.3.1. Phase wrap identification on boundary pixels

To determine if a boundary pixel has phase wrap, a criterion is developed. Each boundary pixel has four reference regions. In each reference region, some pixels are not on the object surface, and do not have valid phase information. Those pixels with valid phase information are denoted as valid pixels. If more than half of the valid pixels in any of the four reference regions of a boundary pixel have the phase difference larger than π, this boundary pixel is designated to have the phase wrap and will be masked in the phase unwrapping.

3.3.2. Masking and recovery

Masking is applied on the boundary pixels with phase wrap to avoid the divergence. The masked boundary pixels with phase wrap are not processed for the phase unwrapping. However, the masked boundary pixel is still a valid pixel and its phase information is used in reference regions of other pixels for phase unwrapping analysis.

After phase unwrapping, to recover the value at a masked boundary pixel, the median filtering [55] is applied. Median filtering first sorts the phase values of pixels in a matrix (usually 3x3, 5x5, 7x7, or 9x9 in dimension) centered at the pixel and then chooses the median as the new phase value. If any of the pixels in the matrix have been masked, values of these pixels are not included in the sorting sequence. Median filtering has the advantage of suppressing the spike noise.

An example of the masking and recovery process is illustrated in Fig. 3.5. Figure 3.5(a) shows the close-up view of the region S_1 in Fig. 3.4. Boundary pixels with phase wrap are marked by arrows. These pixels are masked for the phase unwrapping. Fig. 3.5(b) shows the result after phase unwrapping and before the recovery. Seven masked boundary pixels still have the phase wrap before the recovery. The recovery process assigns the phase values to the masked pixels using a 7x7 median filter. The result after applying the median filtering is shown in Fig. 3.5(c). The phase unwrapping is completed without divergence problem and the phase values of the masked boundary pixels have been recovered.

3.3.3. Dynamic segmentation

The static segmentation, as discussed in Sec. 3.2.2, has fixed size of segments and fixed width of overlapped regions. Dynamic segmentation is developed in this study to overcome the problem of thin boundary regions of laterally discontinuous surfaces.

To identify the thin boundary region, the width of boundary regions needs to be quantified. A parameter, called the boundary width p_m, of each boundary region is defined as the maximum number of pixels inside the boundary region in the direction perpendicular to the side of the segment. An example is shown in Fig. 3.7(a). Two unmasked boundary regions, marked by the hatched lines, have p_m equal to p_{m1} and p_{m2}, respectively. The smaller of the two, p_{m1}, is denoted as the minimum side width p_{min}, which is defined as the minimum of the boundary widths of all the boundary regions on a side of the segment.

An exception in the determination of p_m occurs when a narrow region exists along the two adjacent sides. As shown in Fig. 3.7(b), the pixels, which are on the top side of the segment and are close (less than a predetermined threshold T) to the left side of the segment, are not considered in the calculation of the p_{m3}. In Fig. 3.7(b), the smaller of p_{m3} and p_{m4} is used to determine the p_{min} to represent the minimum boundary width of the top side of the rectangular segment.

Dynamic segmentation starts with the static segmentation. If one side of a segment has p_{min} smaller than T after the static segmentation, dynamic segmentation is triggered. The side of the segment after the static segmentation will be moved toward outside of the segment by $m_1 = (T - p_{min})$ pixels to increase the width of the thin boundary region. The counting of p_{min} is applied again to identify if any thin boundary region still exists on the new segment. If it does, the side of the segment is moved in the opposite direction by $m_2 = m_1 + T/2$ pixels. This dynamic segmentation is repeated to all four sides of the rectangular segment and has demonstrated the ability to eliminate most, but not all, of the thin boundary regions in practical applications.

Figure 3.8 shows an example of the dynamic segmentation of the region S_3 in Fig. 3.4. The size of segments and the width of overlapped regions are $W = 50$ and $W_o = 20$

pixels in the static segmentation. The original segment after the static segmentation is shown in Fig. 3.8(a). The segment including the overlapped region is 70 x 70 pixels. The top side of the segment has two regions. The p_m in the middle region is 70 and in the right region is 2, which is smaller than the predetermined threshold value T (= 6) and is identified as a thin boundary region. The p_{min} is equal to 2. Using the dynamic segmentation, the top side of the segment is then moved upward by m_1 = 4 (= 6 – 2) pixels. The newly obtained segment, as shown in Fig. 3.8(b), has a new thin boundary region with the boundary width p_m (= 4) in the upper left corner. The top side of the segment is then moved in the opposite direction by m_2 = 7 (= 4 + 6/2) pixels. The newly obtained segment with no thin boundary region on the top side is shown in Fig. 3.8(c). The same procedure is repeated on the other three sides. The final segment after the dynamic segmentation is 67 x 74 pixels, as shown in Fig. 3.8(d).

The phase unwrapping results with dynamic segmentation of the region S_2 in Fig. 3.4 are shown in Fig. 3.6(c). For the segment $C_1D_1E_1F_1$ with no thin boundary region, the segment after dynamic segmentation, $C'_1D'_1E'_1F'_1$, does not change. On the contrary, the segment $C_2D_2E_2F_2$ has thin boundary regions. The dynamic segmentation changes the segment to $C'_2D'_2E'_2F'_2$ to eliminate the thin boundary regions. The phase wrap in the region S_4 of Fig. 3.6(a) is eliminated after dynamic segmentation (Fig. 3.6(c)). The dynamic segmentation improves the noise robustness of the phase unwrapping method.

3.3.4. Phase adjustment for thin boundary regions with phase wrap

After dynamic segmentation, some thin boundary regions may still exist. The phase wrap in these thin boundary regions cannot be solved using the region-referenced method described in Sec. 3.2. The phase adjustment method is developed to identify the phase wrap in the integral phase map and adjust the phase values by the multiple of 2π in the thin boundary regions to complete the phase unwrapping process.

Figure 3.9(a) illustrates two examples of regions S_5 and S_6 in the integral phase map of the automatic transmission valve body (Fig. 3.2). The close-up view of the region S_5 is shown in Fig. 3.9(b). The thin boundary region in S_5 is located on the top side. During dynamic segmentation, the boundary line cannot extend beyond the integral phase

map and the thin boundary region exists. The close-up view of S_6 is shown in Fig. 3.9(c). The thin boundary region with phase wrap still exists after moving the boundary line twice in dynamic segmentation.

The phase values of pixels in thin boundary regions can be estimated or extrapolated using a polynomial function fitted by the data of the integral phase map. If the difference between the estimated phase values and the existing phases of pixels in thin boundary regions is larger than 2π, the multiple of 2π is subtracted to the existing phases to make the difference smaller than 2π. The polynomial function can be of the first, second, third, or higher order. The first order polynomial function representation of the integral phase map is:

$$\varphi_1(i,j) = a_{0,1} + a_{1,1}i + a_{2,1}j \tag{3.1}$$

where

$\varphi_1(i,j)$ is the estimated phase value of the pixel (i,j) in the integral phase map,

i and j are the row and column coordinates, respectively, of the integral phase map, and

$a_{0,1}$, $a_{1,1}$, and $a_{2,1}$ are the coefficients of the first order polynomial function, determined using the least square estimation [56]:

$$\begin{Bmatrix} a_{0,1} \\ a_{1,1} \\ a_{2,1} \end{Bmatrix} = \begin{bmatrix} \sum 1 & \sum i & \sum j \\ \sum i & \sum i^2 & \sum ij \\ \sum j & \sum ij & \sum j^2 \end{bmatrix}^{-1} \begin{Bmatrix} \sum \varphi_1 \\ \sum i\varphi_1 \\ \sum j\varphi_1 \end{Bmatrix} \tag{3.2}$$

The second order polynomial function of $\varphi(i,j)$ is:

$$\varphi_2(i,j) = a_{0,2} + a_{1,2}i + a_{2,2}j + a_{3,2}i^2 + a_{4,2}ij + a_{5,2}j^2 \tag{3.3}$$

where $a_{0,2}$, $a_{1,2}$, $a_{2,2}$, $a_{3,2}$, $a_{4,2}$, and $a_{5,2}$ are estimated by [56]:

$$\begin{Bmatrix} a_{0,2} \\ a_{1,2} \\ a_{2,2} \\ a_{3,2} \\ a_{4,2} \\ a_{5,2} \end{Bmatrix} = \begin{bmatrix} \sum 1 & \sum i & \sum j & \sum i^2 & \sum ij & \sum j^2 \\ \sum i & \sum i^2 & \sum ij & \sum i^3 & \sum i^2 j & \sum ij^2 \\ \sum j & \sum ij & \sum j^2 & \sum i^2 j & \sum ij^2 & \sum j^3 \\ \sum i^2 & \sum i^3 & \sum i^2 j & \sum i^4 & \sum i^3 j & \sum i^2 j^2 \\ \sum ij & \sum i^2 j & \sum ij^2 & \sum i^3 j & \sum i^2 j^2 & \sum ij^3 \\ \sum j^2 & \sum ij^2 & \sum j^3 & \sum i^2 j^2 & \sum ij^3 & \sum j^4 \end{bmatrix}^{-1} \begin{Bmatrix} \sum \varphi_2 \\ \sum i\varphi_2 \\ \sum j\varphi_2 \\ \sum i^2\varphi_2 \\ \sum ij\varphi_2 \\ \sum j^2\varphi_2 \end{Bmatrix} \tag{3.4}$$

The third order polynomial function is defined by:

$$\varphi_3(i,j) = a_{0,3} + a_{1,3}i + a_{2,3}j + a_{3,3}i^2 + a_{4,3}ij + a_{5,3}j^2 + a_{6,3}i^3 + a_{7,3}i^2 j + a_{8,3}ij^2 + a_{9,3}j^3 \tag{3.5}$$

where $a_{0,3}$, $a_{1,3}$, $a_{2,3}$, $a_{3,3}$, $a_{4,3}$, $a_{5,3}$, $a_{6,3}$, $a_{7,3}$, $a_{8,3}$, and $a_{9,3}$ are the coefficients to be estimated by the same least square estimation principle [56].

To determine which order polynomial is adequate for the phase adjustment, the root mean square e_{rms}, defined by Eq. (3.6), of the estimation error is applied.

$$e_{rms} = \sqrt{\frac{\sum_{i,j}\left(\varphi(i,j) - \varphi_k(i,j)\right)^2}{N}} \tag{3.6}$$

where k is the order of the polynomial function and N is the total number of data points in the integral phase map.

If the e_{rms} is small than a predefined threshold (for example, 0.2 rad which is experimentally verified to be sufficient in this study), the polynomial function is considered adequate for the phase adjustment. Otherwise, higher order polynomial function will be fitted using the least square method [56] until the e_{rms} is smaller than the threshold.

3.4. Example

The measurement of the surface on an automatic transmission valve body, as shown in Fig. 3.2, is used as an example of the laterally discontinuous surface to demonstrate the developed phase unwrapping method. The measurement area, as shown in Fig. 3.2(b), was 265 x 250 mm. The measurement result was represented in a matrix with the dimension of 892 x 842 pixels. The height measurement range was set as 0.3 mm. The lower right corner of the valve body was raised by a wedge to increase the height range of the valve body surface beyond 0.3 mm and generate the phase wrap.

3.4.1. Phase unwrapping results

The measured phase map is shown in Fig. 3.4. To unwrap the measured phase map in Fig. 3.4, the region-referenced phase unwrapping method described in Sec. 3.2 is applied. The 15 pixels reference region, as shown in Fig. 3.3(b), is utilized to identify the phase wrap. For each pixel, if more than 8 pixels in any of the four reference regions have the phase difference larger than 2π, that pixel is marked to have phase wrap. The masking and the 7x7 median filter for recovery, as discussed in Sec. 3.3.2, are applied on those boundary pixels with phase wrap to avoid the divergence problem on boundary pixels.

The dynamic segmentation with W = 50 pixels, W_o = 15 pixels, and T = 6 pixels, is applied to generate 18x17 (=306) segments. This segmentation generates 71 thin boundary regions. The dynamic segmentation is applied to move all four sides (top, bottom, right, and left) of the segments to reduce the number of thin boundary regions. In this example, 53 segments have at least one of the four sides moved once and 3

segments have at least one of the four sides moved twice. After the dynamic segmentation, only 5 thin boundary regions exist. These remaining thin boundary regions are marked by three arrows and two boxes (S_5 and S_6) in Fig. 3.9(a). Figures 3.9(b) and 3.9(c) illustrate the close-up view of the thin boundary regions in S_5 and S_6.

The dynamic segmentation was necessary to achieve a converged solution to phase unwrapping in this example. If only the static segmentation was used, the integral phase map was incorrect and the phase adjustment could not correct the errors in the integral phase map.

To recover the phase values in the five thin boundary regions shown in Fig. 3.9(a), the first and second order polynomial functions were applied to fit the integral phase map. Results of the fitted polynomial functions are $\varphi_1(i, j) = -1.521 + 0.006i + 0.013j$ with $a_{0,1} = -1.521$, $a_{1,1} = 0.006$, and $a_{2,1} = 0.013$, and $\varphi_2(i, j) = -0.497 + 0.003i + 0.010j + 4\times10^{-6}i^2 + 1\times10^{-7}ij + 4\times10^{-6}j^2$ with $a_{0,2} = -0.497$, $a_{1,2} = 0.003$, $a_{2,2} = 0.010$, $a_{3,2} = 4\times10^{-6}$, $a_{4,2} = 1\times10^{-7}$, and $a_{5,2} = 4\times10^{-6}$.

The root mean square e_{rms} is calculated to determine which order of the polynomial function is adequate for the phase adjustment. The e_{rms} for the first and second order polynomials are 0.33 rad and 0.16 rad, respectively, with the total number of data points $N = 191131$. Because the second order polynomial has the e_{rms} smaller than the predefined threshold 0.2 rad, this polynomial is used for the phase adjustment.

The difference is calculated between the existing phase values and the estimated values of $\varphi_2(i, j)$ in the thin boundary regions. The multiple of 2π is added to or subtracted from those pixels in the thin boundary regions to make the difference smaller than 2π. For example, in S_5 and S_6, 2π was subtracted from both regions to bring the phase values from the level of 15 rad to 9 rad and from the 9 rad to 3 rad, respectively. Figure 3.9(d) shows the integral phase map after the phase adjustment. The close-up views of the two regions S'_5 and S'_6 in Fig. 3.9(d) are shown in Figs. 3.9(e) and 3.9(f), respectively. The errors have been removed and the whole phase unwrapping process is complete.

3.4.2. Effect of W and W_o on computational efficiency

Two sets of the numerical experiments to study the effect of W and W_o on computational efficiency are conducted and results are summarized in Table 3.1. The W_o is fixed at 25 pixels in the first set of test. The reduction of W from 150 to 30 pixels improves the computational time from 38 to 15 minutes using a common personal computer with the MATLAB software. A smaller size segment requires less computational time for phase unwrapping. However, reducing W increases the number of segments and will eventually increase the computational time. As shown in Table 3.1, when W is reduced to 29 pixels, the computation time is increased to 16 min. When W is smaller than 29 pixels, the phase unwrapping method diverges.

The second set of the numerical experiment is conducted by fixing W and reducing W_o. With a fixed W at 40 pixels, as shown in Table 3.1, the reduction of W_o from 25 to 10 pixels further reduces the computational time to 6 min while the number of segments remains the same at 506. As W_o reduces, the size of segments after dynamic segmentation becomes smaller and makes the phase unwrapping of each segment faster. The total computational time is reduced. When W_o is smaller than 10 pixels (W = 40 pixels), the divergence problem occurs.

3.4.3. Convergence

The convergence of the phase unwrapping method is also investigated. As shown in Table 3.2, for W at 50, 40, and 29, the minimum W_o without the divergence problem are 10, 10, and 24, respectively, for the automatic transmission valve body example. When W reduces from 50 to 40 pixels, the minimum W_o is the same (10 pixels) to make the phase unwrapping method converge. When W reduces from 40 to 29 pixels, the minimum W_o increases to 24 pixels. This is likely due to the increase in the number of boundary pixels in smaller segments makes the region-referenced phase unwrapping more prone to divergence.

This example demonstrates the importance of selecting W and W_o to improve computational efficiency without compromising the stability in phase unwrapping. The selection of W and W_o will change for different applications. The basic principle learned

in this example is to use an optimal W which balances the number of segments and computational time in each segment. Small W_o without triggering the instability is desired.

3.5. Concluding remarks

A new phase unwrapping method was developed to mathematically increase the height measurement range of the laser holographic interferometry while maintaining the same level of accuracy and resolution. This method had successfully solved the phase unwrapping problem of the laterally discontinuous surfaces using an example of the automatic transmission valve body. Three new approaches, including the masking and recovery, dynamic segmentation, and phase adjustment for pixels in thin boundary regions, had demonstrated to be effective to avoid the divergence problem of boundary pixels. A guideline was developed to select the size of segment for improving the computational efficiency without convergence problem.

This phase unwrapping method, together with the hologram registration method developed by Huang et al. [53], can successfully increase the measurement volume for laser holographic interferometry measurements. The phase unwrapping method increases the height and the hologram registration method expands the field of view.

Two research investigations can be further developed to advance the laser holographic interferometry measurement system. For measuring objects with height discontinuity, the 3D CAD model or predetermined (a priori) value on the discontinuity point can be used in phase unwrapping. The adaptive filtering of the phase map [58] can also be applied to improve the noise robustness.

Table 3.1. Computational time for phase unwrapping of the automatic transmission valve body example (892 x 842 pixels).

Size of segments, W (pixels)	Width of overlapped regions, W_o (pixels)	Number of segments	Computational time (min)
150	25	36	38
100	25	81	25
50	25	306	18
40	25	506	15
30	25	870	15
29	25	930	16
40	20	506	12
40	15	506	9
40	10	506	6

Table 3.2. Minimum W_o for phase unwrapping without divergence in the automatic transmission valve body example.

W (pixels)	Minimum W_o (pixels) without divergence
50	10
40	10
29	24

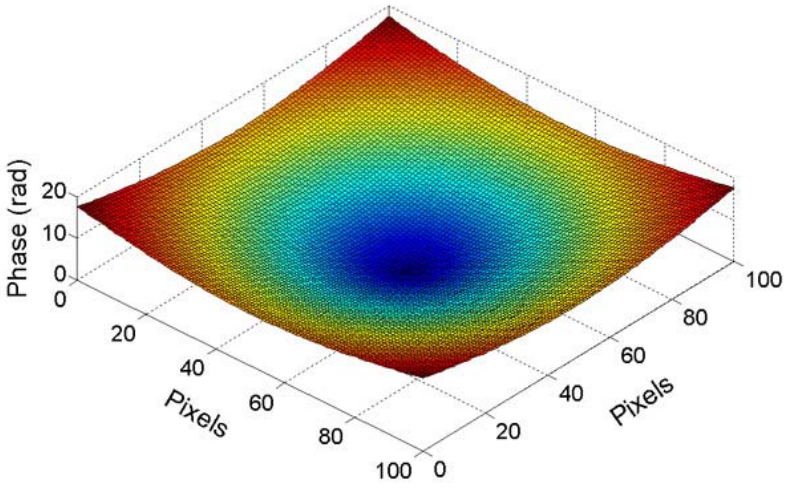

(a)

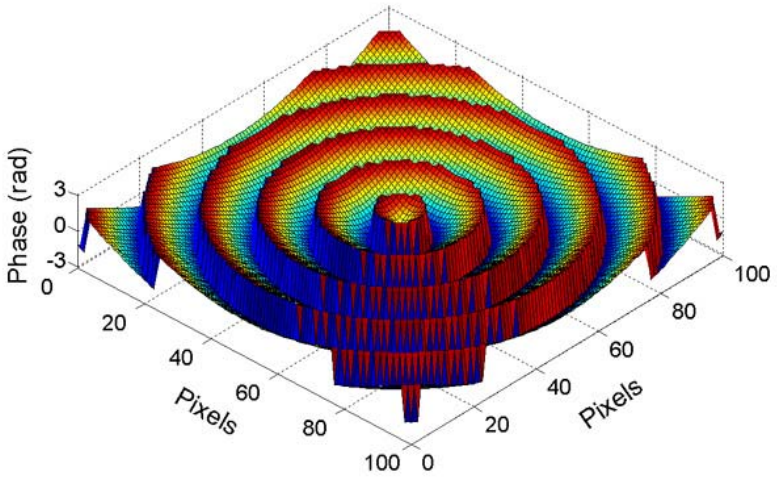

(b)

Fig. 3.1. Artificially created phase map: (a) 3D true phase map without phase wrap and (b) 3D wrapped phase map.

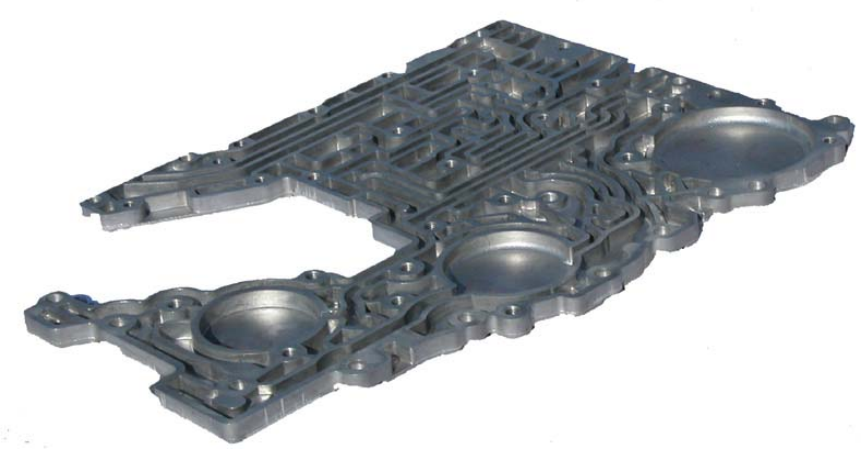

(a)

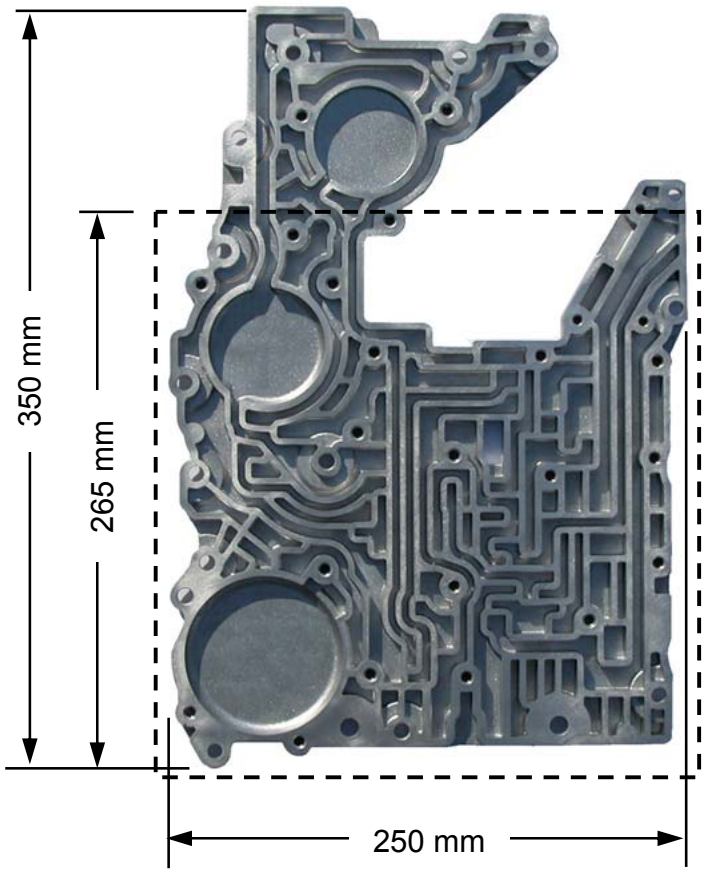

(b)

Fig. 3.2. The automatic transmission valve body: (a) isometric view and (b) top view.

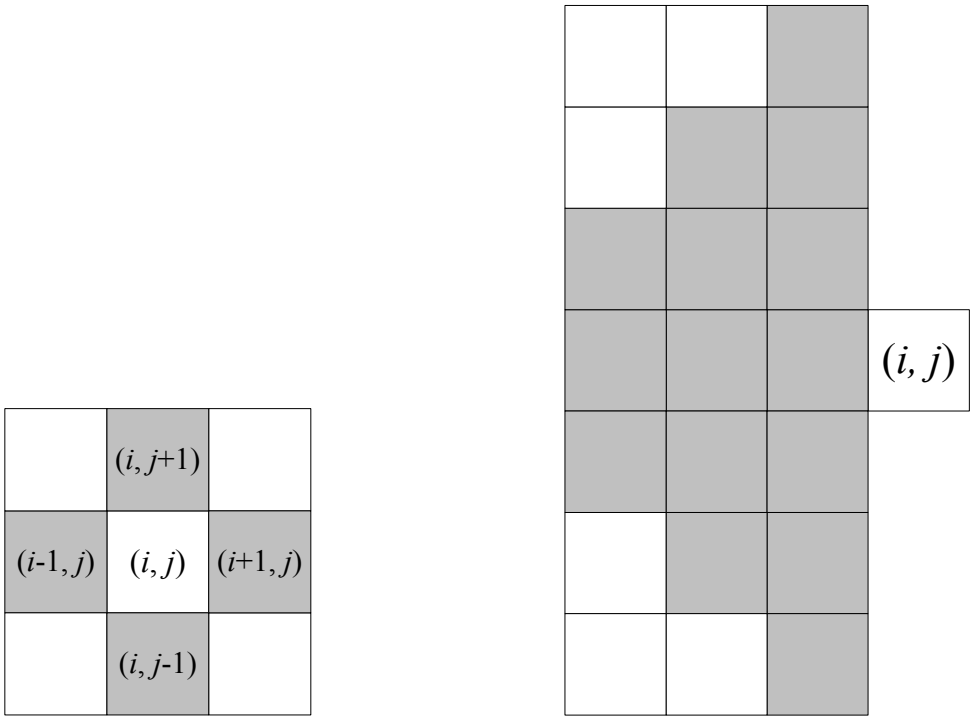

Fig. 3.3. Detection of phase wrap at pixel (i, j): (a) surrounding four pixels and (b) reference region surrounding the pixel.

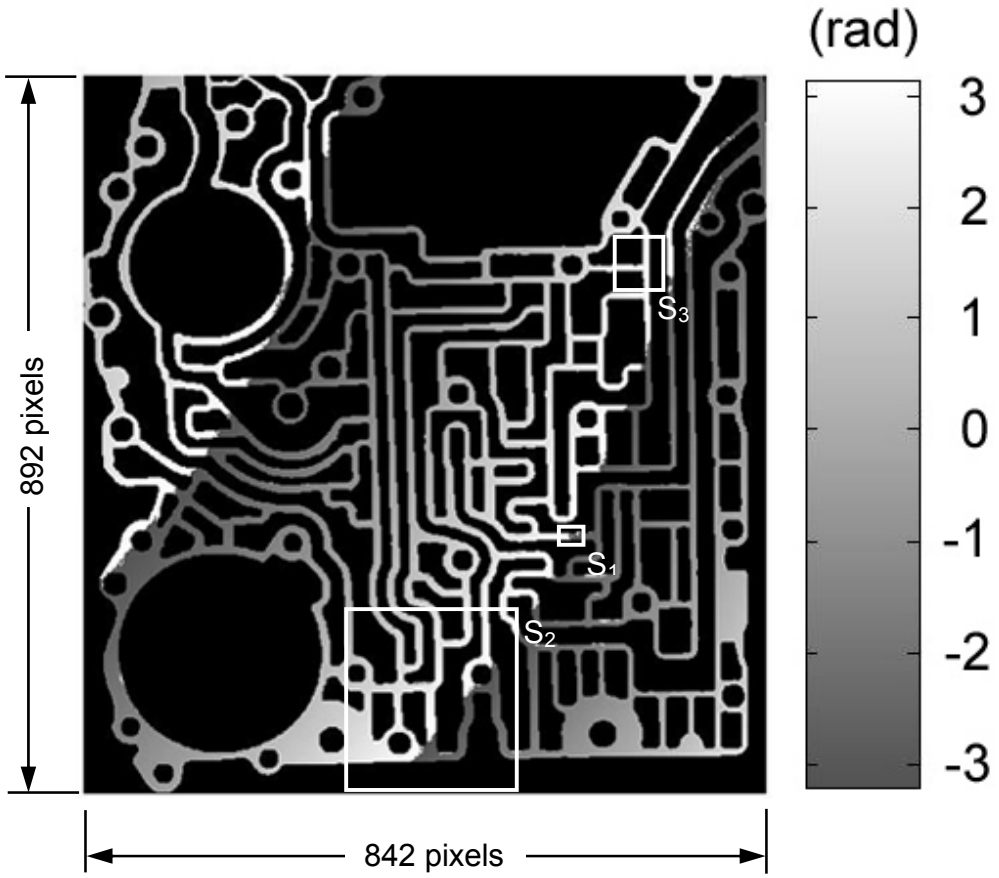

Fig. 3.4. Measured phase map with phase wrap for the automatic transmission valve body.

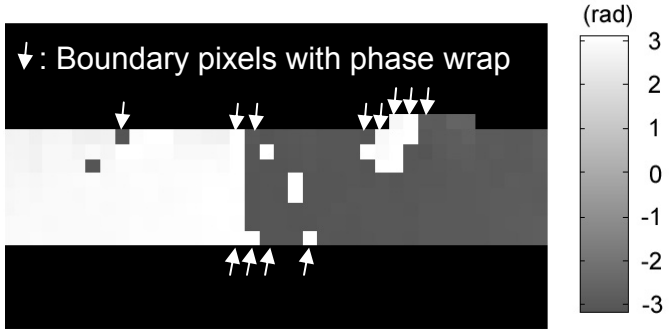

(a)

(b)

(c)

Fig. 3.5. Close-up view of the region S_1 in Fig. 3.4 as an example of the boundary pixels with decreased noise robustness in the detection of phase wrap: (a) before phase unwrapping, (b) after phase unwrapping and before recovery, and (c) after phase unwrapping and recovery.

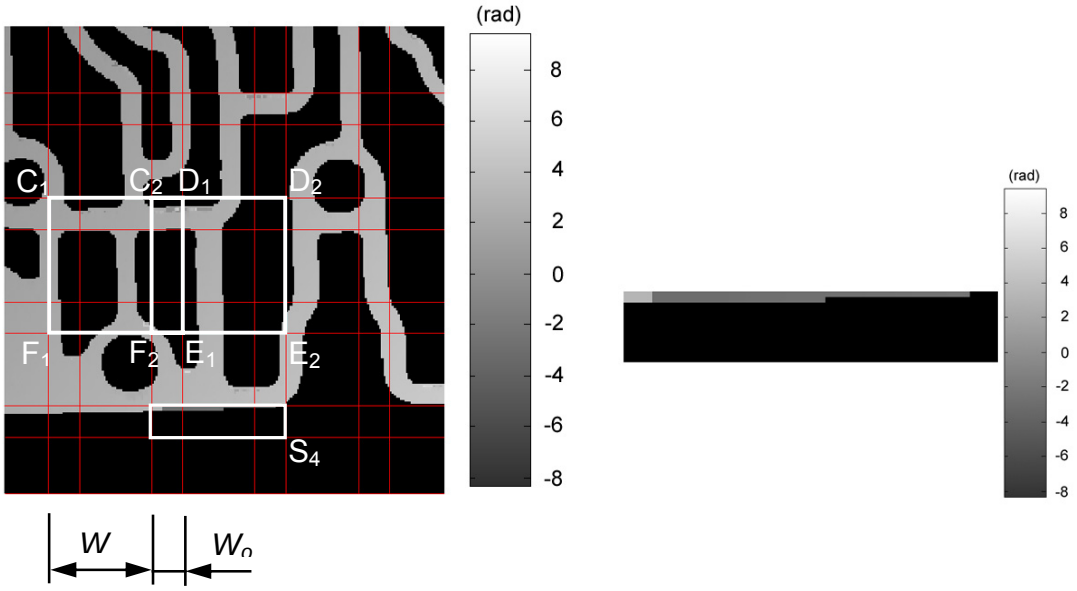

(a) (b)

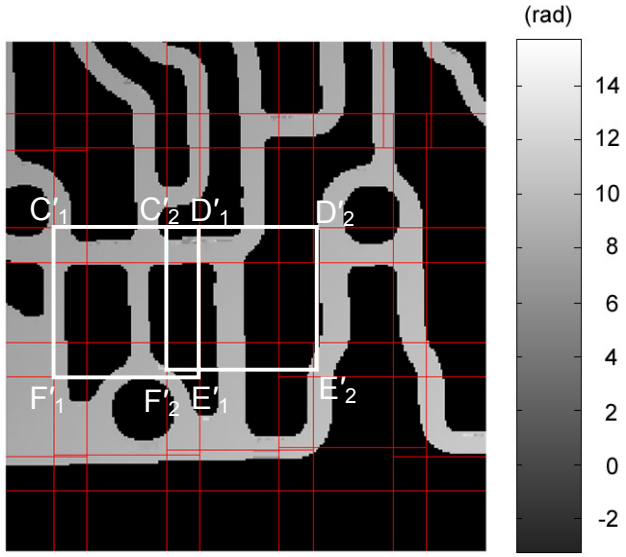

(c)

Fig. 3.6. Segmentation: (a) static segmentation of the region S_2 in Fig. 3.4, (b) close-up view of the region S_4 in Fig. 3.6(a), and (c) dynamic segmentation of the region S_2 in Fig. 3.4.

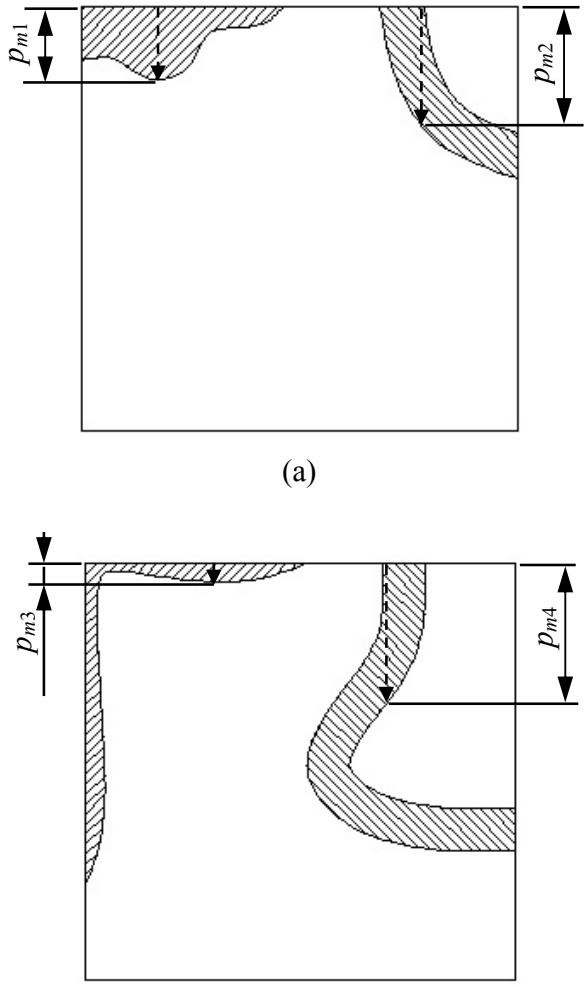

Fig. 3.7. Definition of the boundary width p_m: (a) two boundary regions and (b) the condition with pixels on the top side close to the left side of the segment.

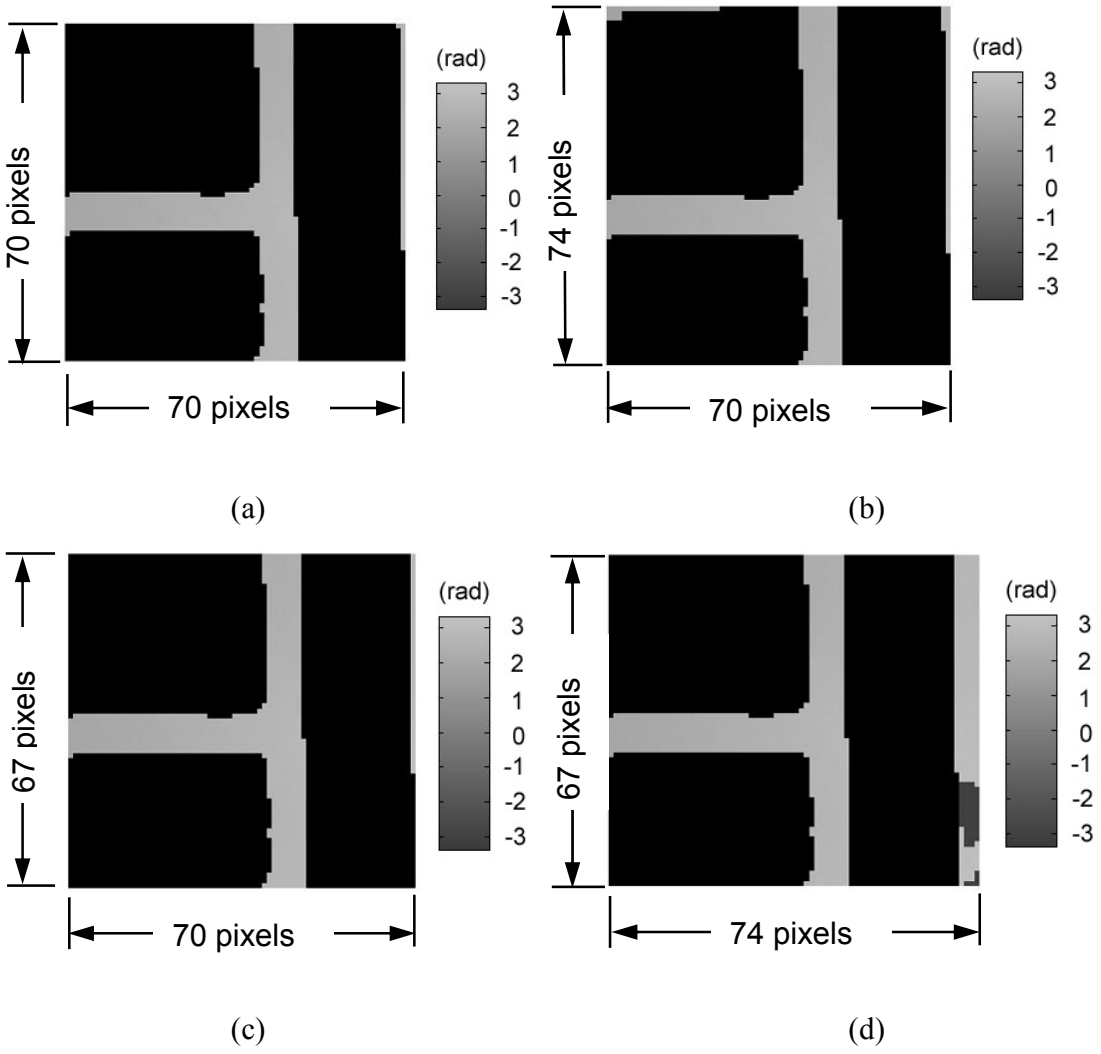

Fig. 3.8. Example of the dynamic segmentation of region S_3 in Fig. 3.4 ($W = 50$, $W_o = 20$, and $T = 6$ pixels).

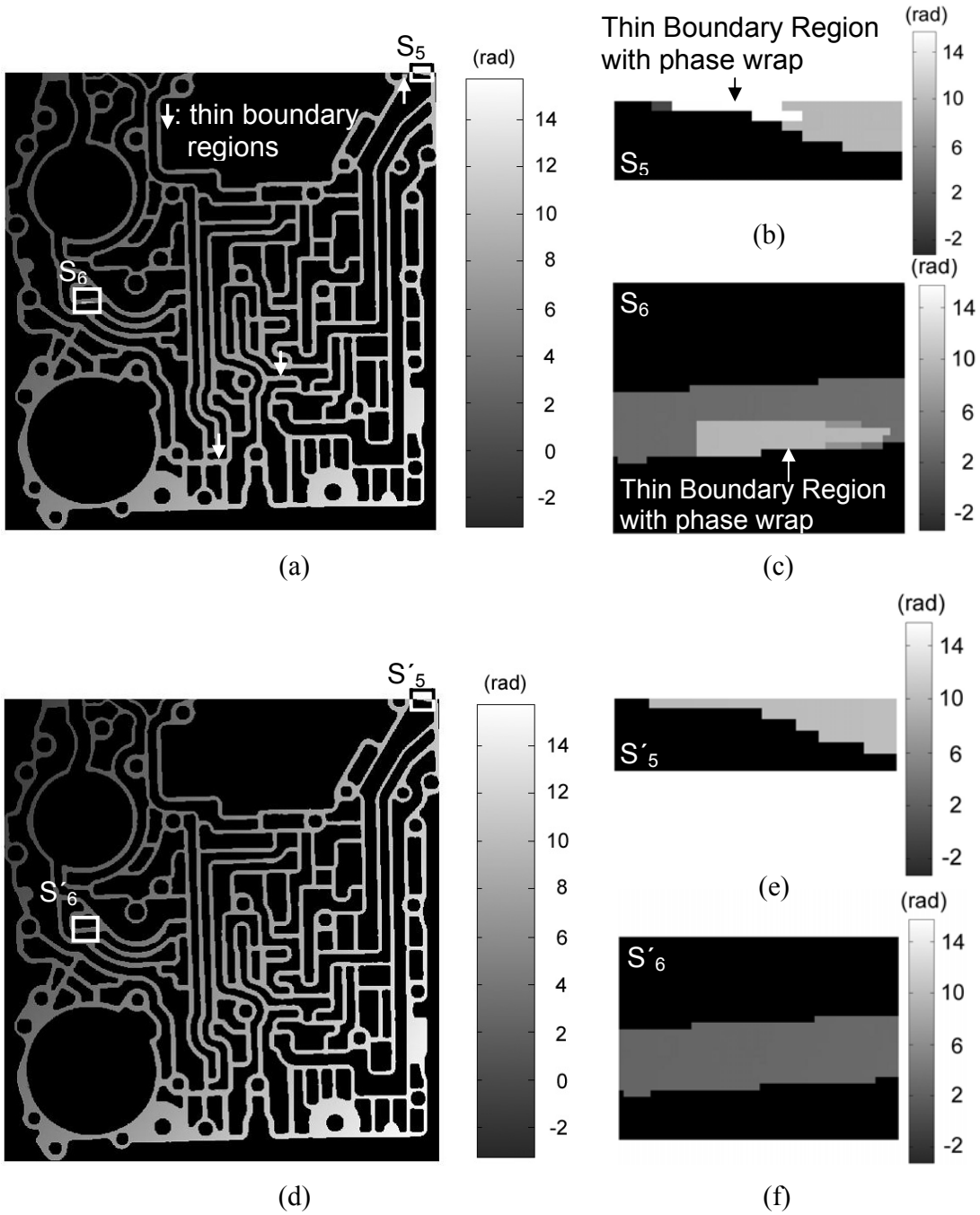

Fig. 3.9. Phase unwrapping of the automatic transmission valve body: (a) unwrapped phase map without adjustment, (b) close-up view of the region S_5 in (a), (c) close-up view of the region S_6 in (a), (d) unwrapped phase map after adjustment, (e) close-up view of the region S'_5 in (d) after adjustment, and (f) close-up view of the region S'_6 in (d) after adjustment.

Chapter 4

Laser Holographic Interferometry Measurement of Cylinders

4.1. Introduction

Round shape is an important surface geometry. About 70% of all engineering components have an axis of rotational symmetry in them somewhere [34]. To evaluate the surface geometry, the roundness for two-dimensional (2D) circle and the cylindricity for three-dimensional (3D) cylinder are developed. Currently, the contact-based measurement [59-63] is widely utilized to evaluate the roundness and cylindricity due to its simple implementation and flexibility. However, the contact-based cylindricity measurement delivers only limited number of cross-sections along the axis of the cylinder surface to save the inspection time and cost. Some possibly important features between two adjacent cross-sections of the cylinder surface may be missing. The measurement time is dependent on the number of cross-sections to be measured.

A non-contact optical-based cylindricity measurement method was developed [64]. This method applied the interferometry to measure the cylinder surface at grazing incidence. The interference pattern of a master cylinder with negligible cylindricity errors is compared with that of the sample cylinder to obtain the surface geometry of the sample cylinder. The grazing incidence configuration of this method limits the axial length of the cylinder surface which can be measured. To avoid the ambiguity, the diameter of the sample cylinder should match the known diameter of the master cylinder within a wavelength [64]. This restricted the flexibility of the measurement system.

A new mathematical method is developed to utilize the laser holographic interferometry system [65] for cylindricity measurement of cylinders with variable diameters. The mathematical model is presented in Sec. 4.2. In Sec. 4.3, the calibration

process is discussed. Simulations and experiment are conducted to demonstrate the feasibility of the developed method in Sec. 4.4.

4.2. Mathematical model

The mathematical model is based on the customized design of a laser holographic interferometry system. This model transforms the measurement data from the laser holographic interferometry into the 3D Cartesian representation of the cylinder surface. The cylindricity of the cylinder surface is then evaluated.

4.2.1. System design

The regular laser holographic interferometry system for the flat object measurement is shown in Fig. 4.1(a). This system, which can successfully measure the flat surfaces of machined metals with μm-level accuracy [65], is composed of three major components, the vibration isolated table, the optical measurement unit, and the off-axis parabolic mirror. The vibration isolated table supports the optical measurement unit and the measurement object. The diverging light coming from the optical measurement unit is collimated by the parabolic mirror and directed to the measurement object directly. The light reflected from the measurement object carries the height information of the object, interferes with the reference light in the optical measurement unit, and generates the interference pattern. Fourier transformation [65] is applied to analyze the interference pattern and the 3D surface profile of the flat measurement object is generated.

A cylindrical lens, as shown in Fig. 4.1(b), is applied to customize the optical system for the cylindricity measurement. Without the cylindrical lens, small amount of the collimated light coming down from the parabolic mirror can be reflected back from the round object surface due to the large surface curvature. An ideal cylindrical lens changes the incident parallel light beam into a converging beam and focuses at a straight line. With this cylindrical lens, a cylinder can be positioned with the center axis very close to the focus line of the cylindrical lens as shown in Fig. 4.1(b). The converging light beam from the cylindrical lens hits the cylinder surface in the direction close to

normal and is reflected back through the cylindrical lens to convert into parallel light beam again. The converted parallel light beam after the cylindrical lens follows the same path as for the flat surface to generate the interference pattern in the optical measurement unit.

The cylindrical lens virtually converts the cylindrical surface into flat shape. To the optical measurement unit, the cylindrical measurement object is still flat. The same Fourier transformation described above is applied and the calculated value of each measured point relates to the distance from the corresponding point on the cylindrical measurement object surface to the focus line of the cylindrical lens.

Only a section of the whole circumference of the cylindrical surface can be covered in each measurement with the cylindrical lens configured as shown in Fig. 4.1(b). A rotational stage will be used to hold the cylinder and precisely change its angular positions. The developed mathematical model is applied to convert the measurement data from the laser holographic interferometry into the 3D Cartesian representation of the cylindrical measurement object surface.

4.2.2. Mathematical deduction

The geometric relations between the cylindrical lens, the rotational stage, and the cylinder are defined in the mathematical model. The format of the measurement data by the laser holographic interferometry is described. The mathematical transformation is derived to convert the measurement data into 3D Cartesian representation of the cylinder surface.

4.2.2.1. Geometric relation definition

The 3D positions of the cylindrical lens focus line, the rotational stage center axis, and the cylinder center axis do not match in practice. Figure 4.2 is a 3D illustration of the geometric relations in this configuration. The positions are referred to a common Cartesian coordinate system with the origin at $\mathbf{O}(0, 0, 0)$. This coordinate system is predefined by the laser holographic interferometry measurement system. The center axis of the rotational stage goes through the point denoted as $\mathbf{O}_0(x_0, y_0, z_0)$ and follows the

direction denoted as $\mathbf{D}_0(a_0, b_0, c_0)$. The cylinder center goes through the point denoted as $\mathbf{O}_1(x_1, y_1, z_1)$ and follows the direction denoted as $\mathbf{D}_1(a_1, b_1, c_1)$. As the rotational stage rotates the cylinder, the position of $\mathbf{O}_1(x_1, y_1, z_1)$ and the direction $\mathbf{D}_1(a_1, b_1, c_1)$ will change. The focus line of the cylindrical lens goes through the point denoted as $\mathbf{O}_2(x_2, y_2, z_2)$ and follows the direction denoted as $\mathbf{D}_2(a_2, b_2, c_2)$. The focal length of the cylindrical lens is R_0.

The collimated light travels down and reaches the cylindrical lens, which converts the collimated light into converging light. The converging light, which virtually focuses at a line going through the point $\mathbf{O}_2$ and following the direction $\mathbf{D}_2$, reaches the cylinder and covers the region on the cylinder surface marked by hexagons in Fig. 4.2. The reflected light from the cylinder surface travels through the cylindrical lens and converts into collimated light to generate the interference pattern in the optical measurement unit for calculation of "height," which relates to the distance from the cylinder surface to the focus line of the cylindrical lens.

It is assumed that the true values of the parameters $\mathbf{O}_1(x_1, y_1, z_1)$, $\mathbf{D}_1(a_1, b_1, c_1)$, $\mathbf{O}_2(x_2, y_2, z_2)$, $\mathbf{D}_2(a_2, b_2, c_2)$, and R_0 are known for the conversion of measurement data. In Sec. 4.3, the calibration process is elaborated to estimate these values.

4.2.2.2. Format of measurement data

The measurement data from the laser holographic interferometry system is delivered in a matrix. For flat surface measurement, the row and column positions of each element in the matrix linearly correspond to the x and y coordinates of the point on the object surface, respectively. The value of each element in the matrix indicates the height of the corresponding point on the object surface. The heights of all the data points are measured relative to a reference point, which has the height value equal to zero in the matrix.

For the cylindricity measurement with the configurations shown in Fig. 4.2, the row and column positions of each element in the matrix correspond to the x and y coordinates of the point on the cylindrical lens. The value of each element in the matrix indicates the distance from the point on the cylinder to the focus line of the cylindrical

lens minus a constant shift, denoted as S. This constant shift S is the distance from the reference point, denoted as $\mathbf{P}_r$, to the focus line of the cylindrical lens. In the matrix, the value of the reference point is zero.

4.2.2.3. Data conversion

The measurement data of a cylinder from the laser holographic interferometry should be converted into Cartesian form to represent a 3D cylinder surface and calculate the cylindricity.

The conversion is composed of three steps. First, the point on the focus line of the cylindrical lens and the optical path, which relates to an element in the measurement matrix, is calculated. For example, the point $\mathbf{P}_m$ on the cylindrical lens, as shown in Fig. 4.2, has the coordinates (x_m, y_m, z_m), in which x_m and y_m can be calculated from the row and column positions of the corresponding element in the measurement matrix. The collimated light reaches $\mathbf{P}_m$ and follows the illustrated path to reach the point $\mathbf{P}_o$ with the coordinate (x_o, y_o, z_o) on the cylinder. This path virtually converges to the point $\mathbf{P}_c$ with the coordinate (x_c, y_c, z_c) on the focus line of the cylindrical lens. With the (x_m, y_m) data of the point $\mathbf{P}_m$, the known focal length R_0 of the cylindrical lens, the point $\mathbf{O}_2$ (x_2, y_2, z_2), and the direction $\mathbf{D}_2$ (a_2, b_2, c_2), the 3D coordinate of the point $\mathbf{P}_c$ and the direction vector from $\mathbf{P}_c$ to $\mathbf{P}_m$ can be determined. Second, the relative 3D coordinates of the point $\mathbf{P}_o$ on the cylinder surface is calculated with the value, denoted as d_0, of the element in the measurement matrix corresponding to the point $\mathbf{P}_m$, the known constant shift S, and the calculated 3D coordinate of the point $\mathbf{P}_c$. Third, the calculated 3D coordinate of the point $\mathbf{P}_o$ is rotated about the center axis of the rotational stage with the angular position of the cylinder to compensate its angular position change in different measurements.

The point $\mathbf{P}_c$ (x_c, y_c, z_c) on the focus line of the cylindrical lens is determined by:

$$\begin{cases} x_c = x_2 + a_2 t \\ y_c = y_2 + b_2 t \\ z_c = z_2 + c_2 t \end{cases} \tag{4.1}$$

where t is the scalar parameter to be determined.

The distance from the point $\mathbf{P}_c$ on the focus line of the cylindrical lens to the point $\mathbf{P}_m$ on the cylindrical lens is R_0. This relation is expressed by

$$(x_m - x_c)^2 + (y_m - y_c)^2 + (z_m - z_c)^2 = R_0^2 \tag{4.2}$$

The direction from the point $\mathbf{P}_c$ to $\mathbf{P}_m$ is perpendicular to the direction of the focus line of the cylindrical lens. This relation is expressed by

$$a_2(x_m - x_c) + b_2(y_m - y_c) + c_2(z_m - z_c) = 0 \tag{4.3}$$

Combine Eqs. (4.1)-(4.3) and a two-degree equation of t is formulated:

$$\begin{aligned} &t^2\left[a_2^4 + b_2^4 + 2a_2^2b_2^2 + a_2^2c_2^2 + b_2^2c_2^2\right] + \\ &2t\left[\left(a_2^2 + b_2^2\right)\left(x_2a_2 + y_2b_2 - x_ma_2 - y_mb_2\right) - (x_m - x_2)a_2c_2^2 - (y_m - y_2)b_2c_2^2\right] + \\ &\left[\left(x_2a_2 + y_2b_2 - x_ma_2 - y_mb_2\right)^2 - R_0^2c_2^2 + (x_m - x_2)^2c_2^2 + (y_m - y_2)^2c_2^2\right] = 0 \end{aligned} \tag{4.4}$$

The coefficients of t in each term of Eq. (4.4) are known or measurable and Eq. (4.4) can be solved. There are two roots to the Eq. (4.4). The larger root is always selected with the assumption that the point $\mathbf{O}_2$ is on the beginning side of the cylinder in the direction of $\mathbf{D}_2$.

With the calculated solution to t, the coordinate of the point $\mathbf{P}_c$ is calculated using Eq. (4.1) and the z_m coordinate of the point $\mathbf{P}_m$ is calculated using Eq. (4.3).

The element, corresponding to the point $\mathbf{P}_m$ on the cylindrical lens, in the measurement matrix has the value d_o. The d_o plus the constant shift S is the distance from the point $\mathbf{P}_o$ to the point $\mathbf{P}_c$. The 3D coordinate of the point $\mathbf{P}_o$ is calculated by

$$\mathbf{P}_o = \mathbf{P}_c + \frac{\mathbf{P}_m - \mathbf{P}_c}{\left|\mathbf{P}_m - \mathbf{P}_c\right|}\left(d_o + S\right) \tag{4.5}$$

As the rotational stage rotates the cylinder, the center of the rotational stage and the focus line of the cylindrical lens are stationary, but the center of the cylinder changes and the measured surface region on the cylinder is different.

The rotation is conducted to compensate the angular position change of the cylinder. In practice, the cylinder rotates about the rotational stage center and the cylindrical lens is fixed. In the model, the cylinder is assumed fixed and the cylindrical lens is rotated reversely about the center axis of the rotational stage. This assumption does not change the calculated 3D representation of the cylinder surface because the movement is relative. Let θ be the angular position of the cylinder, $-\theta$ is the angular position of the cylindrical lens about the center axis of the rotational stage. The transformation about the center axis of the rotational stage is defined by [66]

$$\mathbf{P}_o^T = \mathbf{O}_2 + \left(\mathbf{P}_o - \mathbf{O}_2\right)\cos(-\theta) + \mathbf{D}_2\left(\mathbf{D}_2 \cdot \left(\mathbf{P}_o - \mathbf{O}_2\right)\right)\left(1 - \cos(-\theta)\right) + \mathbf{D}_2 \times \left(\mathbf{P}_o - \mathbf{O}_2\right)\sin(-\theta) \tag{4.6}$$

where $\mathbf{P}_o^T$ is the coordinate of the point $\mathbf{P}_o$ after the transformation by angular rotation $-\theta$ about the center axis of the rotational stage.

Each element in the measurement matrix at every angular position of the cylinder is converted using the method described above to reach the 3D coordinate $\mathbf{P}_o^T$. All the converted $\mathbf{P}_o^T$ form a 3D discrete representation of the cylinder surface in the Cartesian

coordinate system. Based on this 3D representation, the cylindricity of the cylinder can be evaluated.

4.2.3. Cylindricity evaluation

Many cylindricity evaluation methods, based on least square and minimum zone [67-70], have been developed. The least square evaluation with Gauss-Newton iteration is applied to estimate the cylindricity because the estimated reference cylinder using this method is unique and robust to a few isolated noisy points [34]. The reference cylinder, from which the deviations of all the measured points are determined, should be identified to calculate the cylindricity. The cylindricity is defined as the range of the deviations of all the measured points from the reference cylinder. This cylindricity evaluation method starts with an initial guess of the reference cylinder and conducts iterations until the estimation of the reference cylinder (radius and position of center axis) converges within a predefined error.

Some transformations of the data points are conducted at the beginning of each iteration to simplify the process. The data points are translated and rotated at the beginning of each iteration to make the trial reference cylinder of this iteration have its center axis lie on the *y* axis. The Jacobian matrix is calculated to identify the incremental step for each parameter estimate. Update the parameter estimates for the next iteration by adding the incremental step to each parameter with the reverse transformations.

The translation and rotation are conducted to make the center axis of the reference cylinder lie on the *y* axis.

The translation of the data points is achieved by:

$$\begin{pmatrix} x_{oi} \\ y_{oi} \\ z_{oi} \end{pmatrix} := \begin{pmatrix} x_{oi} \\ y_{oi} \\ z_{oi} \end{pmatrix} - \begin{pmatrix} x_1 \\ y_1 \\ z_1 \end{pmatrix} \tag{4.7}$$

where

the operator := means update the parameters on the left side,

i is the number of converted points $\mathbf{P}_{o,i}^{\mathbf{T}}$, $i = 1,2,\ldots, N$, and

N is the total number of measured points.

The rotation of the data points is achieved by:

$$\begin{pmatrix} x_{oi} \\ y_{oi} \\ z_{oi} \end{pmatrix} := \mathbf{U} \begin{pmatrix} x_{oi} \\ y_{oi} \\ z_{oi} \end{pmatrix} \tag{4.8}$$

where

$\mathbf{U}$ is the rotation matrix $\mathbf{U} = \begin{pmatrix} 1 & 0 & 0 \\ 0 & \cos\theta_2 & \sin\theta_2 \\ 0 & -\sin\theta_2 & \cos\theta_2 \end{pmatrix} \begin{pmatrix} \cos\theta_1 & \sin\theta_1 & 0 \\ -\sin\theta_1 & \cos\theta_1 & 0 \\ 0 & 0 & 1 \end{pmatrix}$,

θ_1 is the angle to be rotated around the z axis, and

θ_2 is the angle to be rotated around the x axis.

The angles θ_1 and θ_2 are determined by the condition:

$$\mathbf{U} \begin{pmatrix} a_1 \\ b_1 \\ c_1 \end{pmatrix} = \begin{pmatrix} 0 \\ 1 \\ 0 \end{pmatrix} \tag{4.9}$$

Eq. (4.9) defines the transformation which makes the direction $\mathbf{D}_1(a_1, b_1, c_1)$ of the center axis of the cylinder parallel to the y axis (0, 0, 1).

The data points can be reversely transformed by:

$$\begin{pmatrix} x_{oi} \\ y_{oi} \\ z_{oi} \end{pmatrix} := \mathbf{U}^{\mathbf{T}} \begin{pmatrix} x_{oi} \\ y_{oi} \\ z_{oi} \end{pmatrix} + \begin{pmatrix} x_1 \\ y_1 \\ z_1 \end{pmatrix} \tag{4.10}$$

where $\mathbf{U}^{\mathbf{T}}$ is the transpose of the matrix $\mathbf{U}$.

To identify the incremental step of each parameter estimate for next iteration, the Jocobian matrix is calculated by

$$\mathbf{J} = \begin{pmatrix} \frac{\partial q_1}{\partial x_1} & \frac{\partial q_1}{\partial z_1} & \frac{\partial q_1}{\partial a_1} & \frac{\partial q_1}{\partial c_1} & \frac{\partial q_1}{\partial r_1} \\ & & \cdots & & \\ \frac{\partial q_n}{\partial x_1} & \frac{\partial q_n}{\partial z_1} & \frac{\partial q_n}{\partial a_1} & \frac{\partial q_n}{\partial c_1} & \frac{\partial q_n}{\partial R_1} \end{pmatrix} \tag{4.11}$$

where

$$q_i = r_i - R_1, \tag{4.12}$$

$$r_i = \begin{Bmatrix} [c_1(y_{oi} - y_1) - b_1(z_{oi} - z_1)]^2 + \\ [a_1(z_{oi} - z_1) - c_1(x_{oi} - x_1)]^2 + \\ [b_1(x_{oi} - x_1) - a_1(y_{oi} - y_1)]^2 \end{Bmatrix}^{1/2} \Big/ \left(a_1^2 + b_1^2 + c_1^2\right)^{1/2}, \tag{4.13}$$

R_1 is the radius of the reference cylinder.

With the center axis of the reference cylinder lie on the y axis, $a_1 = 0$, $b_1 = 1$, $c_1 = 0$, $x_1 = 0$, and $y_1 = 0$. Eq. (4.13) can be simplified as

$$r_i = \sqrt{x_{oi}^2 + z_{oi}^2} \tag{4.14}$$

And each element in the Jacobian matrix **J**, described in Eq. (4.11), can have a significantly simplified expression:

$$\begin{aligned}
&\frac{\partial q_i}{\partial x_1} = -\frac{x_{oi}}{r_i}, \\
&\frac{\partial q_i}{\partial z_1} = -\frac{z_{oi}}{r_i}, \\
&\frac{\partial q_i}{\partial a_1} = -\frac{x_{oi} y_{oi}}{r_i}, \\
&\frac{\partial q_i}{\partial c_1} = -\frac{y_{oi} z_{oi}}{r_i}, \\
&\frac{\partial q_i}{\partial R_1} = -1 .
\end{aligned} \tag{4.15}$$

The incremental steps of the parameter estimates are determined by

$$\begin{pmatrix} I_{x_1} \\ I_{z_1} \\ I_{a_1} \\ I_{c_1} \\ I_{R_1} \end{pmatrix} = \left(\mathbf{J}^{\mathrm{T}}\mathbf{J}\right)^{-1} \begin{pmatrix} -q_1 \\ \ldots \\ -q_n \end{pmatrix} \tag{4.16}$$

The parameter estimates are updated by

$$\begin{pmatrix} x_1 \\ y_1 \\ z_1 \end{pmatrix} := \begin{pmatrix} x_1 \\ y_1 \\ z_1 \end{pmatrix} + \mathbf{U}^{\mathbf{T}} \begin{pmatrix} I_{x_1} \\ -I_{x_1} I_{b_1} - I_{z_1} I_{c_1} \\ I_{z_1} \end{pmatrix},$$

$$\begin{pmatrix} a_1 \\ b_1 \\ c_1 \end{pmatrix} := \mathbf{U}^{\mathbf{T}} \begin{pmatrix} I_{a_1} \\ 1 \\ I_{c_1} \end{pmatrix}, \text{ and} \tag{4.17}$$

$$R_1 := R_1 + I_{R_1}.$$

4.2.4. Registration adjustment

The registration adjustment is developed to reduce the effect of parameter estimate errors on the cylindricity evaluation. In the process described above, the true values of all the parameters are assumed to be known. In practice, these values have to be estimated or measured with some errors. The registration adjustment is applied before the cylindricity calculation of the whole cylinder to transform the converted 3D data points of each measurement so that the center axis of the reference cylinders of all the measurements match with each other.

The center axis of the fitted cylinder of each measurement is estimated using the cylindricity calculation iteration process described in Sec. 4.2.3. For example, the center point and the direction of the center axis are estimated as $\mathbf{O}_{1k}$ and $\mathbf{D}_{1k}$ for measurement k. The means of $\mathbf{O}_{1k}$ and $\mathbf{D}_{1k}$, denoted as $\overline{\mathbf{O}}_1$ and $\overline{\mathbf{D}}_1$, respectively, are the target axis position for all the measurements. The transformation of the data points for each measurement is determined by

$$\begin{pmatrix} x_{oi} \\ y_{oi} \\ z_{oi} \end{pmatrix} = \mathbf{T}\left(\begin{pmatrix} x_{oi} \\ y_{oi} \\ z_{oi} \end{pmatrix} - \overline{\mathbf{O}}_1 \right) + \overline{\mathbf{O}}_1 \tag{4.18}$$

where $\mathbf{T}_i$ is the rotation matrix determined by $\overline{\mathbf{D}}_1 = \mathbf{T}_k \mathbf{D}_{1k}$.

4.3. Calibrations

Calibrations are conducted to estimate the position of the rotational stage center axis, the position of the focus line of the cylindrical lens, the focal length of the cylindrical lens, and the constant shift of the reference point, which are assumed to be known in the mathematical model described in Sec. 4.2.

A master cylinder with known radius and negligible cylindricity errors is used for the calibrations. The cylindricity of the master cylinder is calculated using the mathematical model described in Sec. 4.2 with the initial guess of all the parameters to be estimated. Within the possible range of all the parameters to be estimated, iterations are conducted to find an optimal combination of these parameters, which deliver the minimum cylindricity error. This optimal combination of these parameters will be used for the mathematical model. Multiple randomly-selected initial guess combinations of the parameters are used to reduce the sensitivity of the converged results to the initial guess.

The computational time of this calibration may be long but this is a one-time process and can be implemented offline. Once all the parameters are calibrated, the master cylinder is released. Without changing the relative locations between the rotational stage and the cylindrical lens, a sample cylinder with variable diameters is fixed. It is important to note that the center of the sample cylinder does not have to be maintained same as the master cylinder. Centering and leveling of the sample cylinder on the chuck of the rotational stage will only change the center axis of the sample cylinder, not the rotational stage center axis.

4.4. Examples

Simulations and an experiment are conducted to demonstrate the developed mathematical model.

4.4.1. Simulations

Three simulations, one for the cylindricity measurement, one for the calibration process, and the other for the error analysis, are conducted.

4.4.1.1. Cylindricity measurement

The simulation for the cylindricity measurement assumes that the true values of the position of the center axis of the rotational stage, the position of the focus line of the cylindrical lens, the focal length of the cylindrical lens, and the constant shift of the reference point, are known. The laser holographic interferometry measurements at different angular positions of a perfect cylinder are simulated excluding any measurement errors. These simulated measurement results are input to the developed algorithm and the cylindricity of the cylinder is calculated. By comparing the calculated cylindricity with the true cylindricity (= 0), the algorithm is evaluated.

The true values of the following parameters are assumed. The coordinate of point $\mathbf{O}_0$ which the center axis of the rotational stage goes through is $\mathbf{O}_0 = (0, 0, 0.5)$ mm. The direction $\mathbf{D}_0$ which the center axis of the rotational stage follows is $\mathbf{D}_0 = (0, 1, 0)$. The coordinate of point $\mathbf{O}_1$ which the center axis of the cylinder goes through at the angular position of 0º is $\mathbf{O}_1 = (0, 0, 1)$ mm. The direction $\mathbf{D}_1$ which the center axis of the cylinder follows at the angular position of 0º is $\mathbf{D}_1 = (0, 0.9988, 0.0499)$. The coordinate of point $\mathbf{O}_2$ which the center axis of the converging light goes through is $\mathbf{O}_2 = (0, 0, –1)$ mm. The direction $\mathbf{D}_2$ which the center axis of the converging light follows is $\mathbf{D}_2 = (0.0995, 0.9950, 0)$. The focal length R_0 of the cylindrical lens is 50 mm. The radius R of the perfect cylinder is $R = 12.5$ mm. The constant shift S of the reference point is assumed to be $S = 12$ mm. For each measurement, the angular and axial coverage of the cylinder surface are 90º and 15 mm, respectively. The covered region of the cylinder surface in each measurement is represented by a measurement matrix with the dimension of 128 x 128. Four rotations with an angular incremental step of 90º are simulated.

The 3D illustrations of the four simulated measurement matrices from the laser holographic interferometry system are shown in Fig. 4.3 with the sampling rate of every 8

points for the purpose of easy illustration. The angular positions of the four measurements in Figs. 4.3(a) to 4.3(d) are 0º, 90º, 180º, and 270º, respectively. The black dots correspond to elements in the measurement matrix. The lines connecting the dots indicate the rows, which correspond to the direction closely perpendicular to the cylinder axis, in the measurement matrix. Irregular shapes of the simulated measurements are observed and these shapes change as the angular position of the cylinder changes. This is because center axes of the cylinder, the rotational stage, and the cylindrical lens do not match in 3D space. Ideally, if these three center axes match, the measurement matrix will appear as the same flat plane at different angular positions.

These four simulated measurement matrices and the corresponding angular positions of the cylinder are input to the cylindricity measurement program, which has the true values of the $\mathbf{O}_0$, $\mathbf{D}_0$, $\mathbf{O}_2$, $\mathbf{D}_2$, R_0, and S. Using the mathematical model described in Sec. 4.2, the 3D surface profile of the cylinder is generated, as shown in Fig. 4.4. A mismatch is observed in the connecting regions between two adjacent sets of the converted 3D measurement data points. This is because that the center axis of the rotational stage and the focus line of the cylindrical lens do not match. However, this mismatch does not impact the estimated cylindricity because all the converted data points are still on the same cylinder surface. The estimated cylindricity using the evaluation algorithm in Sec. 4.2.3 is 1.24×10^{-14} mm. Compared with the true value (= 0 mm), the algorithm is validated.

4.4.1.2. Calibration

The same four simulated measurement matrices and the corresponding angular positions as in Sec. 4.4.1.1 are input to the calibration program. However, the program does not have the information of the true values for the parameters: $\mathbf{O}_0$, $\mathbf{D}_0$, $\mathbf{O}_2$, $\mathbf{D}_2$, R_0, and S. The iteration process, described in Sec. 4.3, is applied to estimate these values. In practice, these estimated values will be used as the true values for the cylindricity calculation.

After totally 18,042 iterations for 10 min in MATLAB 7.0 on a standard PC, the final estimated parameters are $\mathbf{O}_0 = (-2.9694\times10^{-5}, 0, -0.3718)$ mm, $\mathbf{D}_0 = (1.5568\times10^{-8},$

1, -3.4482×10^{-9}), $\mathbf{O}_2$ = (-3.1332×10^{-5}, 0, –1.8718) mm, $\mathbf{D}_2$ = (0.099504, 0.99504, -4.0115×10^{-8}), R_0 = 50.000 mm, and S = 12.001 mm, which delivers the cylindricity as 7.8741×10^{-7} mm. The estimated cylindricity converges to the true value (0 for a perfect cylinder) within the error smaller than 0.001 μm. Those estimated parameters also converge very closely to the true values except the positions of $\mathbf{O}_0$ and $\mathbf{O}_2$. However, the relative position between the estimated $\mathbf{O}_0$ and $\mathbf{O}_2$ is (1.7693×10^{-5}, 0, –1.5000) mm, which is very close to the true relative position, which is (0, 0, –1.5) mm, between $\mathbf{O}_0$ and $\mathbf{O}_2$. This is because wherever the center axis of the rotational stage and the focus line of the cylindrical lens are located, the generated cylinder surface profile will be the same if the relative position between the center axis of the rotational stage and the focus line of the cylindrical lens keeps the same. These results demonstrate the convergence and feasibility of developed mathematical model.

4.4.1.3. Error analysis

The cylindricity measurement error is analyzed by considering the parameter estimation errors in the cylindrical lens, the rotational stage, and the measurement system with the assumption that the cylindrical lens is ideal, i.e., there is no aberration to disable the cylindrical lens to focus at a straight line.

The parameter estimation errors in the cylindrical lens include the focal length error ΔR_0, the point position error $\Delta\mathbf{O}_2(\Delta x_2, \Delta y_2, \Delta z_2)$, the direction error $\Delta\mathbf{D}_2(\Delta a_2, \Delta b_2, \Delta c_2)$ in which only two parameters are independent, and the constant shift error ΔS. The rotational stage error is the angular position error $\Delta\theta$. The measurement system errors include the lateral position errors Δx_m and Δy_m, and the height measurement error Δd_o. The errors of these parameters are assumed to follow the normal distribution with a reasonable deviation. The true values of all the parameters are also assumed known.

The cylindricity measurement error is analyzed in two steps. First, the error of each parameter is applied separately with all the other parameters equal to true value to quantify the sensitivity of the cylindricity measurement error using the Eqs. (4.1)-(4.6). Due to the complexity of the equations, explicit expression of the sensitivity is not derived. The true value plus error is input directly to the cylindricity calculation program

to calculate the cylindricity error. Second, Monte Carlo simulation is conducted with the effects of all the parameters errors included simultaneously in the cylindricity measurement. The error of each parameter is assumed to follow the normal distribution.

The true values of these parameters are assumed to be the same as in Sec. 4.4.1.1. The errors of each parameter are assumed to follow the normal distribution with the expected value equal to 0. The 3σ of these parameters are: ΔR_0 = 0.010 mm, $\Delta\mathbf{O}_2$ is within a sphere of 0.010 mm radius centered at the true position $\mathbf{O}_2$, $\Delta\mathbf{D}_2$ is within 0.05º range from the true direction $\mathbf{D}_2$, ΔS = 0.010 mm, Δx_m = 0.15 mm, Δy_m = 0.15 mm, Δd_0 = 1 μm, and $\Delta\theta$ = 0.04º.

The effect of each parameter error on the final cylindricity measurement is shown in Table 4.1. The first set of the cylindricity error is due to the effect of the parameter estimation error of the cylindrical lens. With the error of each parameter (3σ) listed in Table 4.1, the corresponding cylindricity measurement errors before and after the registration adjustment are recorded. The registration adjustment can significantly reduce the cylindricity measurement error induced by the cylindrical lens parameter estimation errors, except the position estimation error $\Delta\mathbf{O}_2$. This is because position error $\Delta\mathbf{O}_2$ makes the converted 3D representation out of the cylindrical shape and this error cannot be rectified by adjusting the measurement data to match the reference cylinder of different measurements. The 0.05º $\Delta\mathbf{D}_2$ error makes one end of the focus line 0.079 mm away from the true position for a 45 mm long cylinder, which is used in the simulation. After converting the error to the same scale, it is observed that the cylindricity measurement error is most sensitive to position estimation error $\Delta\mathbf{O}_2$ of the point on the focus line. Only 0.010 mm $\Delta\mathbf{O}_2$ introduces 0.030 mm cylindricity measurement error.

The other two sets of Table 4.1 are the effects of the system measurement error and the rotational stage error. The 0.15 mm Δx_m and Δy_m are the lateral resolution of the laser holographic interferometry system. The 1 μm Δd_0 is the height measurement accuracy of the system. The 0.04º $\Delta\theta$ is the calibrated accuracy of the rotational stage used in this research. The registration adjustment does not affect any effect of the system measurement error or the rotational stage error because these two kinds of errors change the position of the measured data points symmetrically about the center axis. The lateral

position error of the system has an important effect on the cylindricity measurement. The height measurement error of the system is linearly mapped to the cylindricity measurement error. The effect of the angular positioning error of the rotational stage on the cylindricity measurement is trivial.

The Monte Carlo simulation is conducted to include all the error effects simultaneously and investigate the performance of the cylindricity measurement. The same parameter estimation errors listed in Table 4.1 are used and 1000 simulations are conducted. The histogram of the simulated cylindricity measurement error after the registration adjustment is shown in Fig. 4.5. The minimum cylindricity measurement error is 0.024 mm. The mean and standard deviation of the cylindricity measurement error are 0.097 mm and 0.054 mm, respectively.

4.4.2. Experiment

This experiment applies the Coherix Shapix 2000 laser holographic interferometry system with a cylindrical lens, the rotational stage, and a fine adjustment mechanism to measure a centerless ground steel cylinder. The system configurations, the experiment procedures, the measurement results, and the processing are elaborated.

4.4.2.1. System configurations

The system configuration of the cylindricity measurement experiment is shown in Fig. 4.6. All the components are inside the measurement cabinet of the laser holographic interferometry system. The rotational stage HAAS HA5C is fixed on the vibration isolated table. A centerless ground steel cylinder (25.4 mm in diameter) is used as a master cylinder to verify the developed mathematical model. The master cylinder is fixed in the chuck, which is attached to the rotational stage. There are 4 centering screws (only 2 visible in Fig. 4.6), positioned at 0º, 90º, 180º, and 270º around the circumference of the chuck to adjust the center position of the master cylinder. The cylindrical lens, which is bonded to the fine adjustment mechanism with 4 degrees of freedom, is

positioned above the master cylinder. A granite plate is positioned beside the master cylinder. This granite plate, used as a height datum, is fixed through the whole measurement process and measured with the laser going down directly to the surface.

4.4.2.2. Adjustments

Adjustment is conducted before the measurement. Three components, the master cylinder, the cylindrical lens, and the granite plate, are adjusted in sequence.

The master cylinder is centered after it is fixed in the chuck. This centering is conducted by adjusting the four centering screws on the chuck with a dial indicator in contact with the master cylinder surface. The runout of the master cylinder after centering is less than 25 μm.

The cylindrical lens is adjusted by the fine adjustment mechanism to have good modulations at 0º, 90º, 180º, and 270º positions. The mechanism has four degrees of freedom: translation in x direction, translation in z direction, rotation about x axis, and rotation about z axis.

The orientations of the granite plate are adjusted by the three adjustment screws underneath to have good surface reflectivity. This granite plate is fixed after the adjustment and used as a height datum. This will be elaborated in Sec. 4.4.2.4.

After the adjustment, measurement of the cylinder surface and the granite plate is conducted in one image capturing. Between two consecutive measurements, the rotational stage is rotated by inputting an angle value on the control panel with the resolution of 0.001º.

4.4.2.3. Measurement results

The surface area covered in one measurement is about 9º of the cylinder and about 42 mm axial length. Each measurement contains more than 20,000 points. Totally there are 58 measurements, which add up to more than 1 million points.

Figures 4.7 to 4.10 show four typical height measurement results obtained by Coherix Shapix 2000 system. The angular positions of these four measurements are

333.140º, 62.227º, 149.988º, and 244.377º, respectively, with about 90º spacing. Fig. 4.7(a) is a 2D grayscale illustration of the measurement matrix. The left rectangle corresponds to the master cylinder surface. The right rectangle is for the granite plate. Two lines, Line 1 from $-y$ to $+y$ and Line 2 from $-x$ to $+x$, are drawn across the grayscale map in Fig. 4.7(a). The height profiles along these two lines are illustrated in Figs. 4.7(b) and 4.7(c), respectively. These two lines are drawn at the same positions in Figs. 4.8(a), 4.9(a), and 4.10(a) as in Fig. 4.7(a). Compare the profiles at these four angular positions along Line 1 and Line 2, respectively, it is observed that at angular positions of 333.140º and 244.377º, the trend of the master cylinder surface leans upward from $-y$ to $+y$; whereas the trend at the angular positions of 62.227º and 149.988º is opposite. This indicates that the center axis of the rotational stage and the center axis of the cylinder do not match in the 3D space. The height positions of the granite plate change between the four angular positions. This is because the reference point, which has the height value equal to 0 in the measurement matrix, changes as the cylinder rotates. The trend of Line 2 at the angular positions of 333.140º and 62.227º leans downward from $-x$ to $+x$; whereas the trend at the angular positions of 149.988º and 244.377º is opposite.

4.4.2.4. Processing

The height measurement data of the master cylinder from the 58 measurements are first adjusted with reference to the height measurement data of the granite plate, which is fixed through the whole measurement process and used as common height datum. The reason of this adjustment is that the Coherix Shapix measurement is relative, i.e., all the height data points in one measurement are relative to a reference point, and this reference point changes as the master cylinder rotates. The measured height of the granite plate from all the measurements is compared with the first measurement. The difference of height is least square fitted by a plane and the trend of this plane will be subtracted from the corresponding height measurement data of the master cylinder.

The row and column coordinates of the element in the height matrix of the Coherix Shapix 2000 measurement are converted into the x and y coordinates. All the 58 adjusted and converted measurement data of the master cylinder together with the

corresponding angular positions are input to the program. Initial guess are generated to estimate $\mathbf{O}_0$, $\mathbf{D}_0$, $\mathbf{O}_2$, $\mathbf{D}_2$, R_0, and S. Then iterations are conducted to find the optimal values of these unknown parameters, which deliver the minimum cylindricity error of the master cylinder. To avoid the problem of iteration sensitivity to initial guess, multiple initial guess of the randomly selected unknown parameters are used.

The converged solution is reached after 4568 iterations for more than 33 hours. Figure 4.11 shows the generated 3D surface profile of the master cylinder surface with the final estimation of these parameters. The estimated values of all the unknown parameters are: $\mathbf{O}_0$ = (160.3313, 0, –12.4622) mm, $\mathbf{D}_0$ = (–0.1369, 0.9796, –0.1469), $\mathbf{O}_2$ = (162.1639, 0, –14.2365) mm, $\mathbf{D}_2$ = (–0.1467, 0.9783, –0.1466), R_0 = 251.12 mm, and S = 123.22 mm, which delivers the cylindricity error as 123 μm.

The master cylinder was measured by the contact-based Taylor Hobson TalyRond 265 system. The cylindricity of the same surface region was 8 μm with 2 mm spacing between two adjacent cross-sections of the cylinder. Compared with this contact-based measurement result, a 115 μm error in the laser holographic interferometry measurement exists. There are four possible reasons for this error. First, the possible runout error of the rotational stage may have a significant effect on the cylindricity evaluation. Second, the measurement data from the laser holographic interferometry system is not rectified and some significant errors in the lateral coordinates x and y may exist. Third, the iteration process to estimate the system configuration parameters may not find the globally optimal combination. Fourth, the cylindrical lens used in this research is off-the-shelf and some significant aberrations of the cylindrical lens may exist. A calibration process of the cylindrical lens shall be developed.

Different error sources are quantified to analyze their contributions to the 115 μm cylindricity measurement error. The maximum runout error of the rotational stage, which is used in this research, is the 10 μm [71]. This indicates that the center axis of the rotational stage should be within a virtual 10 μm radius cylinder centered at a stationary and perfect straight line. The maximum cylindricity measurement error introduced by the 10 μm runout of the rotational stage is 20 μm. The lateral coordinate measurement errors Δx_m (= 0.15 mm) and Δy_m (= 0.15 mm) of the laser holographic interferometry system

will have the cylindricity measurement errors equal to 15 μm and 29 μm, respectively, as shown in Table 4.1. The 1 μm height measurement accuracy of the laser holographic interferometry will generate the 2 μm cylindricity measurement error. The total error contribution of the laser holographic interferometry is 46 μm. The iteration process described in Sec. 4.3 can also have some system parameter estimation errors. Assume the system parameter estimation errors are ΔR_0 = 10 μm, ΔS = 10 μm, and $\Delta \mathbf{O}_2$ = 10 μm, the cylindricity measurement errors introduced by these errors are calculated using the Eqs. (4.1)-(4.6) as 0.8 μm, 0.4 μm, and 30 μm, respectively. The total error contribution of these assumed system parameter estimation errors is 31 μm. The aberration of the cylindrical lens also contributes to the cylindricity measurement error. Assume there is 5 μm error in focusing the light to the focus line of the cylindrical lens. This focusing error will generate another $\Delta \mathbf{O}_2$ up to 5 μm for all light directions and introduce up to 15 μm cylindricity measurement error. These four error contributions, 20 μm by the 10 μm runout of the rotational stage, 46 μm by the lateral and height measurement errors of the laser holographic interferometry system, 31 μm by the assumed system parameter estimation errors ΔR_0 = 10 μm, ΔS = 10 μm, and $\Delta \mathbf{O}_2$ = 10 μm, and 15 μm by the assumed 5 μm focusing error, add up to about 112 μm cylindricity measurement error. This quantitatively explains the error sources of the cylindricity measurement. More experiments shall be conducted to verify the assumed system parameter estimation errors and evaluate the aberrations of the cylindrical lens.

4.5. Concluding remarks

A mathematical method was developed to utilize the laser holographic interferometry with customized optical and mechanical configurations for flexible and full surface measurement of cylinders with variable diameters. A cylindrical lens was used to customize the optical system and enable the laser holographic interferometry for the inspection of cylinders. A rotational stage was applied to rotate the cylinder and the whole circumference of the cylinder can be measured. The developed mathematical model converted the laser holographic interferometry measurements into the 3D

representation of the cylinder surface from which the cylindricity can be calculated. The simulation demonstrates that the developed method can estimate the system configuration parameters with good accuracy. The effect of the estimation error of system configuration parameters and the measurement error on the cylindricity measurement was analyzed. The experiment with the master cylinder was conducted and the cylindricity was estimated with an error of 115 μm, which was mainly due to the four possible error sources.

Two possible future researches can follow. First, this method assumes no aberration in the cylindrical lens. A calibration procedure of the cylindrical lens should be developed to accommodate the aberrations of the optical system. Second, a more robust and time-efficient calibration process should be developed to improve the performance of the estimation of the unknown parameters.

Table 4.1. The cylindricity measurement error due to the parameter estimation errors.

Parameter estimation error (3σ)	Maximum cylindricity error (mm)	
	Before registration adjustment	After registration adjustment
ΔR_0 = 0.010 mm	0.002	0.001
$\Delta \mathbf{O}_2$ = 0.010 mm	0.029	0.030
$\Delta \mathbf{D}_2$ = 0.05º	0.043	0.010
ΔS = 0.010 mm	0.0008	0.0004
Δx_m = 0.15 mm	0.015	0.015
Δy_m = 0.15 mm	0.028	0.029
Δd_0 = 1 μm	0.002	0.002
$\Delta \theta$ = 0.04º	0.000	0.000

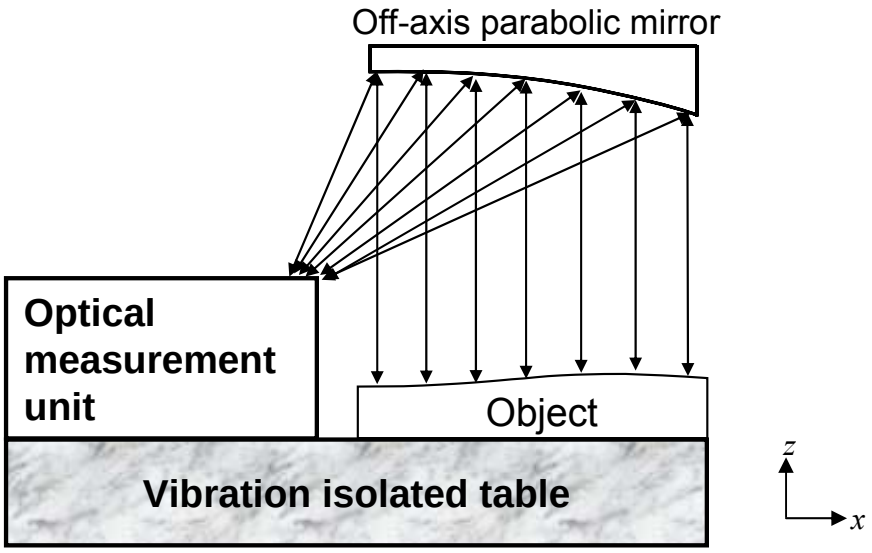

(a)

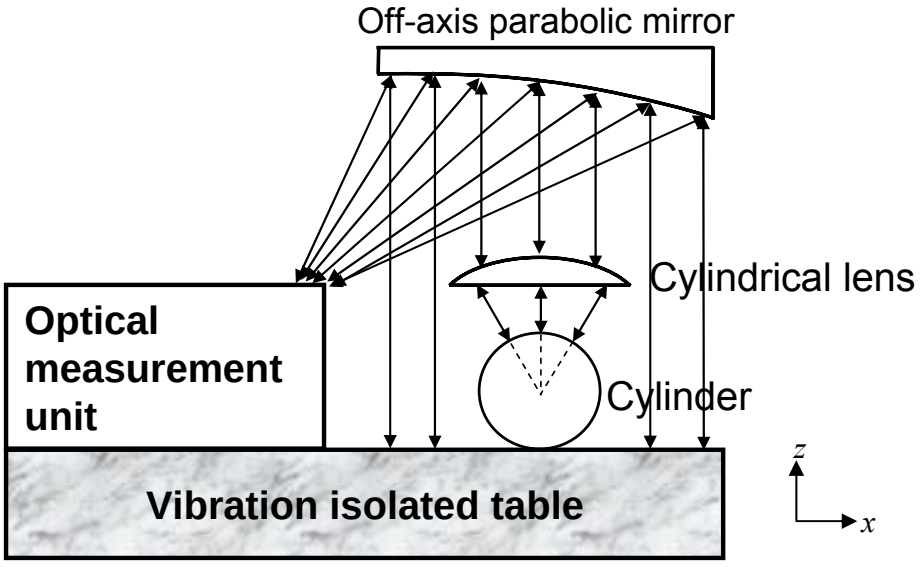

(b)

Fig. 4.1. Conceptual system design of the laser holographic interferometry system: (a) flat object measurement and (b) cylindricity measurement.

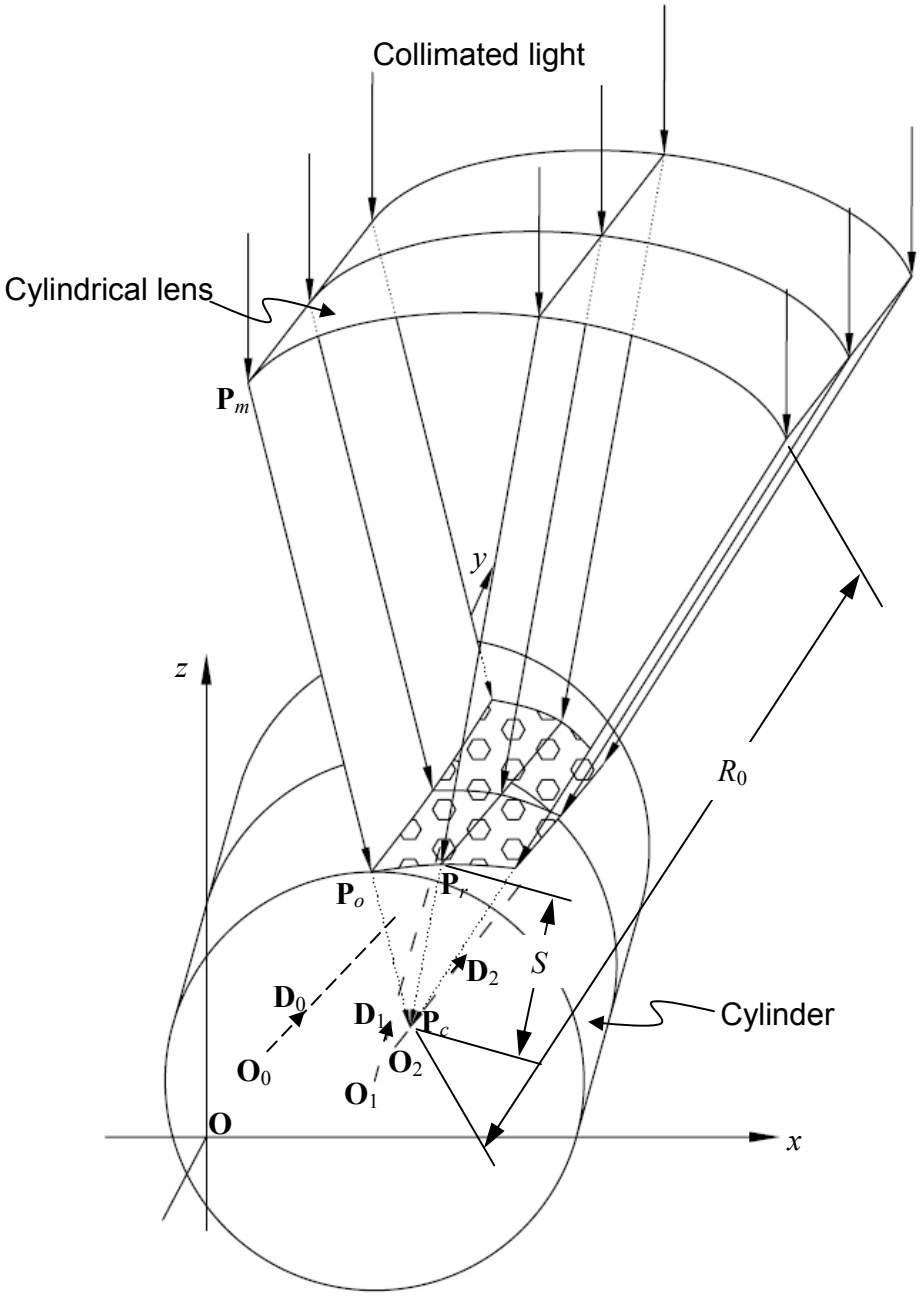

Fig. 4.2. 3D illustration of the geometric relations in the mathematical model for the cylindricity measurement with the laser holographic interferometry system.

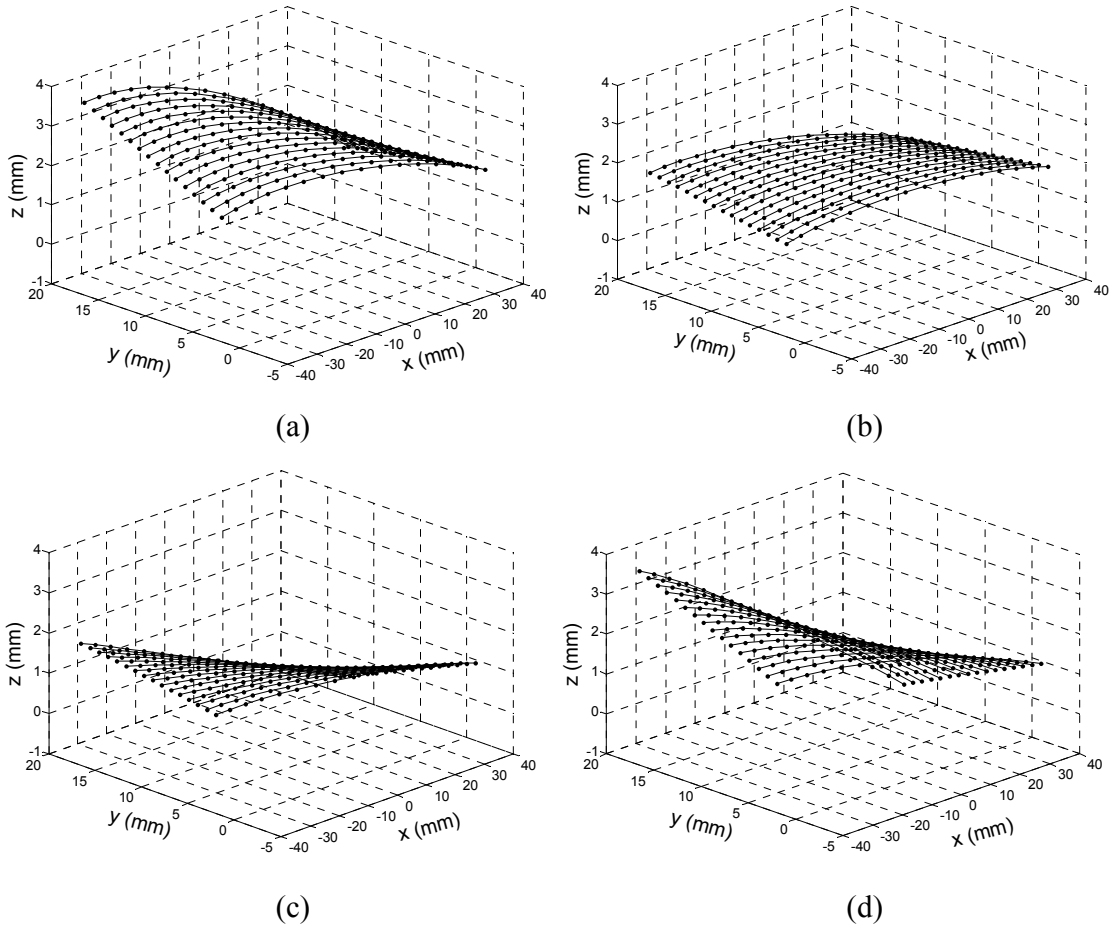

Fig. 4.3. 3D illustration of four simulated laser holographic interferometry measurements of the cylinder with O_0 = (0, 0, 0.5) mm, D_0 = (0, 1, 0), O_2 = (0, 0, –1) mm, D_2 = (0.0995, 0.9950, 0), R = 12.5 mm, and S = 12 mm (O_1 = (0, 0, 1) mm and D_1 = (0, 0.9988, 0.0499) at the 0º angular position of the cylinder): (a) at 0º angular position, (b) at 90º angular position, (c) at the angular position of 180º, and (d) at the angular position of 270º of the cylinder.

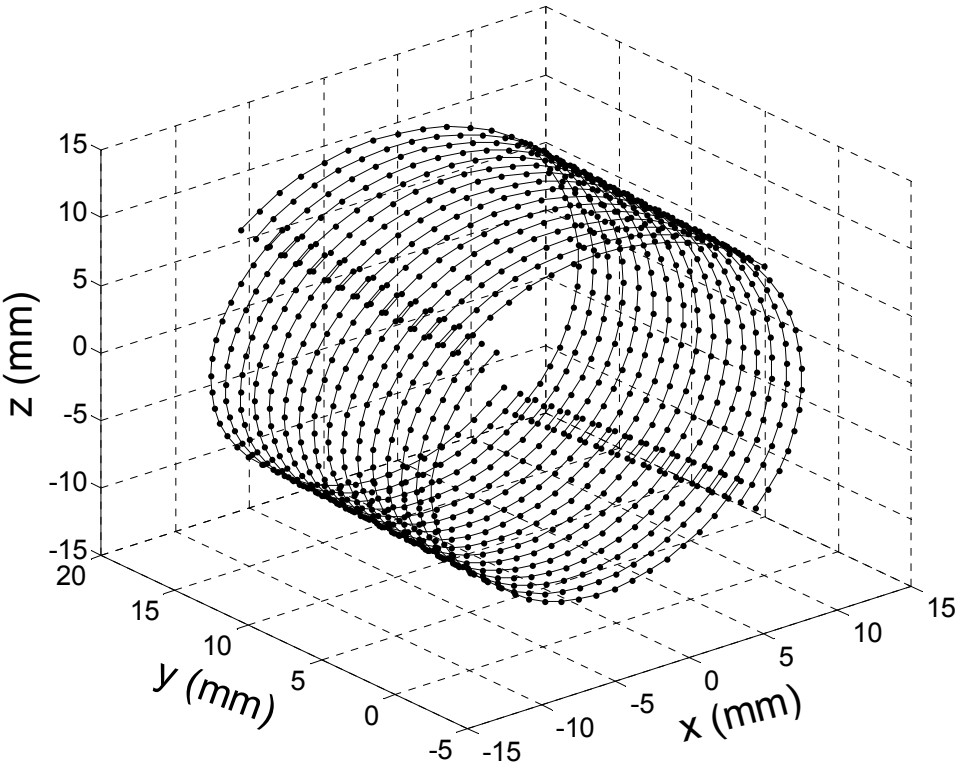

Fig. 4.4. Generated cylinder surface profile from the simulated data (cylindricity = 7.9×10^{-7} mm).

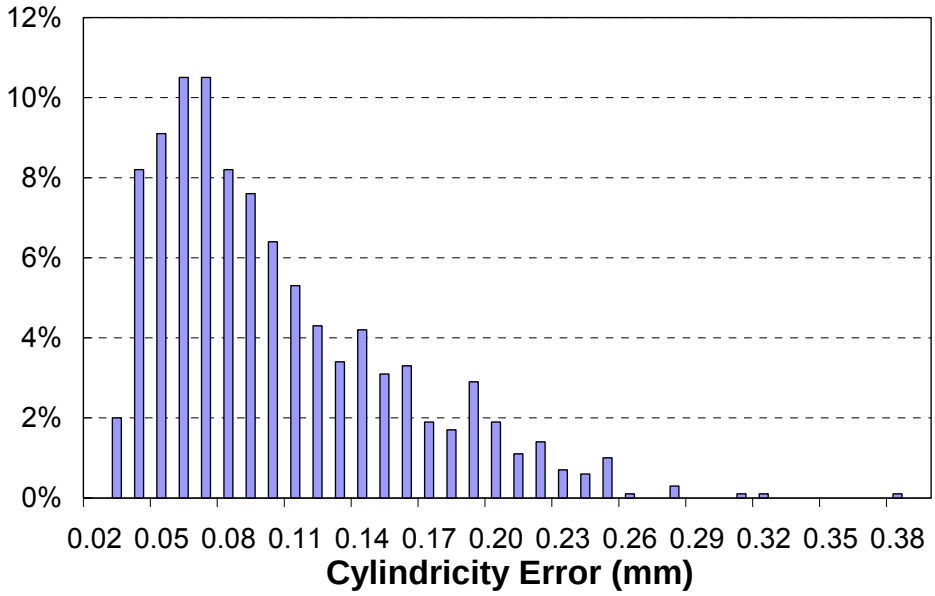

Fig. 4.5. The cylindricity measurement error distribution simulated by the Monte Carlo method.

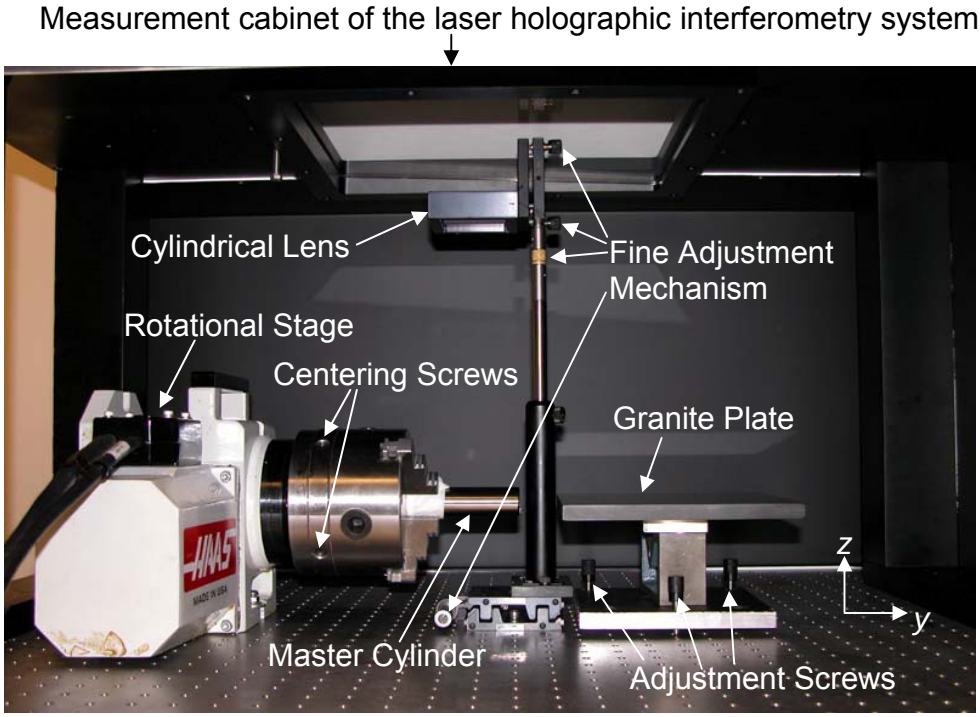

Fig. 4.6. System configurations of the cylindricity measurement.

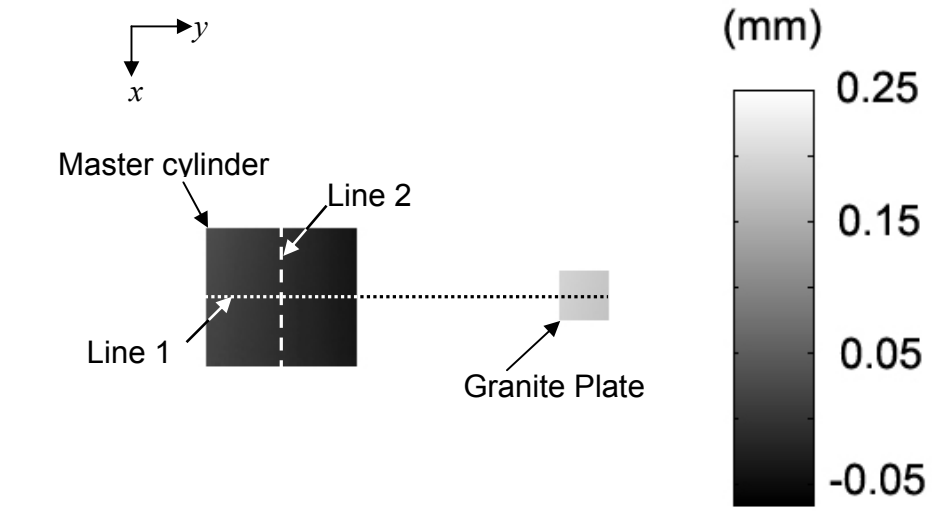

(a)

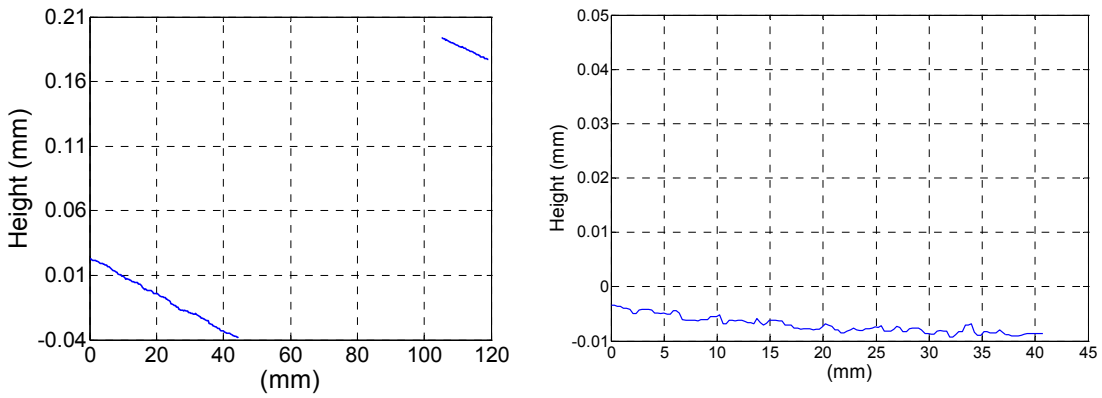

(b) (c)

Fig. 4.7. Height measurement of the master cylinder at the angular position of 333.140º: (a) 2D color map, (b) height profile along Line1 from left to right in (a), and (c) height profile along Line 2 from top to bottom in (a).

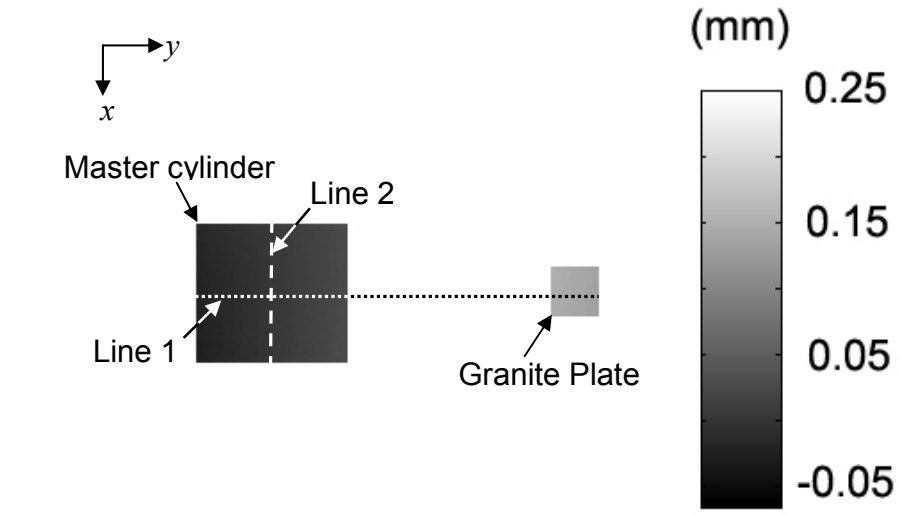

(a)

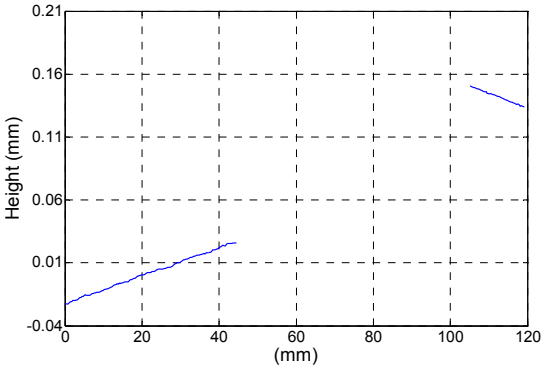

(b)

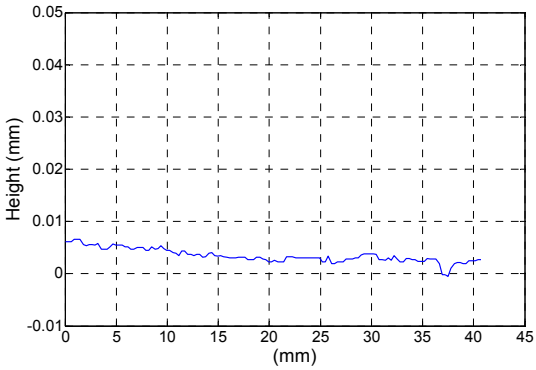

(c)

Fig. 4.8. Height measurement of the master cylinder at the angular position of 62.227º: (a) 2D color map, (b) height profile along the Line 1 from left to right in (a), and (c) height profile along the Line 2 from top to bottom in (a).

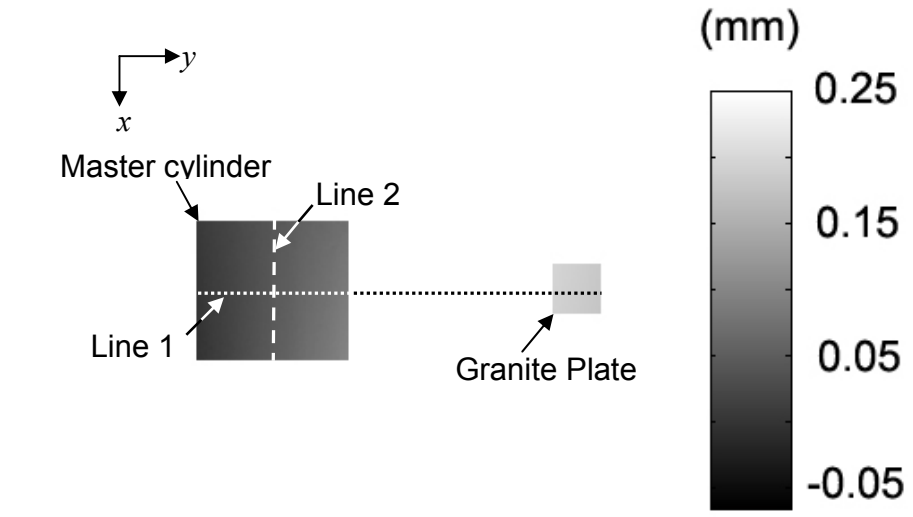

(a)

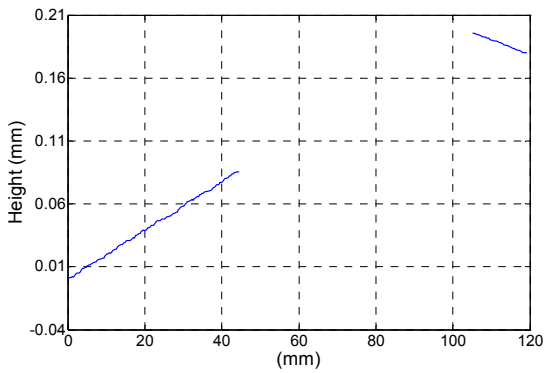

(b)

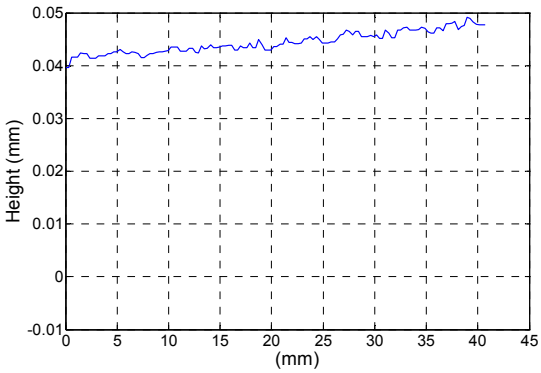

(c)

Fig. 4.9. Height measurement of the master cylinder at the angular position of 149.988º: (a) 2D color map, (b) height profile along the Line 1 from left to right in (a), and (c) height profile along the Line 2 from top to bottom in (a).

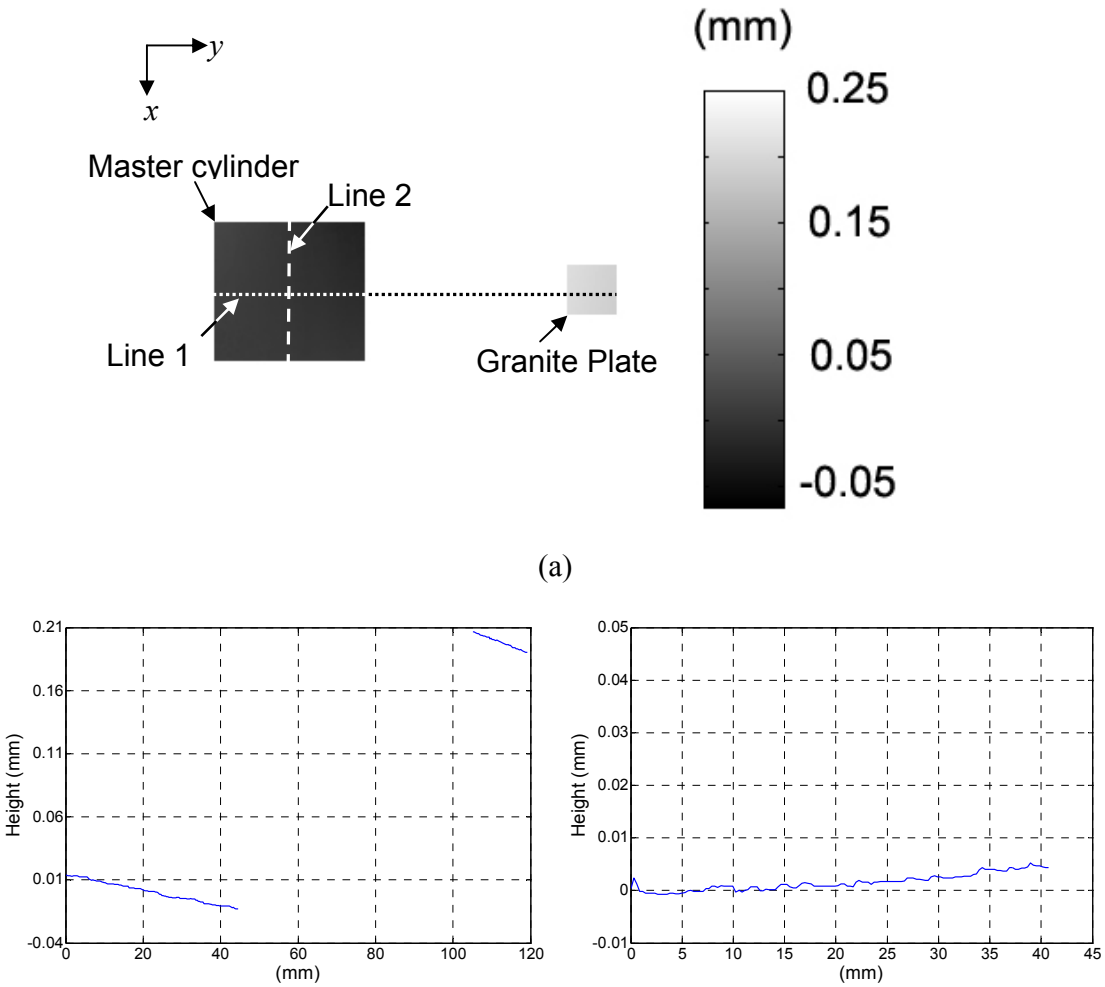

Fig. 4.10. Height measurement of the master cylinder at the angular position of 244.377º: (a) 2D color map, (b) height profile along the Line 1 from left to right in (a), and (c) height profile along the Line 2 from top to bottom in (a).

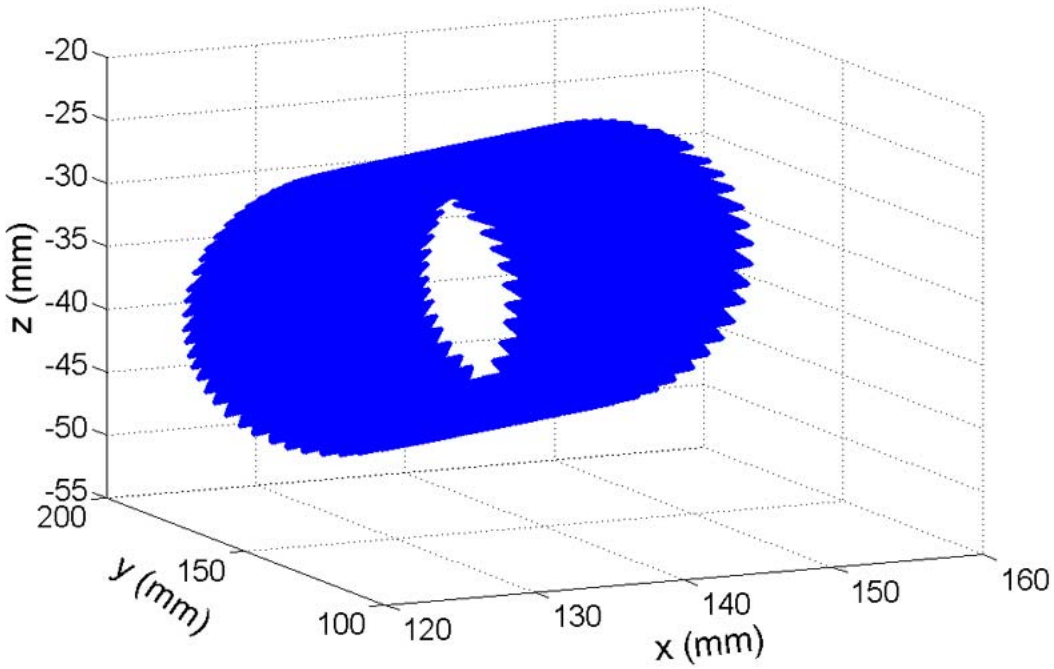

Fig. 4.11. 3D illustration of the final estimation of the master cylinder.

Chapter 5

Conclusions and Future Work

5.1. Conclusions

This research developed three new methods to improve the laser holographic interferometry for the 3D precision and full surface measurement of manufactured components. The flatness evaluation errors for the high definition measurement system were investigated.

A hologram registration method without using targets was developed in Chapter 2 for the laser holographic interferometry measurement of objects larger than the field of view (FOV). The cross-correlation analysis was used to identify the translation and overlapped regions, which determine the tilt and shift correction for hologram registration. The proposed method was validated using two examples with different approaches. The first example, a wheel hub smaller than the FOV, demonstrated only 0.1 μm discrepancy of the surface flatness between the registered and standard measurements. The second example, an engine head combustion deck surface, was larger than the FOV. The registered surface measurements were compared to that of CMM with only 2.5% discrepancy of the peak-to-valley flatness. This hologram registration method enables the μm-level precision measurement of large objects.

A phase unwrapping method was developed in Chapter 3 to mathematically increase the height measurement range of the laser holographic interferometry while maintaining the same level of accuracy and resolution. Three approaches, including the masking and recovery, dynamic segmentation, and phase adjustment for pixels in thin boundary regions, were developed to effectively avoid the divergence problem of

boundary pixels. This method successfully solves the phase unwrapping problem of the laterally discontinuous surfaces and is validated using an example of the automatic transmission valve body.

A mathematical method was developed in Chapter 4 to utilize the laser holographic interferometry with customized optical and mechanical configurations for flexible and full surface measurement of cylinders with variable diameters. The developed mathematical model converts the laser holographic interferometry measurements into the 3D representation of the cylinder surface from which cylindricity was calculated. The simulation demonstrated that the developed method can estimate the system configuration parameters with good accuracy. The effect of the estimation error of system configuration parameters and the measurement error on the cylindricity measurement was analyzed. The experiment was conducted to measure the master cylinder with negligible cylindricity errors and the feasibility of the developed method was verified.

A preliminary study was conducted in Appendix C to analyze the flatness evaluation errors for high definition measurements. Two commonly used methods, least square and minimum zone, were analyzed in the estimation error of the reference plane for flatness evaluation. The widely-used peak-to-valley flatness definition and two proposed flatness definitions, $6\sigma_f$ and modified peak-to-valley, were assessed. Five surface profiles with the random measurement errors were generated to simulate the flatness evaluation process. The results showed that the least square method with the modified peak-to-valley definition has the good potential among the analyzed methods to effectively evaluate the flatness with good noise robustness for the high definition measurement system.

5.2. Future work

This research will continue in two areas. First is to further improve the performance of the cylindricity measurement with the laser holographic interferometry system. Third is to develop a more comprehensive method to quantitatively evaluate

different geometrical form measurement errors for the high definition measurement system.

5.2.1. Performance improvement of cylindricity measurement

The cylindricity measurement methods developed in Chapter 4 is verified in simulations to be capable of estimating the system configuration parameters and evaluating the cylindricity with good accuracy. The conducted experiment demonstrates the feasibility of this method in practice but the cylindricity evaluation accuracy needs improvement.

To further improve the performance of the cylindricity measurement, two research investigations will follow.

- *Calibration of cylindrical lens*: The cylindrical lens used in Chapter 4 is off-the-shelf and no calibration was conducted. An aspherical cylindrical lens with minimum aberrations should be utilized to advance the performance of the method. An effective calibration method of the cylindrical lens, using a master cylinder with negligible cylindricity errors and precisely rectified grooves, as shown in Fig. 5.1, should be developed. The rectified grooves will appear in a possibly distorted way in the generated 3D representation of the cylinder due to the aberrations of the cylindrical lens. By comparing the measured profile with the rectified profile of the grooves, the cylindrical lens can be calibrated.
- *Improvement of the iteration process*. Iteration is conducted in the mathematical method described in Chapter 4 to estimate the unknown system configuration parameters. The converged results are sensitive to the initial guess though multiple combinations of randomly selected initial guess are applied because the optimization search is gradient-based. More robust and efficient optimization methods will be explored to reach a more reliable estimation of these system configuration parameters.

5.2.2. Error analysis of geometrical form evaluation for high definition measurements

The huge number (more than 1 million) of data points by the high definition measurement system imposes a great challenge on how to evaluate the geometrical form variation because the huge number of data points makes the small probability event of large measurement error happen frequently. The preliminary analysis of the flatness evaluation error for high definition measurements was conducted in Appendix C. The reference plane estimated by least square method for flatness evaluation was demonstrated more robust to measurement errors than the minimum zone method. And the least square method with the modified peak-to-valley flatness definition has the potential among the analyzed methods to effectively evaluate the flatness with good noise robustness for the high definition measurement system. However, a more comprehensive theoretical analysis to quantitatively evaluate the geometrical form variations for the high definition measurement system should be conducted.

- *Flatness evaluation analysis*: The flatness is determined in two steps. First, a reference plane, from which the deviations of all the measured points are referred, is identified. Second, some parameter, such as peak-to-valley deviations of all the measured points, will be calculated as the flatness. In this research, a more comprehensive mathematical method will be developed to quantitatively analyze error flows starting from each measured points to the final evaluated flatness result for the high definition measurement system. Some more robust and efficient flatness evaluation methods can be developed.
- *Cylindricity and other geometric form analysis*: The research work in the flatness evaluation analysis for high definition measurements will be extended to other more complicated geometric forms, such as cylinder and sphere.

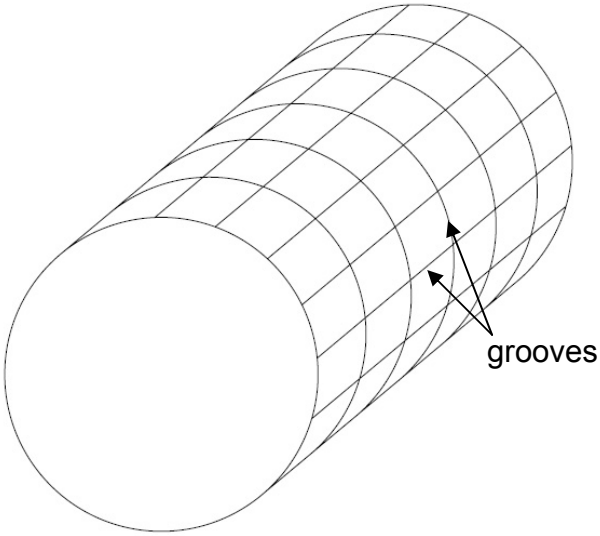

Fig. 5.1. Master cylinder with negligible cylindricity errors and precisely rectified grooves.

Appendices

Appendix A

Comparison Matrix of Six 3D Measurement Systems

The specifications of six different 3D measurement systems are compared. The comparison matrix is developed as following with the help of Robert Waite and Bill Haukkala from DaimlerChrysler and Dr. Lianxiang Yang from Oakland University.

Reconfigurable Precision Measurement Comparative Matrix	CMM (Zeiss UPMC 850)	Stereovision (CogniTens)	Laser Holography (Coherx)	RIM (UM)	Stereovision (Oakland Univ.)	3D-Digitization for Direct Measurement of Surface Slope (Oakland Univ)
Measurement Area (target size 400 × 250 × 25 mm)	850 × 1150 × 600 mm	100×70×45 mm 140×180×60 mm 190×260×150 mm 290×380×200 mm (stitching accuracy needs investigation)	300×300×25 mm	5 lines, 3 on one side, 2 on the other	100×100×20 mm (stitching accuracy needs investigation)	Almost unlimited (stitching accuracy needs investigation)
Measurement Time	Part dependent	Dependent on # of shots, image acquisition < 1msec./shot	~ 150 sec.	Not given	Dependent on # of shots (< 1 sec. for each shot) For the DCX engine head, 10 shots needed, DA < 10 sec./shot, total 2 min.	Dependent on # of shots (image acquistion < 1msec./shot) DA < 5 sec./shot
Lateral Resolution	0.1 μm in scanning range of ±0.2 mm	Not given (to be studied)	12 μm	2 μm (high definition)	10 μm	Not given (to be studeid)
Depth Resolution		Better than 100 μm for 6 σ (to be studied)	20 nm single λ	< 0.1μm (high definition)	10 μm	Better than 20 μm
Depth Accuracy	Global: ≤ 3 μm	? (to be studed)	20 nm	5 μm	? (to be studied)	? (to be studied)
Operating temperature	20°C ± 1°C	10 - 35 °C	15 - 30 °C	18 - 35 °C	10 - 35 °C	10 - 35 °C
Thermal gradient	0.5°C/h, 0.5 °C/m	Not defined	0.5 °C/15 min.	Not defined	Not defined	Not defined
Air humidity	40% - 60%	Not defined	5-95% relative, noncondensing	Not defined	Not defined	Not defined
User Skill Requirements	High	Medium (?)	Medium (?)	High	Medium	High
Ability to patch multiple scans	Not applicable	Yes	No	Not applicable	Yes	Yes
Automatic analysis	Yes	Yes	Yes		Yes	Yes
Repeatability		To be studied in this research	R&R 8.25%	?	To be studied in this research	To be studied in this research

Appendix B

Laser Holographic Interferometry and Performance Evaluation

B.1. Introduction

The holographic interferometry technology was initiated by Leith and Upatnieks [72-74] and invented by Stetson and Powell in 1960s [75].

The laser holographic interferometry includes the following important features:

- *High accuracy*: For a typical laser holographic interferometer, the height measurement accuracy of machined metal surfaces is 0.30 μm for the 0.3 mm height measurement range.
- *No shadowing or occlusion*: Shadowing occurs when the object cannot be illuminated but is visible to the sensor. Occlusion occurs when the object is illuminated but invisible the sensor. Either shadowing or occlusion does not exist in the laser holographic interferometry because the object is illuminated and viewed from the same direction.
- *No moving parts*: The instrument generates a 3D image of the entire FOV without scanning. The process is accomplished by flood illuminating the object and collecting the light with a 2D CCD camera. With all parts fixed, the instrument has high reliability and repeatability.

In this appendix, the principles of the laser holographic interferometry are described in Sec. B.2. The configurations and specifications of a state-of-the-art laser

holographic interferometer are presented in Sec. B.3. The performance is evaluated in Sec. B.4.

B.2. Principles of laser holographic interferometry

The 3D profiling of the laser holographic interferometry is based on the coherence property of light wave. The mathematical descriptions of light waves and their interference are introduced as following [76].

B.2.1. Mathematical expression of light wave

Light is an electromagnetic wave. For a plane light wave u, the electromagnetic field at an arbitrary point (x, y, z) is generally described as,

$$u(x,y,z,t) = U\cos[\varphi - 2\pi\upsilon t] \tag{B.1}$$

where

u represents the field in an electromagnetic wave,

U is the wave amplitude,

φ is the phase which is a function of x, y, and z,

υ is the frequency of the light wave, and

t is the time.

Figure B.1 shows the field distribution of the plane wave in 3D space at a time spot. At each plane perpendicular to the wave propagation direction, marked by $\boldsymbol{k}$ in Fig. B.1, the phases φ are constant at a time spot.

The observable quantity in the image recording media is the light intensity I, which is defined as the squared amplitude of the light wave, i.e., $I = U^2$.

B.2.2. Interference

Interference occurs when two plane waves u_1 $(= U_1 \cos(\varphi_1 - 2\pi\upsilon t))$ and u_2 $(= U_2 \cos(\varphi_2 - 2\pi\upsilon t))$ with the same frequency overlap. The interfered wave is $u = u_1 + u_2$. The light intensity in the CCD camera of the interfered wave is expressed as,

$$I = |u|^2 = |u_1 + u_2|^2 = U_1^2 + U_2^2 + 2U_1U_2\cos(\varphi_1 - \varphi_2) = I_1 + I_2 + 2\sqrt{I_1 I_2}\cos\Delta\varphi \quad \text{(B.2)}$$

where $\Delta\varphi = \varphi_1 - \varphi_2$ as the phase difference between the two waves.

No light source can emit light of a single frequency practically and Eq. (B.2) should be modified as

$$I = I_1 + I_2 + 2\sqrt{I_1 I_2}\gamma\cos\Delta\varphi \quad \text{(B.3)}$$

where γ is a complex degree of coherence term as a measure of the ability of the two wave fields to interfere.

B.2.3. Height measurement in laser holographic interferometry

The height of the measurement object is extracted by the phase-shifting and multi-wavelength tuning techniques.

The setup of the laser holographic measurement system is shown in Fig. B.2(a). The optical measurement unit generates the laser beam for measurement and acquires the hologram for computation. The optical measurement unit and object are both placed on a vibration isolated table to ensure the mechanical stability. An off-axis parabolic mirror is

located on the top of the machine to collimate the carrier beam u_c from the optical measurement unit to the object. The laser beam reflected from the object carries the surface height information and reflects by the parabolic mirror back to the optical measurement unit for processing.

The setup of the Twyman-Green interferometer [76] inside the optical measurement unit is shown in Fig. B.2(b). The laser beam from a tunable laser source is split by the beam splitter into two coherent laser beams: the reference beam u_r and carrier beam u_c. The reference beam u_r is a plane wave, i.e., phase φ_r is a constant across any plane perpendicular to the wave propagation direction. The reference beam u_r is reflected by a reference mirror, which is moved by a piezoelectric motor to apply the phase-shifting for measurement. The carrier beam u_c, re-directed by a mirror, is enlarged by a beam expander and directed to the parabolic mirror and object. The carrier beam u_c reflected from the object surface has the phase φ_c modulated by the height of the object. The Fourier transform method [76,77] is applied to analyze the hologram to extract the 3D surface profile of the object.

In this research, the carrier beam after collimation by the parabolic mirror is 300 mm x 300 mm in size, which is the FOV of the measurement system.

Two techniques, phase-shifting and multi-wavelength tuning, are applied to measure the height of an object surface.

B.2.3.1. Phase-shifting

The phase-shifting is applied to convert the intensity of each pixel in the CCD camera into the height of the corresponding point on the object surface. The light intensity I generated by the two interfering beams u_r and u_c is [76]:

$$I = I_r + I_c + 2\sqrt{I_r I_c}\,\gamma \cos\Delta\varphi \tag{B.4}$$

where $\Delta\varphi = \varphi_r - \varphi_c$ is the phase difference between the reference beam and the carrier beam.

The phase difference $\Delta\varphi$ ranges from $-\pi$ to π and can be linearly mapped to the height measurement ranging from −1/4 wavelength to 1/4 wavelength. To solve $\Delta\varphi$, the phase-shifting technique [78] is applied by moving the piezoelectric stage (shown in Fig. B.2(b)) with small, incremental steps. Moving the piezoelectric stage introduces a phase shift α and Eq. (B.4) can be rearranged as:

$$I = m + n\cos(\Delta\varphi + \alpha) \tag{B.5}$$

where

$m = I_r + I_c$,

$n = 2\sqrt{I_r I_c}\gamma$, and

α is the given phase shift.

When the phase of the reference beam is shifted by three given values α_1, α_2, and α_3, three light intensities $I_k = m + n\cos(\Delta\varphi + \alpha_k)$ (k = 1, 2, and 3) can be measured. The phase difference $\Delta\varphi$, which corresponds to height, on each pixel is [76]:

$$\Delta\varphi = \tan^{-1}\frac{(I_2 - I_3)\cos\alpha_1 - (I_1 - I_3)\cos\alpha_2 + (I_1 - I_2)\cos\alpha_3}{(I_2 - I_3)\sin\alpha_1 - (I_1 - I_3)\sin\alpha_2 + (I_1 - I_2)\sin\alpha_3} \tag{B.6}$$

In practice, more than three phase shifts, which introduce a set of over-determined equations, are applied to obtain a more numerically stable solution. The least square

method [76] has been derived to solve $\Delta\varphi$ of a set of over-determined equations. In this research, four or five 100 nm incremental movements of the piezoelectric stage are utilized to generate the phase shift.

B.2.3.2. Multi-wavelength tuning

To increase the range of height measurement, the multi-wavelength laser source, so called tunable laser, is applied. If a single wavelength laser source is used, the overall height range of all the pixels in the CCD camera must be smaller than ½ of the laser wavelength to avoid the ambiguity in the phase domain. This limits the range of height measurements. The use of multi-wavelength tuning can overcome this obstacle.

The multi-wavelength laser can be generated using a laser-cavity design [79]. The laser beam in the cavity strikes a diffraction grating at near grazing incidence, i.e., an incidence angle near 90°. The laser diffracts off the grating at different diffraction angles with different wavelengths. Each diffraction angle corresponds to a specific wavelength. In this study, a tunable diode laser, Velocity made by New Focus, can generate infrared wavelengths ranging from 830.80 nm to 850.60 nm. During measurement, the laser is tuned to 16 wavelengths with a constant step change of wavelength ranging from 0.02 nm to 1.00 nm.

In holographic interferometry, the concept of reference point is applied to improve the measurement accuracy and reduce the adverse effect caused by mechanical vibration from the surrounding environment. A reference point is arbitrarily selected in the measurement region. The phase of the reference point is designated as 0 by shifting the phase of all measurement points by a constant value. The height h and phase difference $\Delta\varphi$ of all other points are calculated relative to the reference point.

The height h is extracted by tuning the wavelength of the laser source and calculating the change of the phase difference $\Delta\varphi$ for each point [80]. If the wavelength λ_1 is used, the phase difference is $\Delta\varphi_1$, then $\Delta\varphi_1 = 4\pi h/\lambda_1$. If the wavelength is changed to λ_2, the phase difference is $\Delta\varphi_2 = 4\pi h/\lambda_2$. The height h can be solved by combining the two relations as below:

$$h = \frac{(\Delta\varphi_1 - \Delta\varphi_2)\lambda_1\lambda_2}{4\pi(\lambda_2 - \lambda_1)} \tag{B.7}$$

Eq. (B.7) shows that the height measurement range depends on the wavelength tuning step ($\lambda_2 - \lambda_1$). A smaller wavelength tuning step generates a larger height measurement range. If the tuning step ($\lambda_2 - \lambda_1$) is 0.02 nm, the wavelength is 830 nm, and the change of phase difference $(\Delta\varphi_1 - \Delta\varphi_2)$ is 2π, then the height measurement range is 17 mm. If the tuning step ($\lambda_2 - \lambda_1$) is increased to 1.00 nm, the height measurement range is reduced to 0.34 mm. The tradeoff of the increase in height measurement range is the decrease of resolution and accuracy.

In practical holographic measurement, more than two wavelengths are used to achieve a more robust solution. In this study, 16 wavelengths, marked as λ_1 to λ_{16} were applied. During the time interval, 4 or more phase shifts are conducted to calculate $\Delta\varphi$ for each wavelength. The change of wavelength occurs at a constant rate with period Δt and a constant tuning step $\Delta\lambda$ ($\Delta\lambda = \lambda_2 - \lambda_1 = \lambda_3 - \lambda_2 = ... = \lambda_{16} - \lambda_{15}$). At each wavelength, only the calculated phase difference $\Delta\varphi$ was selected as the angle of a complex number with unit magnitude. As the wavelength changes, the complex number rotates around the origin of the complex plane at the frequency f_s [81]. The Fourier transform analysis of the 16 complex values at 16 wavelengths generates a peak at f_s in the frequency domain. The height h can be expressed as [81]:

$$h = f_s\lambda_1^2 / \beta \tag{B.8}$$

where β is a constant which determines the wavelength tuning speed, i.e., $\Delta\lambda$ ($=\beta\Delta t$). The wavelength λ_1 and the constant β are known parameters. The height h on each point can be solved using Eq. (B.8) with the identified f_s.

The 3D surface profile is extracted from the measured hologram using the method described above. The height measurement calibration and the median filtering [82] are applied to reduce the noise.

B.3. Configurations of the laser holographic interferometer

The optical configurations of the laser holographic interferometer system under this research are shown in Fig. B.3. All the optical components are fixed. The laser comes out from the laser source, goes through a set of lenses, and reaches the beamsplitter which is inside of the black box in front of the CCD camera. A certain percent amount of the beam is transmitted as reference beam and reaches the mirror controlled by the piezoelectric translator in the reference arm. The other amount of the beam is reflected as carrier beam and goes through the neutral density (ND) filter. A series of ND filter are available for different surface reflectance. The flipper is designed to further reduce noise of measurement. The carrier beam then travels up to the parabolic mirror, which is positioned on the top of the machine.

An example measurement of an automatic transmission valve body is shown in Fig. B.4. The part is located on the tip-tilt support, which is used to level measurement surfaces. The complicated surface region of the valve body can be selected by the masking tool in the software.

The laser source is the Velocity tunable diode laser, provided by New Focus Co. The tunable wavelength range is from 831.00 to 853.00 nm. The minimum wavelength tuning step is 0.02 nm [83]. The maximum tuning speed is 8 nm/s [83]. The CCD camera is Dalstar DS-12-01M30, with 1024 x 1024 pixel resolution. The data sampling rate is 40 MHz, 30 frames per second with 12 bit digitization [84].

The basic claimed specifications of a typical laser holographic interferometer, Coherix Shapix 1000, are as following [85,86]. The FOV is 300 mm x 300 mm. The largest depth-of-field is 17 mm. For single wavelength measurement, the accuracy is 0.050 μm and the repeatability is 0.020 μm. For multi-wavelength measurement, the

accuracy is 0.50 μm and the repeatability is 0.20 μm. The claimed accuracy and the gage R&R will be evaluated in Sec. B.4.

B.4. Performance evaluation

Two kinds of parts, an artifact Step Gage, as shown in Fig. B.5, and five automatic transmission valve bodies from the production line, one of them shown in Fig. B.8, are used to evaluate the accuracy and the gage repeatability and reproducibility (R&R) of the laser holographic interferometer.

B.4.1. Accuracy evaluation

B.4.1.1. Artifact

The 48 mm x 48 mm Step Gage, made of stainless steel, has four ground surfaces denoted as A, B, C, and D, as shown in Figs. B.5(a) and B.5(b). The ground surfaces, each of 12 mm x 48 mm, are specular with about 0.2 μm R_a roughness. Three Step Heights, designated as I, II, and III in Fig. B.5(b), are used to evaluate height measurement accuracy of the laser holographic interferometer. The nominal value of Step Heights I, II, and III are 5, 15, and 35 μm, respectively. The target values of step heights are measured using the Taylor Hobson Form Talysurf profilometer. Ten measurement traces, all parallel to each other and perpendicular to the line between two adjacent step surfaces, are used to measure the Step Heights I, II, and III. An example of the profilometer measurement trace on the surface is shown in Fig.B.6. The algorithm presented in Sec. B.4.1.3 is used to calculate the step height. The average of the five measurements is used as the target value. As shown in Table B.1, target values for Step Heights I, II, and III are equal to 3.9, 13.6, and 32.1 μm, respectively.

B.4.1.2. Measurement procedures

The Step Gage is positioned in the middle of the field of view of the system. Three measurement groups, each of 11 measurements without moving the part, are

conducted. No powder spray is applied on the surface for each measurement. Between each group, the part is repositioned in the field of view.

B.4.1.3. Step height calculation

The least squares method is used to find the step height between two segments of data points. Three Step Heights I, II, and III, as shown in Fig. B.5(b), are referenced from the datum surface A. The points representing surface *J* are denoted as the vector $\boldsymbol{P}_{Ji}$, where *J* = A, B, C, and D, *i* = 1, 2, …, n_J, and n_J is the number of points on surface *J*. The middle point of surface *J*, denoted as $\boldsymbol{P}_{JM}$, is calculated by:

$$\boldsymbol{P}_{JM} = \frac{\sum_{i=1}^{n_J} \boldsymbol{P}_{Ji}}{n_J} \tag{B.9}$$

The vector from a point in the segment to the middle point of plane *J* is $\boldsymbol{P}_{Ji}$–$\boldsymbol{P}_{JM}$, *J* = B, C, and D, and *i* = 1, 2, …, n_J. Two groups of vectors $\boldsymbol{P}_{Ai} - \boldsymbol{P}_{AM}$ and $\boldsymbol{P}_{Ji} - \boldsymbol{P}_{JM}$ (*J* = B, C, and D) are combined together and a least square plane is calculated to fit these two combined segments. The normal vector of the least square plane is $\boldsymbol{N}$. The plane distance between two segments is $d = \left|\left(\boldsymbol{P}_{\boldsymbol{AM}} - \boldsymbol{P}_{\boldsymbol{JM}}\right) \cdot \boldsymbol{N}\right|$.

B.4.1.4. Step height measurement

The 3D profile of the Step Gage measured by the laser holographic interferometer is shown in Fig. B.7. The four steps A, B, C, and D corresponding to the four surfaces shown in Fig. B.5(a), are observed. The center points, marked as $\boldsymbol{P}_{AM}$, $\boldsymbol{P}_{BM}$, $\boldsymbol{P}_{CM}$, and $\boldsymbol{P}_{DM}$, of the four steps are identified to calculate the height.

The mean values, marked as μ_d, of the three measurement groups for Step Heights I, II, and III are listed in Table B.1. The deviation of μ_d from the target value is the accuracy of measurement system. As listed in Table B.1, the worst case accuracy in three

measurement groups for Step Heights I, II, and III are 0.1, 0.7, and 1.0 μm or 3%, 5%, and 3% of the target value, respectively. This demonstrates the μm-level accuracy of the laser holographic interferometer for the 3D profile measurement of the machined components.

B.4.2. Gage R&R evaluation

B.4.2.1. Measurement parts

Five automotive automatic transmission valve bodies from the production line are used to evaluate the gage R&R of the laser holographic interferometer. These five parts, from the same production line but with different clamps, have the same surface geometry. One of the five parts is shown in Fig. B.8. The size of the part is about 225 mm x 370 mm, which is larger than the FOV of the laser holographic interferometer under research. Because the flatness of the region enclosed by a dashed rectangle is critical to avoid the fluid leakage and this is the region under warranty by the manufacturing plant, only this region is measured for the gage R&R evaluation. The overall surface flatness tolerance of this region is 50 μm.

B.4.2.2. Measurement procedures

The parts are positioned on a 3-2-1 fixture, i.e., three blocks support the parts from the bottom, a pin through a hole of the part restricts the lateral x and y movement, and a stop bar in contact with the side surface of the part restricts the rotation about the pin.

The five parts are measured three times by two operators. Each operator measures the whole five parts for once before the operator switches.

B.4.2.3. Flatness measurement

An example of the 3D profile of the valve body measured by the laser holographic interferometer is shown in Fig. B.9. From the 3D profile measurement, the flatness can be calculated. Table B.2 shows the flatness measurements of the five parts by two

operators. Following the standard evaluation procedures [87,88], the gage R&R is calculated as 11 μm. Take 50 μm as the tolerance and the gage R&R is about 23%, which is in the acceptable condition. Due to the restriction of the current fixture, the part cannot be located with the pixel accuracy laterally and some edges might introduce some errors. The performance is expected better with a better fixture design.

B.5. Concluding remarks

In this appendix, the overview of the laser holographic interferometry and detailed study of the state-of-the-art laser holographic interferometer were presented. Features of the laser holographic interferometer were discussed. The principles of laser holographic interferometry were described. Detailed optical hardware setup and claimed specifications of a typical laser holographic interferometer, Coherix Shapix 1000, were presented. The performance of the system was evaluated.

The Coherix laser holographic interferometer is capable for the μm-level precision measurement on machined metal components. Limitations and potential research of this system are identified.

- *Limited field of view*: This system can measure parts within the 300 mm x 300 mm FOV. Only a portion of the surface area can be measured if the part, such as the engine head in Fig. 1.1, is larger than the FOV.
- *Limited depth-of-field*: This system can measure parts within the depth-of-field from 0.3 mm up to 17 mm depending on the optical configurations. The tradeoff of increasing the depth-of-field is the decrease of height measurement accuracy and resolution.
- *No capability for round surface measurement*: This system is targeted for flat surface measurement. If the surface is round such as a cylinder, very few amount of light can be reflected back from the round surface to generate the hologram, which is used for the calculation of 3D surface profile, due to the large surface curvature.

This research is aimed to solve the above problems for laser holographic interferometry, which are described in Chapter 2, Chapter 3, and Chapter 4, respectively.

Table B.1. Plane distance measurements of the step gage by the laser holographic interferometer.

Measurement method		Step height								
		I			II			III		
Profilometer	Target value (μm)	3.9			13.6			32.1		
Laser holographic interferometer	Group	1	2	3	1	2	3	1	2	3
	Mean, μ_d (μm)	4.0	3.9	3.9	13.1	12.9	13.0	32.7	31.8	31.1
	Difference (μm)	0.1	0.03	0.04	0.5	0.7	0.6	0.6	0.3	1.0
	Accuracy (μm)	0.1			0.7			1.0		
	Percentage of target value	3%			5%			3%		

μ_d: mean of step height

σ_d: standard deviation of step height

Table B.2. Gage R&R evaluation of the laser holographic interferometer.

Unit: μm

Operator	A ==> Operator #1			B ==> Operator #2		
Sample #	1st Trial	2nd Trial	3rd Trial	1st Trial	2nd Trial	3rd Trial
1	55.4	59.5	61.5	60.6	59.6	57.7
2	62.7	56.2	64.2	63.3	63.2	62.0
3	70.4	64.2	69.8	69.1	71.5	73.0
4	51.0	53.9	49.4	51.0	50.0	50.8
5	52.5	52.3	51.6	52.8	50.5	51.2

Repeatability = 11.3 μm

Reproducibility = 2.2 μm

Gage R&R = 11.5 μm

% Gage R&R = 23% for a 50 μm tolerance specification

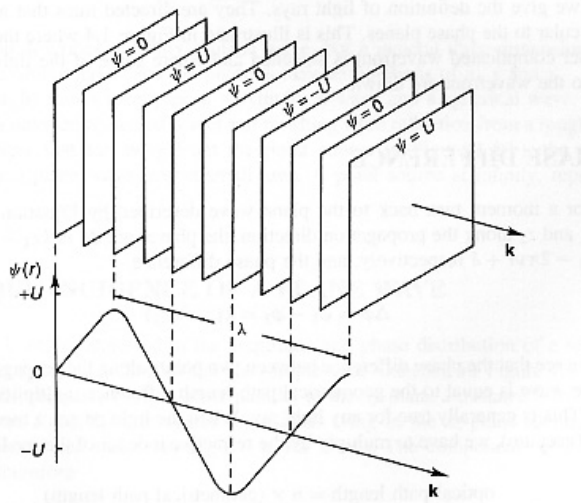

Fig. B.1. Plane light wave distribution in space at a time spot. [76]

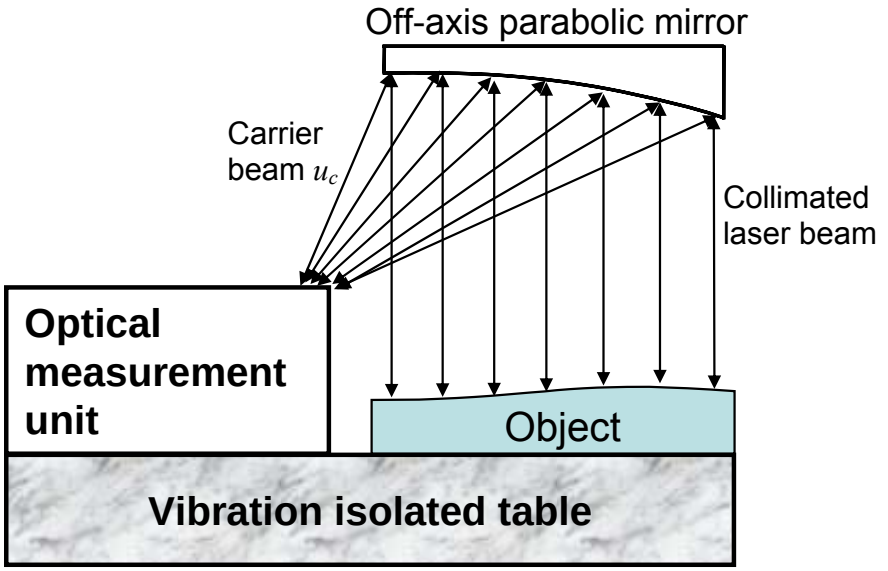

(a)

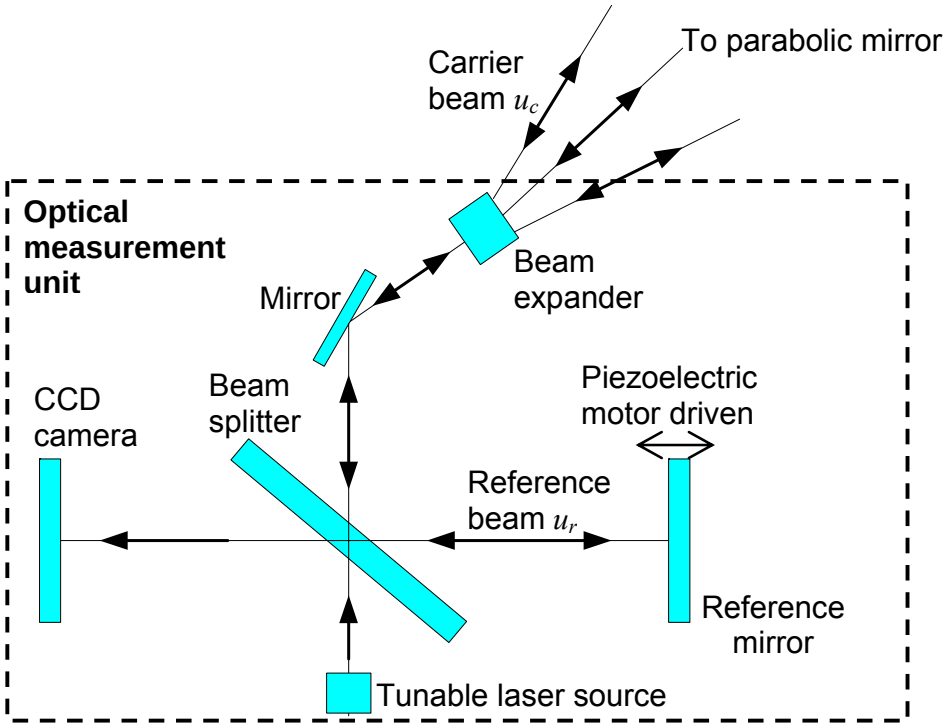

(b)

Fig. B.2. Diagram of the laser holographic interferometer: (a) configuration of the machine and (b) scheme of the optical measurement unit in (a).

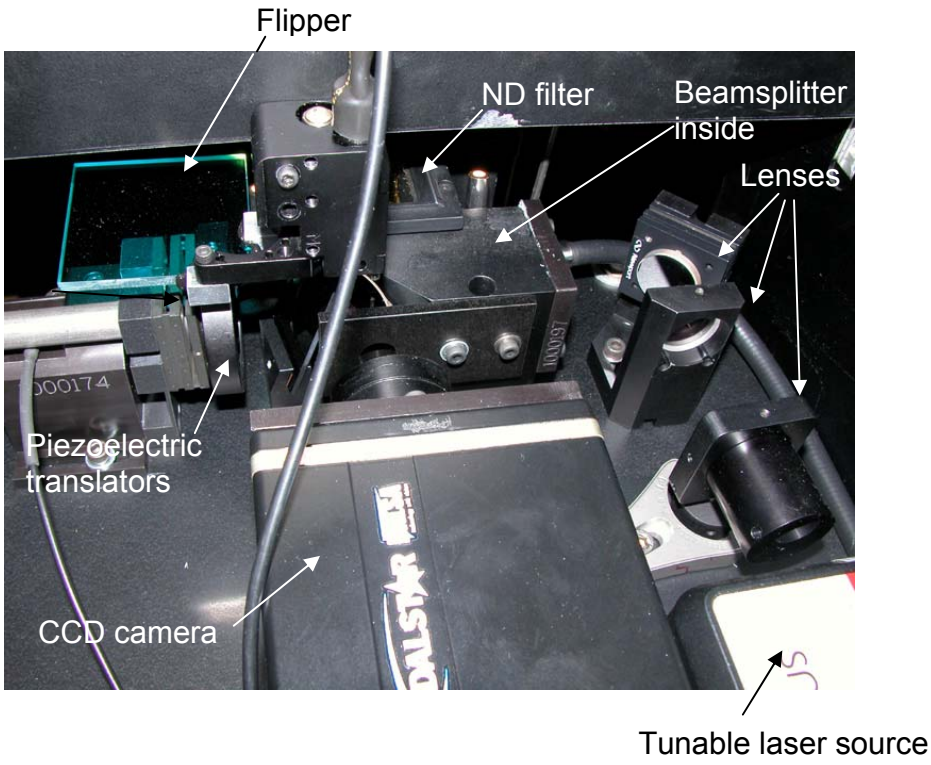

Fig. B.3. Optical configurations of the laser holographic interferometer under research.

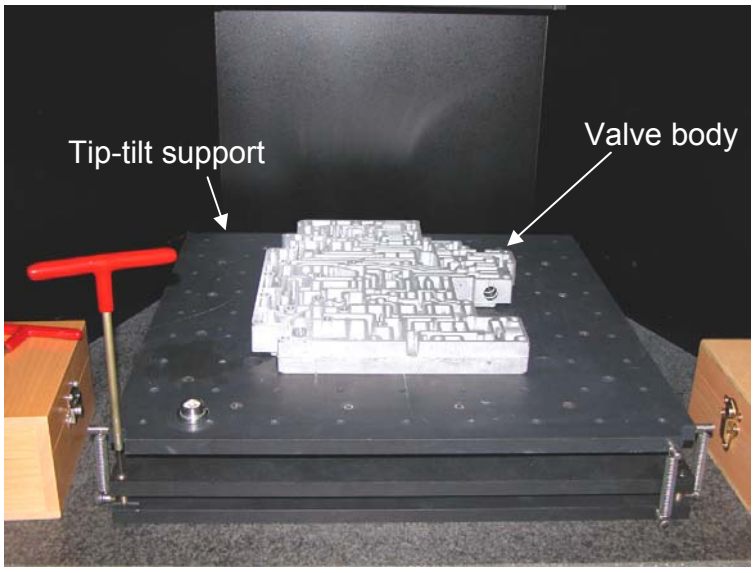

Fig. B.4. Valve body surface flatness measurement by the laser holographic interferometer.

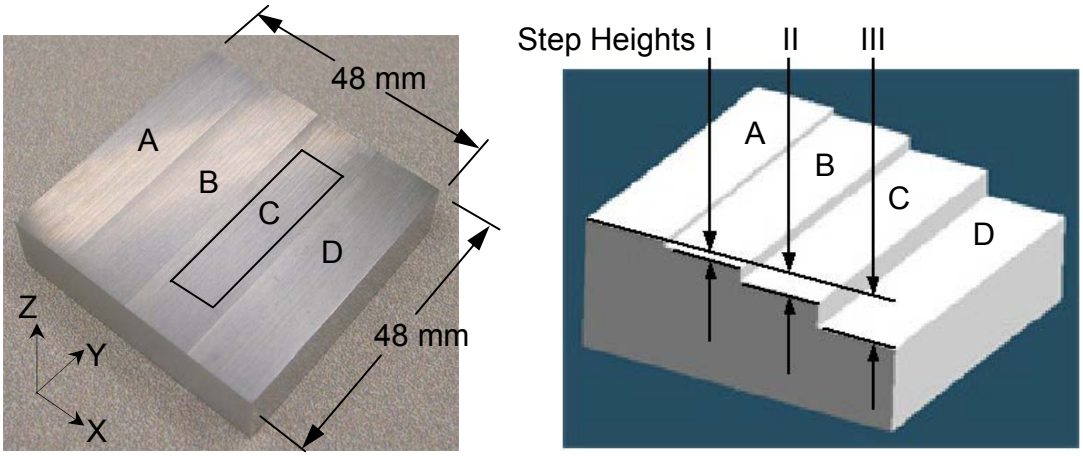

Fig. B.5. Step gage for performance evaluation: (a) overview and (b) CAD model.

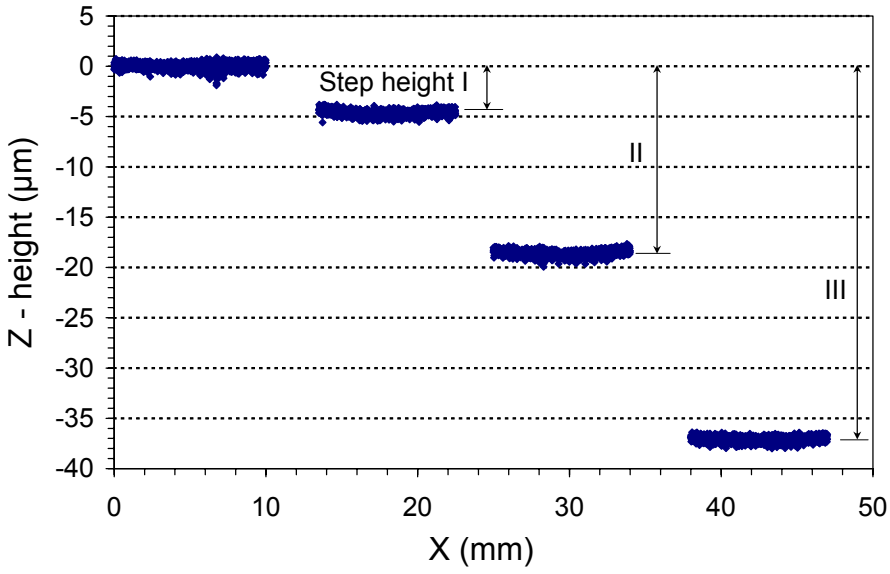

Fig. B.6. Target value measurement of the step heights by Taylor Hobson contact profilometer.

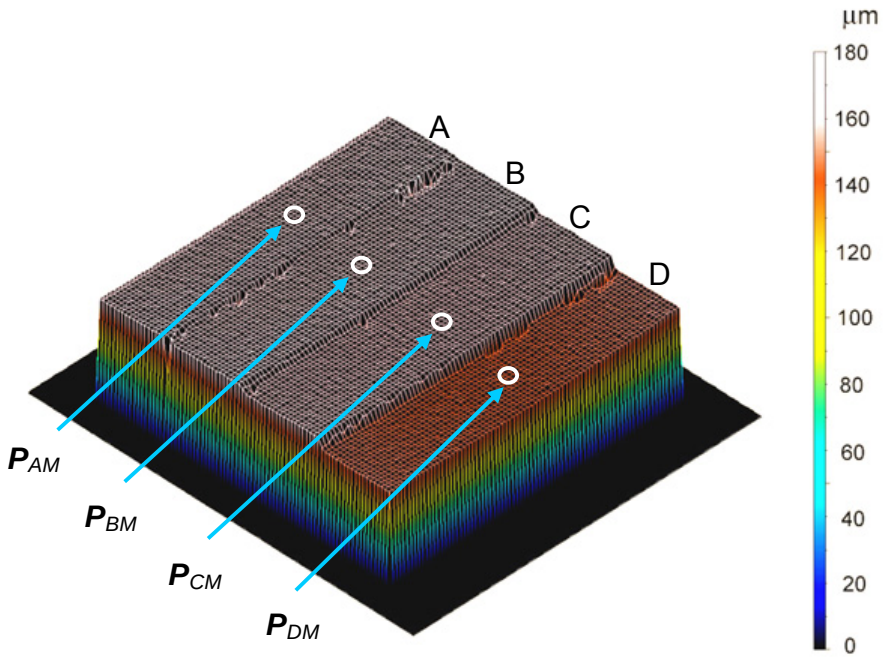

Fig. B.7. 3D profile of the step gage measured by the laser holographic interferometer.

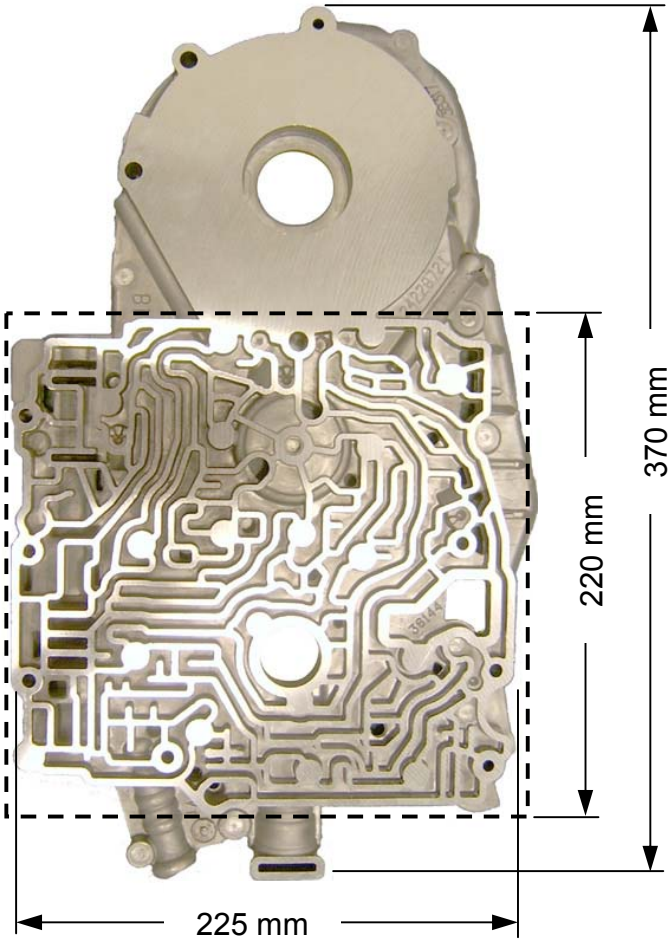

Fig. B.8. An automotive automatic transmission valve body for performance evaluation.

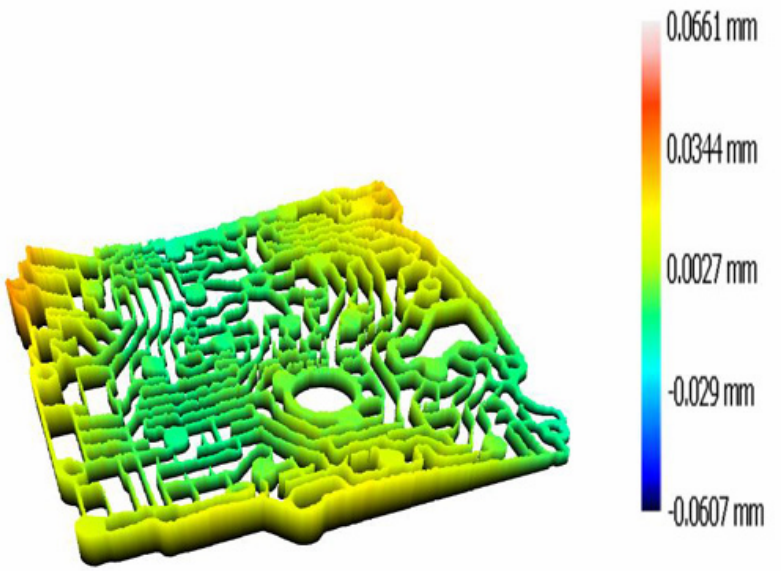

Fig. B.9. 3D profile of the automotive automatic transmission valve body measured by the laser holographic interferometry.

Appendix C

Flatness Evaluation for High Definition Measurements

C.1. Introduction

The goal of the geometric form evaluation is to determine the variation of actual part features with reference to the ideal features. In practice, all the geometric form evaluations are based on the measurement data, which contains both the variation of part features and the measurement errors. Figure C.1 illustrates the geometric form evaluation process based on the measurement data. The variation of part features is captured by the measurement system, which introduces the data acquisition error and possibly the registration error for combining multiple measurements if the part is larger than the field of view. The measured cloud of points contains both the variation of part features and the measurement errors. The geometric form evaluation method is to effectively estimate the variation of part features from the measurement data with errors.

The high definition measurement system usually generates a huge number (larger than a million) of data points, which impose a great challenge on how to evaluate the geometric form variations because the huge number of data points makes the small probability event of large measurement error happen frequently. Assume the measurement error of each point acquired by the high definition measurement system follows the normal distribution $N(\mu_e, \sigma_e)$ and the error of each point is independent on the others. The 99.73% of measured points will statistically have the measurement error in the range from $\mu_e - 3\sigma_e$ to $\mu_e + 3\sigma_e$. If the number of measured points is a hundred, the possibility that at least one point has the measurement error out of this range is 0.27. As

the number of measured points increases to a million level, the possibility to have points with large measurement errors increases significantly.

An example is elaborated to explain the problem of the current geometric form evaluation method for high definition measurement system. Let the flatness tolerance of the part be 100 μm. A capable measurement system must have the precision/tolerance ratio less than 20% [87]. This means that the repeatability of the measurement system $5.15\sigma_e$ must be smaller than 20 μm (= 100 μm x 20%), i.e., the standard deviation σ_e should be equal to or smaller than 3.9 μm. For a high definition measurement system with the deviation σ_e equal to 3.9 μm, if there are $1x10^7$ points measured in one acquisition, it will statistically have at least one data point with the measurement error larger than 21.8 μm. The current ANSI and ISO standards [89,90] define the flatness as the minimum zone which encloses all the measured data points of the part surface. Following this definition, the evaluated flatness can have an error up to 21.8 μm statistically due to the large number of data points by the high definition measurement system. This error is unacceptable in most industrial applications though the measurement system is capable by definition.

In this appendix, the preliminary research is conducted to quantitatively analyze the flatness evaluation errors of different methods for the high definition measurement system.

C.2. Mathematical analysis

The surface flatness is generally evaluated in two steps. First, a reference plane, to which the deviations of all the points are referred, is determined. Second, a flatness definition, such as the range of deviations of all the measured points from the identified reference plane, is applied to calculate the flatness.

C.2.1. Reference plane estimation

Two methods, least square and minimum zone, are mainly used to estimate the reference plane for flatness evaluation. The least square method identifies the reference

plane by least square fitting all the measured points. The minimum zone method defines the reference plane as the plane from which the range of deviations of all the measured points is the minimum.

The error in the estimation of the reference plane is different for the least square and minimum zone methods.

C.2.1.1. Least square estimation of the reference plane

The least square method assumes that the surface can be fitted with a plane equation:

$$z = a + bx + cy \tag{C.1}$$

where

z is the height of a surface point,

x and y are the lateral position of a surface point, and

a, b, and c are the coefficients of the plane equation. The a determines the shift in the height direction and b and c determine the orientation of the reference plane.

In practice, the part is not ideal and each point on the part surface has a deviation δ_i from the ideal plane and the Eq. (C.1) is modified as

$$z_i = a + bx_i + cy_i + \delta_i \tag{C.2}$$

where

z_i is the height of the point i on the part surface,

x_i and y_i are the lateral coordinates of the point i, and

δ_i is the deviation of the point i from the plane $z = a + bx + cy$.

Assume the measurement error ε_i of the point i is independent of other points and follows the normal distribution with the mean μ_e and variance σ_e^2. Then to include the measurement error, Eq. (C.2) is modified as

$$z_i + \varepsilon_i = a + bx_i + cy_i + \delta_i \tag{C.3}$$

The least square method minimizes the sum of squared deviation from the reference plane

$$\sum_i \left[z_i + \varepsilon_i - \left(a + bx_i + cy_i \right) \right]^2 = \min \tag{C.4}$$

To satisfy the Eq. (C.4), the parameters a, b, and c can be estimated by

$$\begin{bmatrix} a \\ b \\ c \end{bmatrix} = \begin{bmatrix} \sum 1 & \sum x_i & \sum y_i \\ \sum x_i & \sum x_i^2 & \sum x_i y_i \\ \sum y_i & \sum x_i y_i & \sum y_i^2 \end{bmatrix}^{-1} \begin{bmatrix} \sum z_i + \sum \varepsilon_i \\ \sum x_i z_i + \sum x_i \varepsilon_i \\ \sum y_i z_i + \sum y_i \varepsilon_i \end{bmatrix} \tag{C.5}$$

The mathematical expression of the parameters a, b, and c determined by the Eq. (C.5) is complicated. In order to simplify the expression without losing the generality,

the coordinate system is shifted to the center of the plane to satisfy the following conditions

$$\sum x_i = 0 \tag{C.6}$$

$$\sum y_i = 0 \tag{C.7}$$

$$\sum x_i y_i = 0 \tag{C.8}$$

Then the parameters a, b, and c are determined by

$$\begin{bmatrix} a \\ b \\ c \end{bmatrix} = \begin{bmatrix} \sum x_i^2 \sum y_i^2 \sum z_i + \sum x_i^2 \sum y_i^2 \sum \varepsilon_i \\ \sum 1 \sum y_i^2 \sum x_i z_i + \sum 1 \sum y_i^2 \sum x_i \varepsilon_i \\ \sum 1 \sum x_i^2 \sum y_i z_i + \sum 1 \sum x_i^2 \sum y_i \varepsilon_i \end{bmatrix} \Big/ \sum 1 \sum x_i^2 \sum y_i^2 \tag{C.9}$$

From Eq. (C.9), the means or expected value and variance of the estimated parameters a, b, and c due to the measurement error can be determined by

$$E\left(\begin{bmatrix} a \\ b \\ c \end{bmatrix}\right) = \begin{bmatrix} \sum x_i^2 \sum y_i^2 \sum z_i / \sum 1 \sum x_i^2 \sum y_i^2 + \mu_e \\ \sum 1 \sum y_i^2 \sum x_i z_i / \sum 1 \sum x_i^2 \sum y_i^2 \\ \sum 1 \sum x_i^2 \sum y_i z_i / \sum 1 \sum x_i^2 \sum y_i^2 \end{bmatrix} \tag{C.10}$$

and

$$V\left(\begin{bmatrix} a \\ b \\ c \end{bmatrix}\right) = \begin{bmatrix} \sigma_e^2 / \sum 1 \\ \sigma_e^2 / \sum x_i^2 \\ \sigma_e^2 / \sum y_i^2 \end{bmatrix} \tag{C.11}$$

where, $E(.)$ and $V(.)$ indicate the expected value and variance function, respectively.

It is observed from Eq. (C.10) that the expected values of the parameters b and c are not affected by the measurement error. This indicates that the orientation of the reference plane estimated by the least square method is expected to be the same with the measurement error. The μ_e change of the expected value of a does not affect the flatness evaluation because a only determines the shift of the reference plane in the height direction.

It is observed from Eq. (C.11) that as the number of measured points increases, the variance of the parameters b and c decreases. This indicates that the orientation of the reference plane estimated by the least square method is insensitive to the measurement error of the high definition measurement system which generates a huge number of data points.

C.2.1.2. Minimum zone estimation of the reference plane

Several approaches, such as Monte Carlo [91], simplex [91], and convex hull [92], have been developed to find the reference plane for minimum zone estimation.

The Monte Carlo approach randomly selects the values of the parameters a, b, and c to calculate the distance of the enclosing parallel plane pair. If the distance is smaller than the current, the parameters a, b, and c will be set to these values and the process is repeated until the change is below the threshold. Because of the random selection of parameters, the possibility of missing the true minimum is not ruled out [91] for this approach.

The simplex approach utilizes the gradient search to find the optimal combination of the parameters a, b, and c, which construct the enclosing parallel plane pair with minimum distance, for the reference plane.

The convex hull approach has two steps. First all the supporting planes, which have all the measured points on one side, are identified. Second, based on that the reference plane must be one of the supporting planes, this approach designates the

supporting plane, which constructs the enclosing parallel plane pair with minimum distance, as the reference plane.

Only the convex hull approach is considered in the following error analysis because the simplex approach should reach the reference plane very close to that of the convex hull approach. The reference plane defined by the convex hull approach is determined only by three measured points no matter which supporting plane is selected. Based on Eq. (C.11), the variation of the reference plane coefficients are inversely proportional to the sum of the squared coordinates of only these three points. Compared with the least square method, the reference plane determined by minimum zone method using the convex hull approach is more sensitive to the measurement error.

C.2.2. Flatness definition

The flatness is usually defined as the range of deviations, so called peak-to-valley, from the identified reference plane. However, this definition does not consider the effect of the possibly large measurement errors from the high definition measurement system.

Two other flatness definitions, the $6\sigma_f$ and the modified peak-to-valley, are proposed and analyzed.

C.2.2.1. $6\sigma_f$ flatness definition

This 6σ flatness calculates the standard deviation σ_f of the deviations of all the measured points from the identified reference plane and uses $6\sigma_f$ as the flatness.

This definition cuts off all the measured points outside of $6\sigma_f$ range and can effectively suppress the measurement error. However, this definition can also cut off or overestimate some true part variations. For example, the surface of the part has the simulated profile as shown in Fig. C.2(a). Assume the profile in Fig. C.2(a) is the true surface profile and does not have any measurement error. Most of the data points are concentrated in a very small height range and only a small center region of the profile is protruded in the height. The histogram of the height distribution is illustrated by Fig. C.2(b). The $6\sigma_f$ flatness is 23 μm, 71 μm smaller than the 94 μm peak-to-valley flatness

with the reference plane defined by the least square method because the protruded profile is cut off by the $6\sigma_f$ flatness definition.

C.2.2.2. Modified peak-to-valley flatness definition

A criterion is proposed to modify the peak and valley points if large measurement errors on these two points are identified. All the measured points are sorted in the sequence of deviation. The peak point with maximum deviation and the valley point with minimum deviation from the reference plane are identified. The local 5 x 5 region centered at the peak point is least square fitted by a plane. The trend of the fitted plane is subtracted from the local region. If there is another point which has the height value within the σ_f range from the height value of the peak point in the local region, this peak point will be used for flatness evaluation. Otherwise, this peak point is discarded as the point with large measurement error and the point next to the peak point in the sequence will be checked. This process is repeated until the peak point is found. The same process is conducted on the valley point. The flatness is defined as the range of deviations of the peak and valley points determined by the proposed criterion from the identified reference plane.

C.3. Simulations

Five surface profiles are simulated to investigate the flatness evaluation errors on different part variations. A random noise with normal distribution is added to the surface profile. The reference plane and the flatness are estimated from the generated surface profile plus the random measurement error.

The five surface profiles are generated in a matrix with the dimension 1024 x 1024 to simulate the measurement result by the high definition measurement system. The ranges of the lateral coordinates x and y are both from 1 to 1024 for the five surface profiles.

Profile 1: an ideal horizontal plane, as shown in Fig. C.3(a). The surface expression is $z = 0$ mm. The height distribution histogram of this surface profile is illustrated in Fig. C.3(b). All the data points are concentrated at the height position 0 mm.

Profile 2: an ideal tilted plane, as shown in Fig. C.4(a). The surface expression is $z = 5\times10^{-5}x + 2\times10^{-5}y$ mm. The height distribution histogram of this surface profile approximates the normal distribution, as illustrated in Fig. C.4(b). The minimum and maximum heights are 7×10^{-5} mm and 0.072 mm, respectively.

Profile 3: an ideal bowl-shaped plane, as shown in Fig. C.5(a). The surface expression is $z = 1.92\times10^{-5}[(x - 512)^2 + (y - 512)^2]$ mm. The height distribution histogram of this surface profile is illustrated in Fig. C.5(b). The distribution of data points with height smaller than 0.05 mm levels around 16%. As the height of points increases above 0.05 mm, the percentage of points decreases. The minimum and maximum heights are 0 mm and 0.100 mm, respectively.

Profile 4: a plane with a protrusion in the center and some ripples around the protrusion, as shown in Fig. C.2(a). The surface expression is $z = 0.077\left[\frac{\sin(0.02x-10)}{(0.02x-10)} + \frac{\sin(0.02y-10)}{(0.02y-10)}\right]$ mm. The height distribution histogram of this surface profile is illustrated in Fig. C.2(b). More than 90% of the points are concentrated in the height range close to 0 mm. The minimum and maximum heights are –0.017 mm and 0.077 mm, respectively.

Profile 5: a surface composed of multiple sine functions, as shown in Fig. C.6(a). The surface expression is $z = 0.01[\sin(6.13\times10^{-3}x) + \sin(1.53\times10^{-2}x) + \sin(9.20\times10^{-3}y) + \sin(2.15\times10^{-2}y) + \sin(3.99\times10^{-2}y)]$ mm. The height distribution histogram of this surface profile approximates the normal distribution as illustrated in Fig. C.4(b). The minimum and maximum heights are –0.049 mm and 0.038 mm, respectively.

A random noise matrix, following the normal distribution with the mean and standard deviation equal to 0 μm and 3.9 μm, respectively, is added to each of the five generated surface profile. Using the methods described in Sec. C.2, the reference plane and the flatness are estimated from the generated surface profiles with the random noises.

To investigate the statistics of the flatness evaluation error, the evaluation is repeated 1000 times with 1000 different random noise samples.

Table C.1 lists the standard deviations σ_a, σ_b, and σ_c of the coefficients a, b, and c, respectively, of the estimated reference planes from the 1000 evaluations for the five surface profiles using the least square and convex hull minimum zone methods. Only the coefficients b and c are considered because they determine the orientation of reference plane which affects the flatness evaluation result.

The standard deviations σ_b and σ_c estimated by the least square method is very stable on the five surface profiles, as shown in Table C.1. This indicates that the variation of the orientation of the reference plane estimated by the least square method is independent on the surface profile. The standard deviations σ_b and σ_c estimated by the convex hull minimum zone method changes on different surface profiles. The maximum σ_b is 1.3×10^{-5} mm for the profile 4 of a plane with protrusion and the minimum σ_b is 1.6×10^{-6} mm for the profile 1 of a perfect horizontal plane. This indicates that the variation of the orientation of the reference plane estimated by the convex hull minimum zone method is dependent on the surface profile.

The standard deviations σ_b and σ_c estimated by the convex hull minimum zone method are always larger (from 100 to 1000 times) than those estimated by the least square method for all the five surface profiles, as shown in Table C.1. For example, the σ_b and σ_c estimated by the convex hull minimum zone method are 1.3×10^{-5} mm for the profile 4 of a plane with protrusion and those estimated by the least square methods are 1.1×10^{-8} mm. With the 1024 x 1024 dimension of the measurement matrix, the maximum 3σ tilt error of the reference plane from one corner of the plane to the other is about 69 μm for the convex hull minimum zone method and is about 0.07 μm for the least square method. This verifies the argument in Sec. C.2 that the reference plane estimated by the least square method is more robust to measurement errors compared with minimum zone method.

Table C.2 shows the mean and standard deviation of the estimated flatness from the 1000 evaluations for the five surface profiles. For each surface profile, the reference

planes estimated by the least square and minimum zone methods are used. With the identified reference plane, the three flatness definitions, discussed in Sec. C.2.2.2, are applied for evaluation.

The least square and minimum zone methods are compared in the mean and standard deviations of the evaluated flatness for different surface profiles using the three flatness definitions. The mean of evaluated flatness by the minimum zone is always about 1 μm smaller than that of the least square method for the peak-to-valley definition on different surface profiles. For the modified peak-to-valley flatness definition, the relation of the evaluated flatness between minimum zone and least square methods is not definite for different surface profiles. However, the difference of the evaluated flatness between the two methods for both the peak-to-valley and modified peak-to-valley flatness definitions is still not significant (about 1 μm). The standard deviations of evaluated flatness by the least square and minimum zone methods are of the same level (about 1.5 μm) for different surface profiles.

The three flatness definitions are compared in the mean and standard deviations of the evaluated flatness for different surface profiles using the least square and minimum zone methods.

The $6\sigma_f$ definition effectively cuts off the measurement error effect than the other two definitions for the profiles 1 and 2, which do not have the part variation. However, the $6\sigma_f$ definition overestimates the flatness for the profile 3 of a bowl-shaped surface and underestimates the flatness for the profile 4 of a plane with protrusion because this definition does not consider the part variation separately from the measurement error as described in Sec. C.2. This indicates the $6\sigma_f$ flatness definition should not be used generally. The modified peak-to-valley definition effectively suppresses the measurement error for the profiles 1 and 2. However, this definition does not indicate much advantage over the peak-to-valley definition to suppress the measurement error for the other three surface profiles. This is because the points with large measurement errors, which are discarded by the modified peak-to-valley definition, can be randomly distributed in some regions of the surface profile which does not have contribution to the

flatness evaluation due to that these regions are not on the top or bottom of the whole surface profile.

The standard deviations of evaluated flatness by the peak-to-valley and modified peak-to-valley definitions are at the same level and are stable for different surface profiles. The standard deviation of the $6\sigma_f$ definition changes significantly for different surface profiles.

In summary, several observations are made based on the analysis of simulation results of the reference plane and flatness evaluation shown in Tables C.1 and C.2. First, the orientation of the reference plane estimated by the least square method is more robust than the minimum zone method. Second, the difference of the evaluated flatness between the least square and minimum zone methods is not significant with the measurement errors of high definition measurement system. Third, the $6\sigma_f$ definition should not be applied generally because it is dependent on the part variation and the possibility of underestimation and overestimation is not ruled out. Last, the modified peak-to-valley definition can effectively suppress the large measurement errors which impact the flatness evaluation though this effect of the definition is not necessarily detected in some cases.

C.4. Concluding remarks

The flatness evaluation for the high definition measurements was discussed. The mathematical analysis of the reference plane estimation error by the least square and minimum zone methods was conducted. The widely used peak-to-valley flatness definition and two proposed flatness definitions, $6\sigma_f$ and modified peak-to-valley, were analyzed. Five surface profiles with the random measurement errors were generated to simulate the flatness evaluation process for the high definition measurement system. The least square method with the modified peak-to-valley definition was demonstrated to have the good potential among the analyzed methods to effectively evaluate the flatness with good noise robustness for the high definition measurement system.

This is an exploratory study of the geometrical form evaluation for the high definition measurements. Many research investigations can follow. For example, a theoretical error analysis of other flatness evaluation methods such as the minimum average [93] and function-oriented evaluation [94] can be developed. A more comprehensive mathematical method shall be developed to quantitatively analyze error flows starting from each measured points to the final evaluated flatness result for the high definition measurement system. The research in this appendix can also be extended to other more complicated geometric forms, such as cylinder and sphere.

Table C.1. Standard deviation of reference plane coefficients for flatness evaluation.

Part variation	Least square			Convex hull minimum zone		
	σ_a (mm)	σ_b (mm)	σ_c (mm)	σ_a (mm)	σ_b (mm)	σ_c (mm)
Profile 1	8.9×10^{-6}	1.1×10^{-8}	1.1×10^{-8}	1.6×10^{-2}	1.6×10^{-6}	1.6×10^{-6}
Profile 2	9.1×10^{-6}	1.1×10^{-8}	1.1×10^{-8}	1.6×10^{-2}	1.7×10^{-6}	1.6×10^{-6}
Profile 3	8.9×10^{-6}	1.1×10^{-8}	1.1×10^{-8}	1.5×10^{-3}	1.9×10^{-6}	1.8×10^{-6}
Profile 4	8.9×10^{-6}	1.1×10^{-8}	1.1×10^{-8}	9.1×10^{-3}	1.3×10^{-5}	1.3×10^{-5}
Profile 5	9.1×10^{-6}	1.1×10^{-8}	1.1×10^{-8}	2.7×10^{-3}	3.3×10^{-6}	1.9×10^{-6}

Table C.2. Flatness evaluation error analysis of different methods.

Part variation	Method to determine the reference plane	Mean of evaluated flatness (μm)			Standard deviation of evaluated flatness (μm)		
		Peak-to-valley	$6\sigma_f$	Modified peak-to-valley	Peak-to-valley	$6\sigma_f$	Modified peak-to-valley
Profile 1	Least square	33.1	20.4	27.4	1.2	0.01	1.1
	Minimum zone	32.5	20.9	28.2	1.0	0.4	1.2
Profile 2	Least square	33.2	20.4	27.3	1.2	0.01	1.0
	Minimum zone	32.6	20.8	28.2	1.0	0.4	1.3
Profile 3	Least square	122.7	129.2	122.7	1.6	0.02	1.6
	Minimum zone	121.8	129.2	121.8	1.3	0.09	1.3
Profile 4	Least square	112.4	30.6	111.2	1.7	0.02	1.5
	Minimum zone	111.6	43.3	111.4	1.6	7.5	1.5
Profile 5	Least square	105.4	88.8	105.4	1.7	0.02	1.7
	Minimum zone	104.0	89.4	104.0	1.5	0.6	1.5

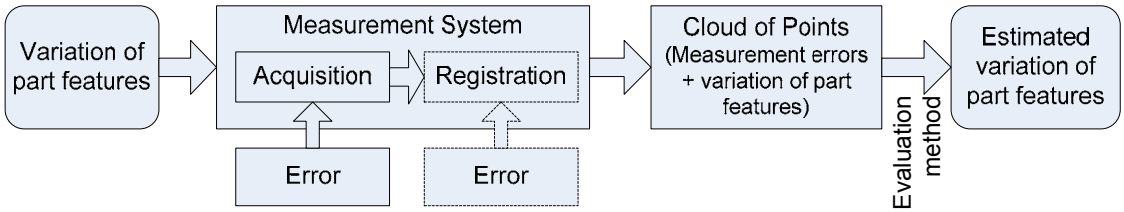

Fig. C.1. Geometric form evaluation based on the measurement data with the part and measurement variations.

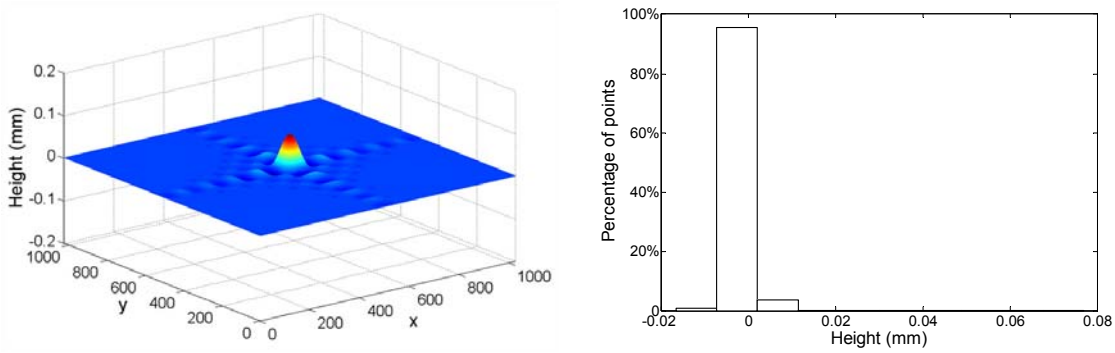

(a) (b)

Fig. C.2. Simulated part variation of profile 4 without measurement errors: (a) 3D profile and (b) histogram of height distribution.

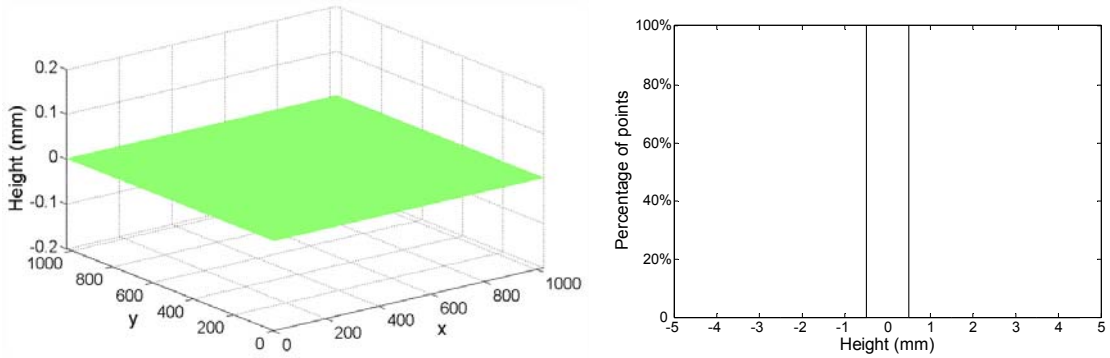

(a) (b)

Fig. C.3. Simulated part variation of profile 1 without measurement errors: (a) 3D profile and (b) histogram of height distribution.

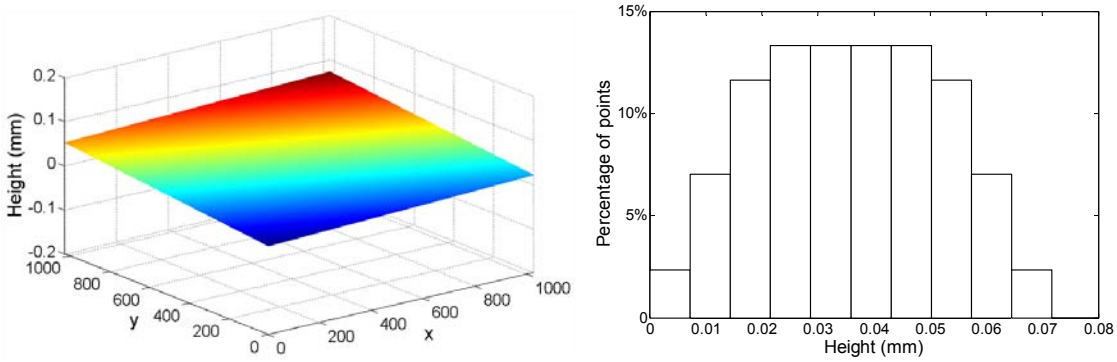

(a) (b)

Fig. C.4. Simulated part variation of profile 2 without measurement errors: (a) 3D profile and (b) histogram of height distribution.

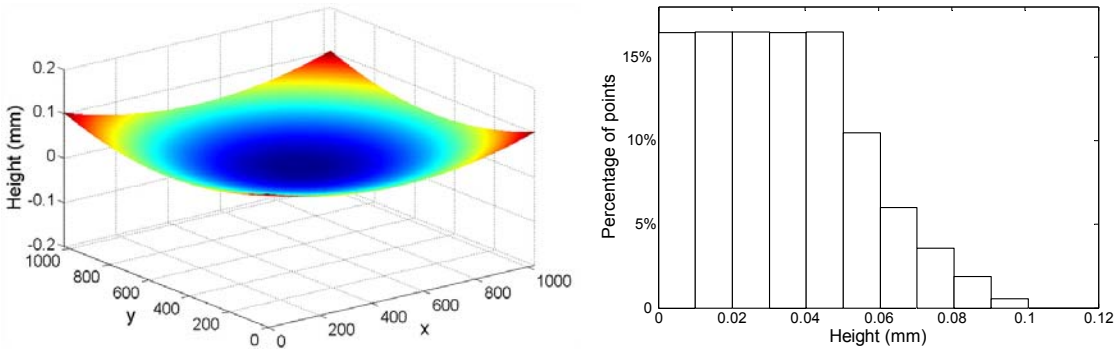

(a) (b)

Fig. C.5. Simulated part variation of profile 3 without measurement errors: (a) 3D profile and (b) histogram of height distribution.

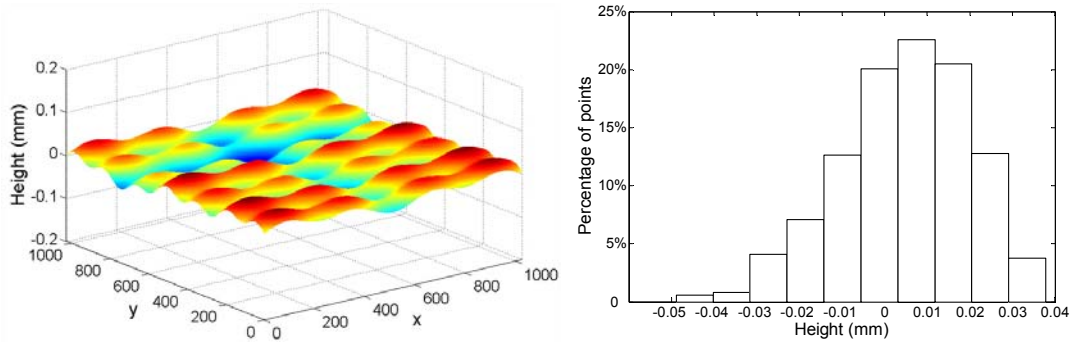

(a) (b)

Fig. C.6. Simulated part variation of profile 5 without measurement errors: (a) 3D profile and (b) histogram of height distribution.

References

1. White, D. A. and Shry, J., 2000, "Noncontact Measurement for Today and Tomorrow," *Quality Digest*.
2. Bradley, C., 1998, "Computer Vision Techniques in Reverse Engineering," *Engineering Design and Automation*, Vol. 4, pp. 101-12.
3. Maa, H. G., 2002, "Methods for Measuring Height and Planimetry Discrepancies in Airborne Laserscanner Data," *Photogrammetric Engineering and Remote Sensing,* Vol.68, pp. 933-40.
4. Rooks, B. W., 1997, "Vision Helping the Automotive Industry to Better Customer Choice," *Industrial Robot*, Vol. 24, pp. 48-51.
5. Buckberry, C. H., Towers, D. P., Stockley, B, C., Tavender, B., Jones, M. P., Jones, J. D. C., and Valera, J. D. R., 1996, "Whole-Field Optical Diagnostics for Structural Analysis in the Automotive Industry," *Optics and Lasers in Engineering*, Vol. 25, No. 6, pp. 433-453.
6. Beeck, M. A. and Hentschel, W., 2000, "Laser Metrology — A Diagnostic Tool in Automotive Development Processes," *Optics and Lasers in Engineering*, Vol. 34, No. 2, pp. 101-120.
7. Leopold, J., and Günther, H., 2002, "Fast 3D Measurement of Gear Wheels," *Proceedings of the SPIE - The International Society for Optical Engineering*, Vol. 4900, pp. 185-194.
8. Chen, F., Marchi, M. M., and Allen, T. E., 2002, "Powertrain Engineering Using Holographic/Electronic Speckle Pattern Interferometry," *Proceedings of the SPIE - The International Society for Optical Engineering*, Vol. 4778, pp. 302-311.
9. Zollne, F., Matusevich, V., and Kowarschik, R., 2003, "3D Measurement by Stereophotogrammetry," *Proceedings of the SPIE on Optical Measurement Systems for Industrial Inspection III*, Vol. 5144, pp. 311-314.
10. Trolinger, J. D., 1996, "Ultrahigh Resolution Interferometry," *Proceedings of the SPIE - The International Society for Optical Engineering*, Vol. 2861, pp. 114-123.
11. Kozhevatov, I.E.; Kulikova, E.Kh, 2001, "Interferometric Methods for Surface Testing High-Order White-Light Interferometer," *Instruments and Experimental Techniques*, Vol. 44, No. 1, pp. 84-87.
12. Zou, D., Ye, S., and Wang, C., 1995, "Structured-Lighting Surface Sensor and Its Calibration," *Optical Engineering*, Vol. 34, No. 10, pp. 3040-3043.
13. Wan, G., Nosekabel, E. H., 1999, "Surface Inspection on Bodies in White in Automotive Industry," *Proceedings of SPIE*, Vol. 3824, pp. 329-333.
14. Fraser, C. S., 1992, "Photogrammetric Measurement to One Part in a Million," *Photogrammetric Engineering and Remote Sensing*, Vol. 58, No. 3, pp. 305-310.
15. Kafri, O. and Glatt I., 1989, *The Physics of Moire Metrology*, John Wiley & Sons.
16. Wykes, C. and Morshedizadeh, R., 1995, "Surface Topography Measurement Using Digital Moiré Contouring – Errors and Limitations," *Proceedings of the Institution of*

Mechanical Engineers, Part B: Journal of Engineering Manufacture, Vol. 209, No. B4, pp. 317-325.

17. Xie, X., Atkinson, J. T., Lalor, M. J., and Burton, D., 1997, "Effects on Absolute Moiré Contouring by Using Gratings with Different Period and Profile and Rotating Angles," *Optics and Lasers in Engineering*, Vol. 27, No. 3, pp. 247-257.
18. Hamilton, D. K. and Wilson, T., 1982, "Three-Dimensional Surface Measurement Using the Confocal Scanning Microscope," *Applied Physics B*, Vol. 27, No. 4, pp. 211-213.
19. Mignot, J., and Gorecki, C., 1983, "Measurement of Surface Roughness: Comparison between a Defect-of-Focus Optical Technique and the Classic Stylus Technique," *Wear*, Vol. 87, No. 1, pp. 39-49.
20. Kilpelä, A., Pennala, R., and Kostamovaara, J., 2001, "Precise Pulsed Time-of-Flight Laser Range Finder for Industrial Distance Measurements," *Review of Scientific Instruments*, Vol. 72, No. 4, pp. 2197-2202.
21. Wang, L. S., Jambunathan, K., Dobbins, B. N., and He, S. P., 1996, "Measurement of Three-Dimensional Surface Shape and Deformations Using Phase Stepping Speckle Interferometry," *Optical Engineering*, Vol. 35, No. 8, pp. 2333-2340.
22. Chen, F., Brown, G. M., and Song, M., 2000, "Overview of Three-Dimensional Shape Measurement Using Optical Methods," Optical Engineering, Vol. 39, No. 1, pp. 10-22.
23. VanderLugt, A. B., "Signal Detection by Complex Spatial Filtering," IEEE Transaction on Information Theory, 1964, Vol. 10, No. 2, pp. 139-145.
24. Kim, T. and Poon, T. C., "Three-Dimensional Matching by Use of Phase-Only Holographic Information and the Wigner Distribution," *Journal of the Optical Society of America A (Optics, Image Science and Vision)*, 2000, Vol. 17. No. 2, pp. 2520-2528.
25. Kim, T., Poon, T. C., Wu, M. H., Shinoda, K., and Suzuki, Y., "Three-Dimensional Image Matching Using Two-Dimensional Optical Heterodyne Scanning," *Optical Memory and Neural Networks*, 1999, Vol. 8, No. 3, pp. 139-145.
26. Dias, P., Sequeira, V., Goncalves, J.G.M., and Vaz, F., "Automatic Registration of Laser Reflectance and Colour Intensity Images for 3D Reconstruction," *Robotics and Autonomous Systems*, 2002, Vol. 39, pp. 157-168.
27. Hsu, L. Y. and Loew, M. H., "Evaluation of the Accuracy of an Edge-Based Approach for Multimodality Brain Image Registration," *Proceedings of the SPIE - The International Society for Optical Engineering*, 2000, Vol. 3979, pp. 360-371.
28. Hsu, L. Y. and Loew, M. H., "Fully Automatic 3D Feature-Based Registration of Multi-Modality Medical Images," *Image and Vision Computing*, 2001, Vol. 19, No. 1-2, pp. 75-85.
29. Shalom, T., "System and Method for Aligning a Locally-Reconstructed Three-Dimensional Object to a Global Coordinate System Using Partially-Detected Control Points," 2003, United States Patent #: 6556705.

30. Shalom, T., Zelnik, I. and Goldberger J., "System and Method for 'Stitching' a Plurality of Reconstructions of Three-Dimensional Surface Features of Object(S) in a Scene Defined Relative to Respective Coordinate Systems to Relate Them to a Common Coordinate System," 2001, United States Patent #: 6201541.

31. Haralick, R. M. and Shapiro, L. G., *Computer and Robot Vision, Volume II*, 1992, Addison-Wesley.

32. Reddy, B. S. and Chatterji, B. N., "An FFT-Based Technique for Translation, Rotation, and Scale-Invariant Image Registration," *IEEE Transactions on Image Processing*, 1996, Vol. 5, No. 8, pp. 1266-1271.

33. Jähne, B., *Practical Handbook on Image Processing for Scientific and Technical Applications*, 2004, CRC Press.

34. Whitehouse, D. J., *Handbook of Surface Metrology*, 1994, Institute of Physics Publishing.

35. Strand, J., Taxt, T., and Jain, A. K., "Two-dimensional phase unwrapping using a block least-squares method," *IEEE Transactions on Image Processing*, 1999, Vol. 8, No. 3, pp. 375-386.

36. Huntley, J. M. and Saldner, H. "Temporal phase-unwrapping algorithm for automated interferogram analysis," *Applied Optics*, 1993, Vol. 32, No. 17, pp. 3047-3052.

37. Huntley, J. M. and Saldner, H. O., "Shape measurement by temporal phase unwrapping: comparison of unwrapping algorithms," *Measurement Science and Technology*, 1997, Vol. 8, No. 9, pp. 986-992.

38. Saldner, H. O. and Huntley, J. M., "Temporal phase unwrapping: application to surface profiling of discontinuous objects," *Applied Optics*, 1997, Vol. 36, No. 13, pp. 2770-2775.

39. Gasvik, K. J., *Optical Metrology*, John Wiley & Sons, 2002, Hoboken, NJ.

40. Friedlander, B. and Francos, J. M., "Model based phase unwrapping of 2-D signals," *IEEE Transactions on Signal Processing*, 1996, Vol. 44, 2999–3007.

41. Liang, Z. P., "A model-based method for phase unwrapping," *IEEE Transactions on Medical Imaging*, 1996, Vol. 15, No. 6, pp. 893–897.

42. Leitao, J. and Figueiredo, M. A., "Interferometric image reconstruction as a nonlinear bayesian estimation problem," in *Proceedings International Conference on Image Processing*, 1995, pp. 453–456.

43. Ghiglia, D. C. and Romero, L. A., "Robust two-dimensional weighted and unweighted phase unwrapping that uses fast transforms and iterative methods," *Journal of the Optical Society of America A (Optics and Image Science)*, 1994, Vol. 11, No. 1, pp. 107-117.

44. Huntley, J. M. and Coggrave, C. R., "Progress in phase unwrapping," *Proceedings of the SPIE - The International Society for Optical Engineering*, 1998, Vol. 3407, pp. 86-93.

45. Huntley, J. M., "Noise-immune phase unwrapping algorithm," *Applied Optics*, 1989, Vol. 28, No. 15, pp. 3268-3270.

46. Cusack, R., Huntley, J. M., and Goldrein, H. T., "Improved noise-immune phase-unwrapping algorithm," *Applied Optics*, 1995, Vol. 34, No. 5, pp. 781-789.

47. Buckland, J. R., Huntley, J. M., and Turner, S. R. E., "Unwrapping noisy phase maps by use of a minimum-cost-matching algorithm," *Applied Optics*, 1995, Vol. 34, No. 23, pp. 5100-5108.

48. Quiroga, J. A., Gonzalez-Cano, A., and Bernabeu, E., "Stable-marriages algorithm for preprocessing phase maps with discontinuity sources," *Applied Optics*, 1995, Vol. 34, No. 23, pp. 5029-5038.

49. Gutmann, B. and Weber, H., "Phase unwrapping with the branch-cut method: role of phase-field direction," *Applied Optics*, 2000, Vol. 39, No. 26, pp. 4802-4816.

50. Chang, H. Y., Chen, C. W., Lee, C. K., and Hu, C. P., "The tapestry cellular automata phase unwrapping algorithm for interferogram analysis," *Optics and Lasers in Engineering*, 1998, Vol. 30, pp. 487-502.

51. Strand, J. and Taxt, T., "Two-dimensional phase unwrapping using robust derivative estimation and adaptive integration," *IEEE Transactions on Image Processing*, 2002, Vol. 10, No. 10, pp. 1192-1200.

52. Huang, M. J. and He, Z. N., "Phase unwrapping through region-referenced algorithm and window-patching method," *Optics Communications*, 2002, Vol. 203, pp. 225-241.

53. Huang, Z., Shih, A. J., and Ni, J., "Laser interferometry hologram registration for three-dimensional precision measurements," *Journal of Manufacturing Science and Engineering Transactions of the ASME* (in press).

54. Stephenson, P., Burton, D. R., and Lalor, M. J., "Data validation techniques in a tiled phase unwrapping algorithm," *Optical Engineering*, 1994, Vol. 33, No. 11, pp. 3703-3708.

55. Gonzalez, R. C. and Woods, R. E., *Digital Image Processing*, 2002, Prentice Hall, Upper Saddle River, NJ.

56. Wu, C. F. J. and Hamada, M., *Experiments: Planning, Analysis, and Parameter Design Optimization*, 2000, John Wiley and Sons, New York.

57. Neter, J. and Wasserman, W., *Applied Linear Statistical Models*, 1974, Richard D. Irwin, Inc.

58. Huang, M. J. and Sheu, W. H., "Histogram-data-orientated filter for inconsistency removal of interferometric phase maps," *Optical Engineering*, 2005, Vol. 44, No. 4, 45602-1-11.

59. T. Tsukada and Y. Dahai, "A Study on Evaluation of Circularity and Related Features for Eccentric Cam Shaft (1st Report) – Development of Algorithm and Its Simulation," *International Journal of the Japan Society for Precision Engineering*, 1995, Vol. 29, No. 1, pp. 80-85.

60. T. Tsukada and Y. Dahai, "A Study on Evaluation of Circularity and Related Features for Eccentric Cam Shaft (2nd Report) – Measured Results and Discussion," *International Journal of the Japan Society for Precision Engineering*, 1995, Vol. 29, No. 2, pp. 150-155.

61. Dean J.W. Dawson, "Cylindricity and Its Measurement," *International Journal of Machine Tools and Manufacture*, 1992, Vol. 32, No. 1/2, pp. 247-253.

62. Y. Kakino and J. Kitazawa, "In Situ Measurement of Cylindricity," *Annals of the CIRP*, 1978, Vol. 27, No. 1, pp. 371-375.

63. S. Y. Li, M. N. Qin, and C. J. Li, "On-line Cylindricity Measurement and Error Compensating Control in Ultra-Precision Lathe," *SPIE Measurement Technology and Intelligent Instruments*, 1993, Vol. 2101, pp. 991-994.

64. A. W. Kulawiec, "Interferometric Measurement of Absolute Dimensions of Cylindrical Surfaces at Grazing Incidence," 1998, United States Patent #: 5,777,738.

65. Z. Huang, A. J. Shih, and J. Ni, "Laser Interferometry Hologram Registration for Three-Dimensional Precision Measurements," *ASME Journal of Manufacturing Science and Engineering* (in press).

66. H. Goldstein, *Classical Mechanics*, 1980, 2nd ed. Addison-Wesley, pp. 164-166.

67. K. Carr and P. Ferreira, "Verification of Form Tolerances Part II: Cylindricity and Straightness of A Median Line," 1995, *Precision Engineering*, Vol. 17, pp. 144-156.

68. A. B. Forbes, "Least-Squares Best-Fit Geometric Elements," NPL Rep DITC 140/89, National Physics Laboratory, UK, April 1989.

69. H. Y. Lai, W. Y. Jywe, C. K. Chen, and C. H. Liu, "Precision modeling of form errors for cylindricity evaluation using genetic algorithms," *Precision Engineering*, 2000, Vol. 24, pp. 310-319.

70. O. Devillers and F. P. Preparata, "Culling a set of points for roundness or cylindricity evaluations," *International Journal of Computational Geometry & Applications*, 2003, Vol. 13, No. 3, pp. 231-240.

71. http://www.haascnc.com/ROTARY_specs.asp?ID=43&mdl=HA5C#RotaryTreeModel

72. Leith, E. N. and Upatneiks, J., "Reconstructed Wavefronts and Communication Theory," *Journal of Optical Society of America*, 1962, Vol. 52, pp. 1123-1130.

73. Leith, E. N. and Upatneiks, J., "Wavefront Reconstruction with Continuous-Tone Objects," *Journal of Optical Society of America*, 1963, Vol. 53, pp. 1377-1381.

74. Leith, E. N. and Upatneiks, J., "Wavefront Reconstruction with Diffused Illumination and Three-Dimensional Objects," *Journal of Optical Society of America*, 1964, Vol. 54, pp. 1295-1301.

75. Powell, R. L. and Stetson, K. A., "Interferometric Vibration Analysis by Wavefront Reconstruction," *Journal of Optical Society of America*, 1965, Vol. 55, pp. 1593-1608.

76. Gåsvik, K. J., 2002, *Optical Metrology*, John Wiley & Sons Ltd.

77. Kreis, T., *Holographic Interferometry: Principles and Methods*, 1996, Akademie Verlag GmbH, Berlin.

78. Hariharan, P., Oreb, B. F., and Brown, N., "A Digital Phase-Measurement System for Real-Time Holographic Interferometry," *Optics Communications*, 1982, Vol. 41, No. 6, pp. 393-396.

79. K. C. Harvey and C. J. Myatt, "External-Cavity Diode Laser Using a Grazing Incidence Diffraction Grating," *Optics Letters*, 1991, Vol. 16, pp. 910–912.

80. Maack, T., Notni, G., and Schreiber, W., "Three Coordinate Measurement of an Object Surface with a Combined Two-Wavelength and Two Source Phase Shifting Speckle Interferometer," *Optics Communications*, 1995, Vol. 115, No. 5-6, pp. 576–584.

81. Suematsu, M. and Takeda, M., "Wavelength-Shift Interferometry for Distance Measurements Using the Fourier Transform Technique for Fringe Analysis," *Applied Optics*, 1991, Vol. 30, No. 28, pp. 4046-4055.

82. Gonzalez, R. C. and Woods, R. E., *Digital Image Processing*, 2001, Prentice-Hall.

83. http://www.newfocus.com/datasheets/ds_TLB-6300.pdf

84. http://vfm.dalsa.com/docs/manuals/1m30p_user_manual_03-32-10001-03.pdf?refr=

85. Coherix, 2002, *User's Manual for Coherix Non-contact Precision Measurement Holomapper*

86. Coherix, 2004, *HoloMapper Calculations: A Description in Matlab*

87. Liggett, J. V., "*Dimensional Variation Management Handbook, A Guide for Quality, Design, and Manufacturing Engineers*," 1993, Prentice-Hall.

88. Automotive IndustryAction Group, "*Measurement Systems Analysis. Reference Manual*," 2002.

89. ANSI standard Y14.5, *Dimensioning and Tolerancing*, 1982, New York: The American Society of Mechanical Engineers.

90. ISO standard 1101, *Technical Drawings – Geometrical Tolerancing*, 1983-12-01.

91. Murthy, T. S. R. and Abdin, S. Z., "Minimum Zone Evaluation of Surfaces," *International Journal of Machine Tool Design and Research*, 1980, Vol. 20, pp. 123-136.

92. Samuel, G. L. and Shunmugam, M. S., "Evaluation of Straightness and Flatness Error Using Computational Geometric Techniques," *Computer-Aided Design*, 1999, Vol. 31, pp. 829-843.

93. Shunmugam, M. S., "New Approach for Evaluating Form Errors of Engineering Surfaces," *Computer-Aided Design*, 1987, Vol. 19, No. 7, pp. 368-374.

94. Narayanan Namboothiri, V. N. and Shunmugam, M. S., "Function-Oriented Form Evaluation of Engineering Surfaces," *Precision Engineering*, 1998, Vol. 22, pp. 98-109.